Thermal Stress Based Model Predictive Control of Power Electronic Converters in Electric Drives Applications

Dissertation

zur Erlangung des akademischen Grades
Doktor der Ingenieurwissenschaften
(Dr.-Ing.)

Technische Fakultät
der Christian-Albrechts-Universität zu Kiel
vorgelegt von

Johannes Falck, M. Sc.

Kiel
2021

Erklärung

Ich erkläre hiermit, dass ich die Dissertation zum Thema:

Thermal Stress Based Model Predictive Control of Power Electronic Converters in Electric Drives Applications

abgesehen von der Betreuung durch Herrn Prof. Marco Liserre selbstständig und ohne Hilfe angefertigt habe und bisher weder ganz noch zum Teil an einer anderen Stelle im Rahmen eines Prüfungsverfahrens vorgelegt, veröffentlicht oder zur Veröffentlichung eingereicht habe. Weiterhin versichere ich hiermit, dass ich die vorliegende Arbeit unter Einhaltung der Regeln guter wissenschaftlicher Praxis der Deutschen Forschungsgemeinschaft angefertigt habe und alle von anderen Autoren wörtlich übernommenen Stellen wie auch die sich an die Gedankengänge anderer Autoren eng anlehnenden Ausführungen meiner Arbeit besonders gekennzeichnet und die entsprechenden Quellen angegeben sind. Mir wurde kein akademischer Grad entzogen.

Kiel, 03. März 2020

Johannes Falck

1. Gutachter: Prof. Dr.-Ing. Marco Liserre
2. Gutachter: Prof. Dr.-Ing. Jörg Roth-Stielow
3. Gutachter: Prof. Dr.-Ing. Thomas Meurer

Datum der Disputation: 27. November 2020

Danksagung

Die vorliegende Arbeit entstand während meiner Tätigkeit als wissenschaftlicher Mitarbeiter am Lehrstuhl für Leistungselektronik an der Technischen Fakultät der Christian-Albrechts- Universität zu Kiel. Sie wurde von der Gesellschaft für Energie und Klimaschutz Schleswig-Holstein (EKSH) mit einem Stipendium gefördert. Für die Förderung und den regelmäßigen interdisziplinären Austausch bedanke ich mich herzlich.

Mein besonderer Dank gilt Prof. Marco Liserre, der mir den Weg zur Promotion eröffnet hat und mich umfassend betreut und unterstützt hat. Darüber hinaus möchte ich mich für die mir eröffneten Möglichkeiten und das mir geschenkte Vertrauen bedanken. Für die Übernahme der Koreferate bedanke ich mich herzlich bei Prof. Dr.-Ing. Jörg Roth-Stielow und Prof. Dr.-Ing. Thomas Meurer.

Meinen Kollegen, die mich in meiner Zeit am Lehrstuhl begleitet haben, möchte ich für die vielen fachlichen und nicht-fachlichen Gespräche sowie für die gute Zusammenarbeit danken. Ebenso möchte ich mich bei den Studierenden bedanken, die mit mir zusammengearbeitet haben. Für die labortechnische Unterstützung bedanke ich mich bei Bernd Doneit.

Besonders bedanken möchte ich mich zudem bei meiner Frau Stefanie, meinen Eltern und meinen Freunden, die mich während meines Studiums und während meiner Promotion stets unterstützt haben.

15. April 2021
Johannes Falck

Table of Contents

German Summary

Leistungselektronik wird vor allem in Frequenzumrichtern, Elektrofahrzeugen und erneuerbaren Energiesystemen verwendet und zunehmend in neuen Anwendungsbereichen wie Beleuchtung, elektrischen Komponenten in Luftfahrzeugen und medizinischen Systemen eingesetzt. Der zuverlässige Betrieb über die gesamte Lebensdauer ist für jedes leistungselektronische System von entscheidender Bedeutung, insbesondere weil die Zuverlässigkeit der Leistungselektronik in Bereichen wie Energieversorgung, Medizin und Logistik zu einer Voraussetzung für die Systemsicherheit wird. Die thermische Belastung leistungselektronischer Komponenten ist eine der wichtigsten Ursachen für deren Ermüdung. Der richtige Umgang mit den Wärmeverlusten spielt eine entscheidende Rolle für einen zuverlässigen und ökonomischen Betrieb der Leistungselektronik. Als eine der anfälligsten und teuersten Komponenten stehen Leistungshalbleiter im Mittelpunkt dieser Arbeit.

Die Aktive Thermische Regelung ermöglicht es, die Temperaturen von Leistungshalbleitern zu regeln, um die thermische Belastung zu verringern. Hierfür wird die modelprädiktive Regelung mit endlicher Anzahl von Schaltzuständen (FCS-MPC) gewählt. In der FCS-MPC werden die Raumzeiger unter Berücksichtigung von mehreren Eingangsparametern ausgewählt. Für die Auswahl des optimalen Raumzeigers können auch nichtlineare elektrische und thermische Modelle verwendet werden. Dieser Raumzeiger wird ohne zusätzliche Modulation auf das physikalische System angewendet. Dies ermöglicht die direkte Regelung des Schaltzustands und des Stroms durch jeden Halbleiter zu jedem Zeitpunkt.

Zur effektiven Regelung der thermischen Belastung ist ein Maß für den Verschleiß des Halbleiters erforderlich. Modelle hierzu aus der Literatur basieren auf den Verläufen von thermischen Zyklen und den Halbleitertemperaturen. Zur Abschätzung der Ermüdung während des Betriebs wird zunächst ein Verfahren zum Erfassen der Halbleitertemperaturen entworfen und validiert. Anschließend wird ein bewährtes Modell für die Ermittlung der thermischen Belastung angepasst, sodass es während des Betriebs funktioniert.

Dieses Modell wird in den Algorithmus der FCS-MPC integriert, um die thermische Belastung des Umrichters zu reduzieren und die Abnutzung der Halbleiter innerhalb eines Moduls anzugleichen. Die Wirksamkeit des Algorithmus wird mittels Simulationen demonstriert und mit Experimenten validiert. Es werden Methoden vorgestellt, die helfen, die optimale Balance zwischen Reduzierung der thermischen Belastung und Auftreten von zusätzlichen Verlusten im System einstellen zu können.

Zudem wird der Einfluss der Änderung des Rotorflusses der Maschine auf die Halbleitertemperaturen des Umrichters untersucht. Der Rotorfluss kann im Ergebnis als weiterer Parameter zur Steuerung der Halbleitertemperaturen verwendet werden. Dies ermöglicht es, größere Amplituden in thermischen Zyklen mit der Aktiven Thermischen

Regelung zu kompensieren. Dafür wird eine geeignete Regelung entworfen und experimentell validiert. Zuletzt wird die Kombination dieser Technik mit der FCS-MPC vorgestellt.

English Summary

Power electronics is used increasingly in a wide range of application fields such as variable speed drives, electric vehicles and renewable energy systems. It has become a crucial component for the further development of emerging application fields such as lighting, more-electric aircrafts and medical systems. The reliable operation over the designed lifetime is essential for any power electronic system, particularly because the reliability of power electronics is becoming a prerequisite for the system safety in several key areas like energy, medicine and transportation. The thermal stress of power electronic components is one of the most important causes of their failure. Proper thermal management plays an important role for more reliable and cost effective energy conversion. As one of the most vulnerable and expensive components, power semiconductors, are the focus of this thesis.

Active thermal control is a possibility to control the junction temperatures of power semiconductors in order to reduce the thermal stress. For this purpose the finite control-set model predictive control (FCS-MPC) is chosen. In FCS-MPC the switching vector is selected using a multi-parameter optimization that can include non-linear electric and thermal stress related models. This switching vector is directly applied to the physical system. This allows the direct control of the switching-state and the current through each semiconductor at each time instant.

For cost-effective control of the thermal stress a measure for the degradation of the semiconductor's lifetime is necessary. Existing lifetime models in literature are based on the thermal cycling amplitudes and maximum values of recorded junction temperature profiles. For online estimation of the degradation, a method to detect the junction temperatures of the semiconductors during operation is designed and validated. An existing and proven lifetime model is adapted for online estimation of the thermal stress.

An algorithm for the FCS-MPC is written that utilizes this model to drive the inverter with reduced stress and equalize the degradation of the semiconductors in a power module. The algorithm is demonstrated in simulation and validated in experiment. A technique to find the optimal trade-off between reduction of the thermal stress and allowing additional losses in the system is given.

The effect of rotor flux variation of the machine on the junction temperatures of the driving inverter is investigated. It can be used as another parameter to control the junction temperature. This allows increasing the maximal thermal cycling amplitude that can be compensated by an active thermal controller. A suitable controller is proposed and validated in experiment. The integration of this technique into the FCS-MPC is presented.

Nomenclature

General notations

$\hat{x}$	peak value of a parameter x
$\bar{x}$	mean value of a parameter x
$x(t)$, x	time depended parameter
X	constant
$x*$	reference value
x_a, x_b, x_c	referred to natural three phase system
x_α, x_β	referred to two-axis stationary coordinate system
x_d, x_q	referred to two-axis rotating coordinate system
$x_{IGBT,i}$	referred to IGBT i
$x_{diode,i}$	referred to power diode i
$f(x)$	f is a function of x

Semiconductor notations

i_C	collector current
i_f	diode forward current
v_{CE}	collector emitter voltage
v_{GE}	gate emitter voltage
v_f	diode forward voltage
E_{on}	switching on energy loss
E_{off}	switching off energy loss
E_{rr}	switching on energy loss

Inverter notations

i_{load}, i	current from inverter output to load
v_{dc}	dc link voltage
P_{in}	input power of the inverter
P_{cond}	conduction losses power
P_{sw}	switching losses power
P_{loss}	total losses power
f_{sw}	switching frequency
S_a, S_b, S_c	switching signals of phases a, b, c

Machine notations

R_s	stator resistance
R_r	rotor resistance
L_m	magnetizing reactance
L_s	stator leakage reactance
L_r	rotor leakage reactance
p	number of pole pairs
i_s	stator current
i_r	rotor current
ω_s	synchronous speed
ω_m	mechanic rotor speed
M_{el}	electric torque
M_m	mechanic torque
Ψ_s	magnetizing flux of the stator
Ψ_r	magnetizing flux of the rotor
θ_r	angle of the rotor
$\theta_{\Psi r}$	angle of the rotor flux

Thermal notations

T_j	junction temperature
T_c	module's case temperature
T_h	heatsink temperature
T_a	ambient temperature
ΔT	thermal cycle amplitude
R_{th}	thermal resistance
C_{th}	thermal capacity
Z_{th}	thermal impedance
τ_{th}	thermal time constant

Model predictive control notations

n	sampling instant
k	space vector
l	semiconductor in the module
g	cost function
λ	weighting coefficient of cost function

$x_i(n,k)$	referred to error from current reference
$x_c(n,k,l)$	referred to additional device damage
$x_{sp}(n,k)$	referred to device junction temperature spread
$x_{loss}(n,k)$	referred to power losses (switching & conduction)
$x_{imax}(n,k)$	referred to maximum device current constraint
$x_{Tmax}(n,k)$	referred to maximum device temperature constraint
annotation:	x is a space holder for g or λ

State space model notations

$x(n)$	state vector
$y(n)$	output vector
$u(n)$	input vector
A	state matrix
B	input matrix
C	output matrix
D	feedthrough matrix

Specific notations

N_f	number of cycles to failure
η	efficiency
f	fundamental frequency
T_s	sampling time of the control system
a	duty cycle
n	discrete time step
t	time

1. Introduction

This section is to motivate the reduction of the thermal stress in power electronics converters and formulates the research proposal of the thesis. Afterwards, the structure of the thesis is explained and the publications related to the different chapters are assigned.

1.1 Motivation

Power semiconductors are increasingly used not only in traditional fields like variable speed drives, consumable electronics and in new but consolidated ones like renewable energies but also in emerging fields like more-electric aircrafts and medical systems. Presently, the control system technology finds itself in a paradigm-changing tipping point, in which more demanding control goals, system flexibility, and functionalities required by emerging applications are driving the control system technology development, in addition to stabilization and robustness, which was the main focus in the past. The reliable operation is becoming crucial for the safety of several key areas like energy, health and transportation [1]. To reduce the required system size, material consumption and working time, power semiconductors in the lower and medium power range are often assembled into modules. An important cause of aging and failures of these modules is the cyclic heating and cooling processes, so called thermal cycles. Manufacturers face this problem by improving the assembly and materials which suffer from mechanical fatigue. These solutions attempt at reducing the effects of thermal cycling without curing the cause of the problem.

Only limited research has been carried out to reduce the thermal cycling with active thermal control, which aims at smoothing the fluctuation of the junction temperature of the semiconductors during operation [2]. Chosen control variables are the switching frequency, the modulation method, the dc link voltage, active and reactive circulating current, the turn on rise times and balancing of the thermal stress in a modular structure [3]. However, the main disadvantage of active thermal control is the decrease of the overall system efficiency or system performance. In addition to the performance deterioration, additional thermal control loops increase the complexity and the actual accumulated damage of the semiconductor is not taken into account.

To overcome these limitations the finite control-set model predictive control (FCS-MPC) seems the optimal approach because it allows an optimal control of every switching event and including of non-linear thermal and lifetime related models into the control law [4]. A precise control of the thermal stress in the semiconductors can be achieved as the optimal switching vector is directly applied to the physical system. A model for online junction temperature estimation that is suited for the use of FSC-MPC is designed. The proposed algorithm is a software solution for increasing the reliability and does not utilize special hardware like extra temperature probes nor active gate drivers.

1.2 Research goals

The general goal is to reduce the thermal stress in order to increase reliability and lifetime of power electronics modules in motor drives by using active thermal control. This can save both costs and resources, making it attractive for commercial use, especially for electric drives applications.

Target 1: Develop and test accumulated damage estimation
Thermal stress leads to fatigue of the power electronics modules. For most effective active thermal control knowledge of this accumulating damage is necessary during operation. Thus, the first target is to design algorithms that allow junction temperature detection and build a model that gives out the remaining lifetime of each semiconductor of the module online. A minimal invasive solution without additional sensors or hardware is aimed. The algorithms and models are tested for their effectiveness.

Target 2: Active thermal control for electric drives applications
First an analysis of the thermal stress in power converters for electric drive applications is done. An active thermal control procedure is developed to reduce thermal stress and reduce unsymmetrical fatigue of the module chips while avoiding unnecessary losses. This multi-parameter optimization is done using model predictive control. The aim is achieving the minimum thermal stress for the best possible overall performance.

Target 3: Provide design guidelines for active thermal control
Since active thermal control with the MPC approach has not been done before, design guidelines have to be established. Design guidelines allow not only to apply the control to a specific laboratory system, but also to adapt the control to real systems. The ratio of thermal stress reduction on the one side and negative side-effects like additional losses or current ripple on the other side is key of this trade-off.

1.3 Structure of this thesis

This thesis is structured in seven chapters. In Figure 1.1, the topics are assigned to two main categories and the publications are associated to the respective sections.

Chapter 1 is this introduction.

Chapter 2 introduces the model predictive control. State of the art and theoretical background of the control structure are given.

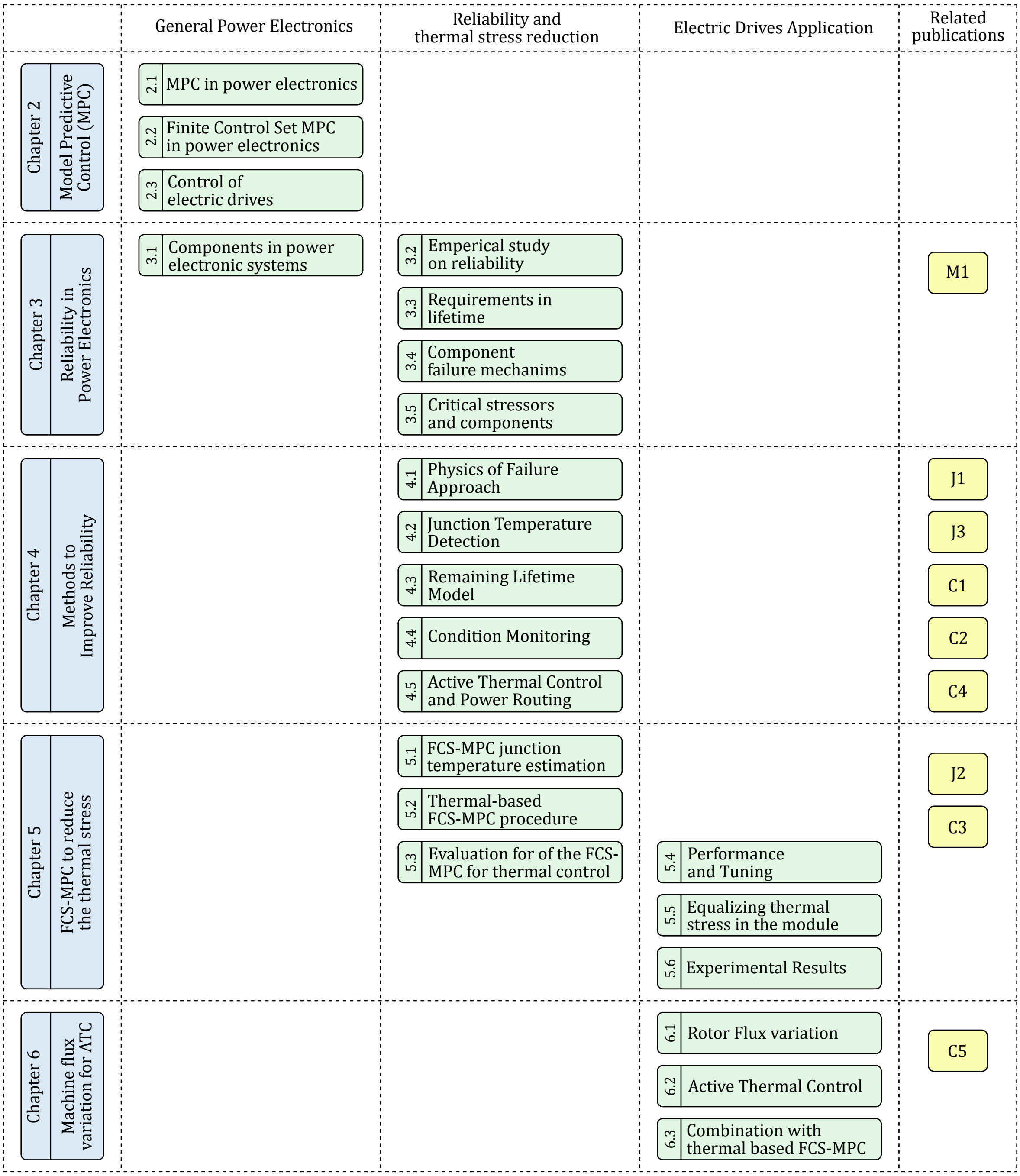

	General Power Electronics	Reliability and thermal stress reduction	Electric Drives Application	Related publications
Chapter 2 Model Predictive Control (MPC)	2.1 MPC in power electronics 2.2 Finite Control Set MPC in power electronics 2.3 Control of electric drives			
Chapter 3 Reliability in Power Electronics	3.1 Components in power electronic systems	3.2 Emperical study on reliability 3.3 Requirements in lifetime 3.4 Component failure mechanims 3.5 Critical stressors and components		M1
Chapter 4 Methods to Improve Reliability		4.1 Physics of Failure Approach 4.2 Junction Temperature Detection 4.3 Remaining Lifetime Model 4.4 Condition Monitoring 4.5 Active Thermal Control and Power Routing		J1 J3 C1 C2 C4
Chapter 5 FCS-MPC to reduce the thermal stress		5.1 FCS-MPC junction temperature estimation 5.2 Thermal-based FCS-MPC procedure 5.3 Evaluation for of the FCS-MPC for thermal control	5.4 Performance and Tuning 5.5 Equalizing thermal stress in the module 5.6 Experimental Results	J2 C3
Chapter 6 Machine flux variation for ATC			6.1 Rotor Flux variation 6.2 Active Thermal Control 6.3 Combination with thermal based FCS-MPC	C5

Figure 1.1: Structure of the thesis with the related publications.

Chapter 3 gives an overview on the reliability in power electronics. Relevant components of power electronic systems are identified first. For these components critical stressors and failure mechanisms are investigated for a broad range of power electronics applications. Reliability measures are reviewed and their utilization in industry is questioned. Finally, based on the findings, it is concluded: (1) on what the future reliability R&D should be focused and (2) how this R&D should be conducted in order to maximize the gain for industrial power electronic systems.

Chapter 4 describes active methods to improve the reliability. These are are software-based control structures that are applied during operation in order to release stress from its components. It starts with introducing the necessary auxiliaries as the junction temperature estimation.

Chapter 5 thoroughly develops the components of an algorithm to reduce the thermal stress of power electronic modules that utilizes the model predictive control. The algorithm is analytically developed and the performance is demonstrated in simulation and experiment in an electric drives application.

Chapter 6 discusses the possibility to use the machine flux of an induction machine as an additional control parameter for active thermal control. This degree of freedom is used to control the losses occurring in the semiconductor devices with the target to reduce the thermal cycles.

Chapter 7 concludes the thesis.

1.4 Publications related to this thesis

A complete list of the publications related to this thesis is given here.

[M1] J. Falck, C. Felgemacher, A. Rojko, M. Liserre, P. Zacharias: "Improving reliability in power electronics: An industry perspective", IEEE Industrial Electronics Magazine, vol. 12, no. 2, pp. 24-35, June 2018.

[J1] M. Andresen, K. Ma, G. Buticchi, J. Falck, F. Blaabjerg, M. Liserre: "Junction Temperature Control for More Reliable Power Electronics", IEEE Transactions on Power Electronics, 2018, 33, pp. 765-776

[J2] J. Falck, G. Buticchi, M. Liserre: "Thermal-based Model Predictive Control of Electric Drives", IEEE Transactions on Industry Applications, 2017, 54.2, pp. 1513-1522

[J3] M. Andresen, J. Kuprat, V. Raveendran, J. Falck, M. Liserre: "Active Thermal Control for Delaying Maintenance of Power Electronics Converters", Chinese Journal of Electrical Engineering, vol. 4, no. 3, pp. 13-20, September 2018

[C1] M. Andresen, G. Buticchi, J. Falck, M. Liserre, O. Muehlfeld: "Active thermal management for a single-phase H-Bridge inverter employing switching frequency control", Proc. of PCIM Europe 2015; International Exhibition and Conference for Power Electronics, Intelligent Motion, Renewable Energy and Energy Management, 2015, pp. 1-8

[C2] J. Falck, M. Andresen, M. Liserre: "Active thermal control of IGBT power electronic converters", Proc. of 2015 41st Annual Conference of the IEEE Industrial Electronics Society (IECON), 2015, pp. 1-6

[C3] J. Falck, M. Andresen, M. Liserre: “Thermal-based finite control set model predictive control for IGBT power electronic converters”, Proc. of 2016 IEEE Energy Conversion Congress and Exposition (ECCE), 2016, 1-7

[C4] J. Falck, M. Andresen, M. Liserre: “Active methods to Improve Reliability in Power Electronics”, Proc. of 2017 43st Annual Conference of the IEEE Industrial Electronics Society (IECON), 2017, pp. 1-6

[C5] J. Falck, M. Liserre: “Induction machine flux variation for active thermal control”, Proc. of 2017 20th European Conference on Power Electronics and Applications (EPE’18 ECCE Europe), 2018, pp. 1-10

1.5 Assignment of publications to the sections of this thesis

The publications related to this thesis are assigned to the different sections in the following.

- Chapter 3 is based on magazine article [M1].
- Chapter 4 is based on journal articles [J1], [J3] and conference articles [C1], [C2], [C4].
- Chapter 5 is based on journal article [J2] and conference article [C3]
- Chapter 6 is based on conference article [C5].

2. Model Predictive Control

The concept of predictive control is known since the end of the 1970s and has been initially used in process control engineering [5]. Since then, the predictive control procedures have been constantly improved and have penetrated more application areas.

Predictive control structures can be divided into two main categories according to their functional principles: Predictive control with use of a controlled system model and predictive control without use of a controlled system model [6]. Hence the integration of an electro-thermal model is a key feature in this thesis, predictive control without use of a controlled system model will not be considered here.

A further classification can be done for predictive control with use of a system model as shown in Figure 2.1. Model predictive control (MPC) is delimited from deadbeat control, hysteresis based control and trajectory based control hence the prediction of the controlled system behaviour is done for a larger control horizon in MPC. Therefore, it is also known as long-range predictive control [7]. The control horizon is the amount of predicted future samples in which control parameters are changed. In this context the prediction horizon is the amount of predicted future samples. To compute the system state also previous system states are taken into account in MPC, which is another essential distinction. In the bottom layer in Figure 2.1, a classification of MPC is done by the kind of output the control system is creating. For an output of switching states that are directly applied to the power electronic system the notation finite control set (FCS) is used. If the control computes a continuous control action, which needs a modulation technique to be applied to the power electronic system, the notation continuous control set is used [8].

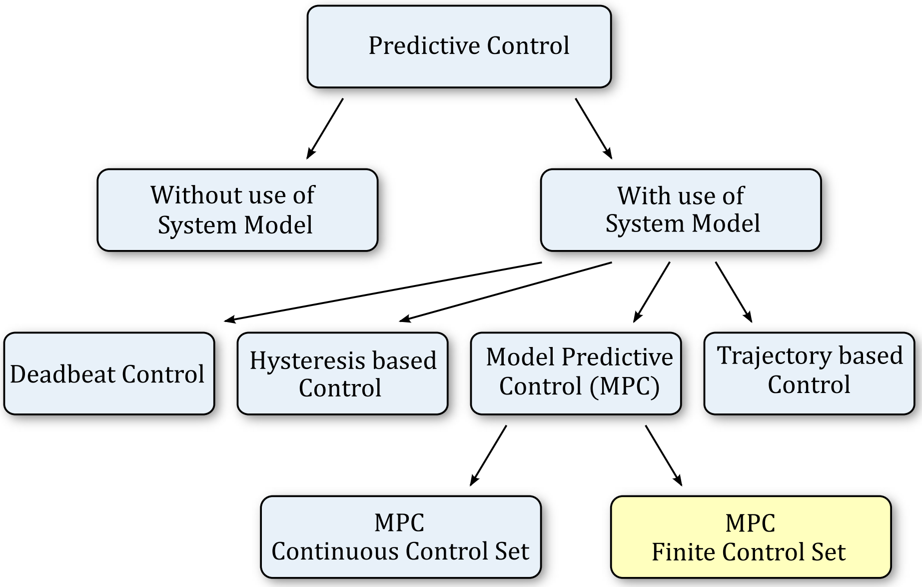

Figure 2.1: Classification of predictive control in power electronics.

2.1 MPC in power electronics

First employments of predictive control in power electronics and electric drives have been reported in the 1980s for high-power systems with low switching frequency [9, 10]. The use of high switching frequencies was not possible at that time due to the large calculation time required for the control algorithm [11]. With the development of faster and more powerful control systems, deployment in more power electronics applications became possible. So far, MPC has been proposed in several fields in power electronics, e.g. distributed generation systems, active filters and power conditioning, drives, non-conventional renewable energy and uninterruptible power supplies [12]. However, it is less commonly used in these applications, since the computational effort of predictive control is higher than in classic linear control while clear advantages are limited to niche applications [13].

The main principle of MPC is to use a model of the system to predict its dynamic behavior during operation. The system outputs are computed by evaluation of a cost function on the basis of this prediction. Figure 2.2 shows the general structure of MPC. The main parts are the system model, the cost function and the control law which is derived from the optimizer [14]. The calculation of the system outputs is done using the receding horizon principle [15]. To this, the optimal future output is evaluated each sample and subsequent it is applied to the system. In the next sample this calculation is repeated using updated measurement inputs. This ensures a feedback, making MPC a type of closed-loop control [15].

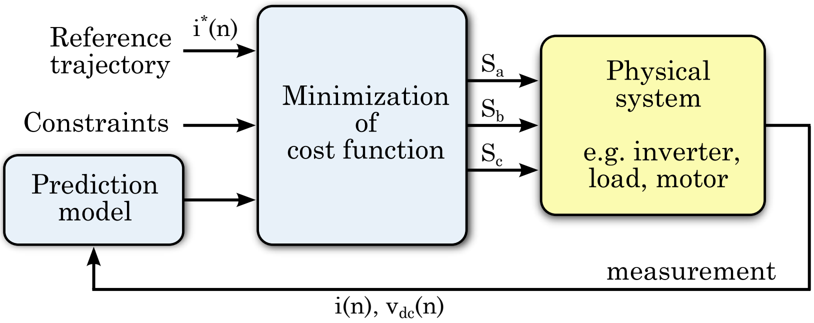

Figure 2.2: Control Structure of FCS-MPC using the receding horizon principle.

The prediction model is discrete-time with sampling instants n, therefore it can be expressed as a state space model with state vector $\mathbf{x}(n)$, output vector $\mathbf{y}(n)$ and input vector $\mathbf{u}(n)$ that holds the measurement data. The prediction model is defined by the state matrix A, the input matrix B, the output matrix C and the feed-through matrix D. The state space model is written as:

$$\mathbf{x}\,(n+1) = A \cdot \mathbf{x}\,(n) + B \cdot \mathbf{u}\,(n) \tag{2.1}$$

$$\mathbf{y}(n) = C \cdot \mathbf{x}(n) + D \cdot \mathbf{u}(n) \tag{2.2}$$

The cost function is used to evaluate the predictions of the prediction model. This function considers the references, the future states and the future outputs:

$$g = f(\mathbf{x}(n), \mathbf{u}(n), ..., \mathbf{u}(n+N)) \tag{2.3}$$

Finding the cost function g with the lowest cost is an optimization problem. It consists of minimizing the cost function within the prediction horizon while regarding the restrictions of the system. The result is a sequence of N optimal actuations [11].

2.2 Finite control set MPC in power electronics

Switching elements in power electronic systems can be driven either by using a modulator or the switching signals are generated directly by the controller. As only a finite amount of switching states is possible in power electronic inverters, the latter can be realized using FCS-MPC. This is advantageous as no modulator is needed and every switching operation can be determined by the cost function of the control algorithm. Therefore, the switching frequency is variable. The cost function in MPC for converter systems includes at least a term regarding the current or voltage error to ensure that it is following the reference values [16]. Other terms can be added to ensure e.g. the ideal minimal switching frequency is used [13]. Capacitor voltage balancing is added in [17]. On the contrary, in a modulator based structure the switching behavior is set with the choice of the modulator.

A three-phase two-level voltage source inverter (VSI) topology is used in a variety of applications in electric drives or grid injection. It has a total amount of $2^3 = 8$ possible switching states. From these valid switching states, six are active and two are zero vectors. These switching states can be illustrated in space vector representation. In FCS-MPC, the model is used to predict the consequences of each possible switching operation and subsequently possible switching operation according to the depth of the prediction horizon. The cost function is used to evaluate each switching operation. Afterward, the space vector with the lowest costs is searched and is then applied to the physical system. The computational effort rises rapidly for increasing prediction horizon. Therefore, it is possible to filter unfit switching operations first. A vast reduction is possible, if only switching at maximum one leg per control cycle is allowed, which can also be obtained as allowing only the two neighbor vectors and a zero vector or three 120° displaced vectors if a zero vector is active or in both cases no switching operation [13].

The defined cost function represents the desired behavior of the system. In power electronics a common task of the controller is to let the inverter output current follow a given reference. This means the error between current measurement and current reference has to be minimized for all its elements. A possible cost function for this aim is:

$$g_i = |i_\alpha^* - i_{\alpha,n,k}| + |i_\beta^* - i_{\beta,n,k}| \tag{2.4}$$

In this equation n is the sampling instant for which the prediction is done and k is the space vector. This equation is transferable for other parameters and components in the index. This cost function has a linear behavior regarding the size of the error. The quadratic or cubic absolute value can be chosen to cause more penalty for greater errors according to the chosen cost function.

This cost function is evaluated discrete sampling instant n and for space vectors k. The switching state that minimizes the cost function is selected:

$$g_{min} = \min g \tag{2.5}$$

With an increasing control horizon, the amount of required calculations rises exponentially. For the given three-phase two-level inverter with 8 possible switching states the number of calculations is 8^N, where N is the control horizon. At the same time the periods for computation in power electronics are smaller compared to classical applications of MPC like process control engineering. This is introducing a considerable time delay between computation start and actuation. Consequently, the computed space vector may not be optimal any more when it is applied to the system. This delay can impact the performance of the system if not considered in the controller design. To compensate this delay, the computation of the space vector in the subsequent sampling instant $n+1$ is already performed during sampling instant n. The space vector that is applied to the system in sampling instant n is known from the previous optimization. It is used to predict the parameters (e.g. the load currents) of sampling instant $n+1$. On this basis all space vectors until reaching the control horizon are predicted and evaluated with the cost function to find the optimal space vector for sampling instant $n+1$. This is shown in Figure 2.3. This compensation method is described particularly in [11]. Similar compensation methods have also been proposed for other predictive control schemes such as deadbeat control [18].

To find the optimal space vector the necessary parameters of all possible space vectors have to be predicted and the cost function has to be evaluated. For increasing control horizons, the used data structure becomes a relevant parameter for optimal utilization of the processing power of the used control system. There are two main procedures for reaching all space vectors known from the search tree data structure in computer science: The iterative deepening depth-first procedure and the breadth-first procedure [19]. In Figure 2.4 and Figure 2.5 the different sequences of predicting and evaluating

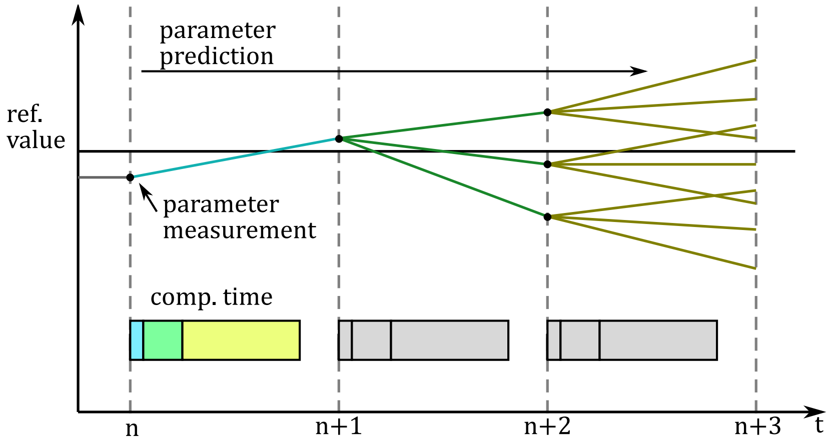

Figure 2.3: MPC prediction with time delay compensation. A system with three possible space vectors is assumed for simplicity.

the space vectors are illustrated for four sampling instants and eight possible switching operations at each instant for both procedures respectively.

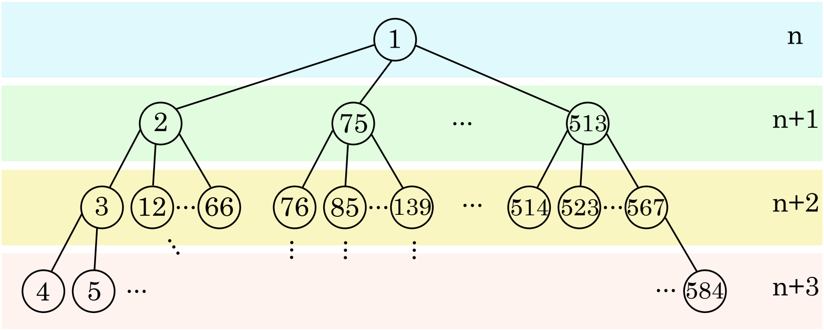

Figure 2.4: Iterative deepening depth-first structure.

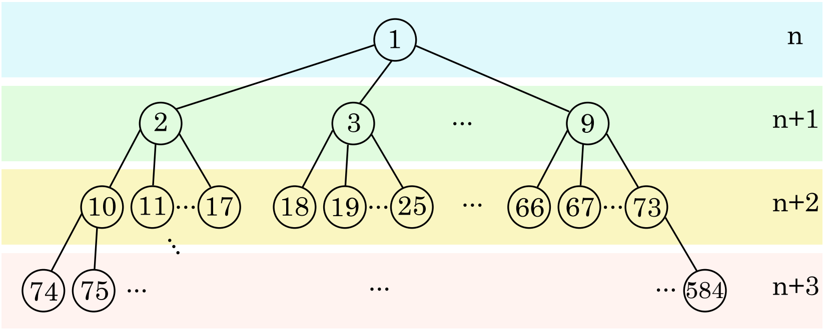

Figure 2.5: Breadth first structure.

The first procedure is the iterative deepening depth-first. After evaluating a specific space vector its successors in the time-line are evaluated until the control horizon is reached. The computed results are used for the directly following calculations of the next sampling instant. When all successors have been reached the data is not accessed again. This reduces the necessary amount of memory storage and also results in minimal saving and loading operations. Therefore, the depth-first strategy is efficient in computation. If the computational burden exceeds the algorithm may not finish all predictions within the given sampling instant. Due to the depth-first character even the eight predictions in the $n + 1$ layer may not have completed, which is a disadvantage of this procedure.

The second procedure is breadth-first. In Figure 2.5 the sequence of predicting and evaluating the space vectors is illustrated in the same framework as the depth-first procedure. Computation of the next sampling instant is started when all calculations of the previous sampling instant are completed. To proceed to the succeeding sampling instant all parameters of the previous sampling instant need to be accessible. This means additional memory requirements compared to the iterative deepening depth-first procedure. It has the advantage, that no fixed prediction horizon has to be selected for this procedure as computation can be continued until the end of the given sampling instant.

The complete iteration of the finite control set MPC in power electronics is given in a flowchart in Figure 2.6. First the optimal space vector is applied to the system. During this space vector takes effect on the system, the prediction of the parameters at the end of this iteration is done. As the applied space vector and the system parameters are known the prediction is very close to the reality which is only measurable at the end of the iteration. This prediction is used as a starting point to predict parameters and evaluate the cost function for the next iteration for all space vectors which is the most time consuming part. In the end the space vector with minimal costs is searched and stored to be applied in the next iteration. This flowchart demonstrates a single step control horizon. The procedure for multiple step control horizons depends on the chosen data structure.

2.2.1 Application of FCS-MPC in power electronics

Advantages of MPC are its usability in a variety of processes and being simple to apply in multi-variable systems. Beyond, it is straightforward to include nonlinearities and constraints into the control law [12]. The disadvantageous high amount of computational effort is diminishing as computational power of control platforms has increased distinctly in the last decades. Thus, MPC has been employed in a wide range of power electronic applications.

Usage of MPC has been reported for several topologies such as dc-dc converters, two-level VSI, neutral point clamped (NPC), cascaded H-bridges, flying capacitor inverters, rectifiers, multilevel converters and matrix converters [20], [12], [21]. The structure of MPC allows this control flexibility for these topologies by adjustment of the system model. Equally effective MPC can be adapted to control current, voltage, torque, flux and other variables by adjustment of the system model [22]. This enables it to be used for a wide range of power electronic applications, such as distributed generation

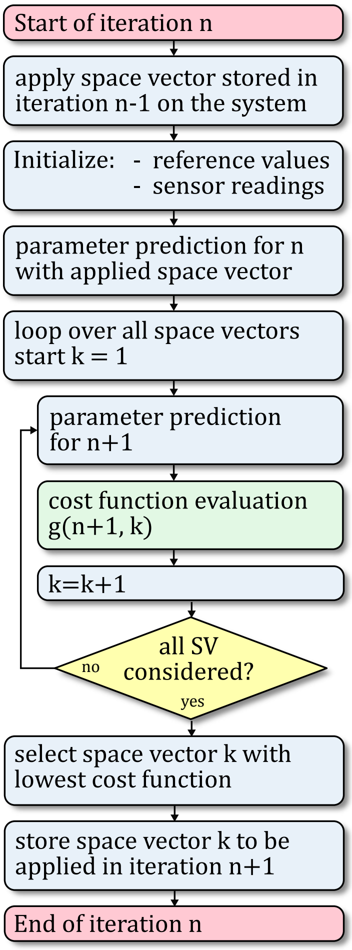

Figure 2.6: General flowchart of the finite control set MPC in power electronics for a single step control horizon.

systems, grid injection of renewable energy, active filters, drives and uninterruptible power supplies [23], [12].

In [24] discontinuous PWM by clamping one leg to either the positive or negative dc link voltage of a VSI is adapted for FCS-MPC. To determine phase and duration of the clamping both the future voltage and the load current are predicted in a system model. In contrast to conventional current based FCS-MPC that is only involving the load current, also a voltage based FCS-MPC scheme is proposed thereby.

In [21] a FCS-MPC for a two-cell cascaded H-Bridge multilevel rectifier is suggested, which is adaptable for other topologies like a three-phase rectifier due to the nature of MPC. A two-step prediction horizon is used for control dynamic and steady-state operation conditions. Stabilization of the system and favorable performance during transients are reported in experimental investigation.

2.3 Comparison of conventional control and FCS-MPC

Several comparisons of conventional control and FCS-MPC for power converters have been done in literature. As the FCS-MPC has been described in the previous section, in this section the conventional control of power converters is described first. Afterward, a literature review on comparisons is given.

2.3.1 Conventional control of power converters

For a consideration of the system behavior of power converters using conventional control strategies, it is distinguished between low and medium voltage applications. While in the low-voltage applications the maximum achievable control dynamics is desired, in medium-voltage applications the power losses or current distortions arising from the selected control concept are focused [25]. This is mainly due to the different power semiconductor components used and the resulting possible switching frequency ranges in which the various applications are operated. Typical switching frequency ranges of power pulse converters in low voltage applications are from 1 kHz to 20 kHz depending on the rated input power, whereas typical switching frequencies of power pulse converters in medium voltage applications range from 200 Hz to 1 kHz depending on the connected load and power semiconductor technology used. Different filter topologies are also used, depending on the application and the used voltage, which also influence the choice of suitable control strategies.

Converters connected to the grid in low-voltage applications are conventionally controlled in a rotating coordinate system based on the grid voltage, the voltage-oriented control. The advantage of this control structure is that, by transforming the measured current and voltage signals into a coordinate system rotating with the line frequency and oriented to a voltage phase, the transformed signals ideally occur as equal variables and form an orthogonal system. The orthogonal system consists of a d-component (real part) and a q-component (imaginary part). This allows to fed and consume active and reactive power by specification of the corresponding current components [26]. Common is a cascaded control structure with external dc link voltage control loop for controlling the active power flow (d-component) and inner current loop for the d and q component. In addition, a phase-locked loop (PLL) is used to detect the line voltage angle required for the transformation into the rotating coordinate system and thus to synchronize the feed-in power with the grid voltage.

In literature several methods are described for controlling power converters for low-voltage applications with small to medium power ranges that are based on voltage-oriented control [26]. The proportional-integral controller (PI controller) control structure is applied in the control of grid-connected converters with L-filters as well as systems with LCL filters [27]. The limitations of the applicability of PI-based current control for power converters with LCL filters are mainly dependent on the choice of filter parameters and the resulting filter resonance frequency as well as the available measurement signals [28].

For conventional control structures of power converters in medium-voltage applications with high powers, the loss or current harmonics minimization are key due to restrictions of the available switching frequency. The voltage-oriented control concept is also conventional for these converters, but the carrier-based modulation strategies of the low-voltage applications are replaced by optimized modulation strategies for pulse pattern generation [29]. These are pre-calculated (offline) pulse patterns which have been optimized with regard to the number of occurring switching operations in order to minimize the switching losses and with regard to the occurring current harmonics in order to minimize the current harmonics. Based on the beginnings of pulse pattern optimization [30], the relevance of the optimized pulse patterns is shown in the low voltage and medium voltage ranges [29].

Conventional closed-loop control structures of converter applications with slow-cycling converters also use the voltage-oriented control concept, but differ in the implementation of the current regulation. Due to the voltage orientation, the orthogonal components of the rotating coordinate system are coupled. Therefore, the components can not be controlled independently. The effects of the coupling become more important with decreasing switching frequency and lead to a significant reduction of the achievable control quality. In order to counteract this effect, decoupling networks are implemented in addition to current regulation. Due to the limited dynamics and parameter uncertainties of the decoupling network, the coupling in the controller design are taken into account in slow-cycling applications, which leads to complex-valued current control structures [25].

2.3.2 Comparison of conventional control and FCS-MPC

The aim of both types of controllers is to let the control variable follow the command variable. The tolerance of the control deviation and the need for dynamics are dependent on the application. When comparing the structure of the FCS-MPC and the conventional control, differences are in the selection of the way the controller sets the control variable value, in the control feedback and in the controller output. However, the other elements of the control loop as the controlling element, the controlled system and its disturbance variables stay unchanged.

In [5] the implementation of an FCS-MPC current controller for a two-level drive converter is presented and the achievable control dynamics are experimentally verified for a low-voltage application with an induction machine with squirrel cage rotor. The results are compared with a hysteresis-based current control, which has a similar average switching frequency compared to the FCS-MPC controller. However, the FCS-MPC achieved a significant reduction in the harmonics of the current compared to the hysteresis-based control.

The FCS-MPC presented in [13] aims to reduce the number of switching operations in stationary operation of a two-stage converter on a drive system. The control target is split into minimizing the current drift in the transient operation of the system in order to high achievable control dynamics, whereas the steady-state control objective minimizes the switching operations in order to minimize the power dissipation of the system. Therefore, the FCS-MPC selects one of two cost functions depending on the detected operating point. The control strategies are validated to a low-voltage converter system and compared to a PI controller-based current control with pulse width modulation. If equal current distortion of the injected current for all considered control strategies are allowed, the average switching frequency can be significantly reduced with the FCS-MPC current control compared to the PI-based control with pulse width modulation.

In [31] another comparison of conventional control strategies versus the FCS-MPC is presented. A medium-voltage drive with an induction machine using a three-level converter system. Carrier-based pulse width modulation and pulse pattern-optimized modulation methods are compared. A significant reduction of the switching losses at constant current distortion compared to carrier-based pulse width modulation as well as pulse pattern-optimized modulation method was achieved. The results depend on the control objective and choice of the control horizon in steady-state operation of the considered drive system of the FCS-MPC.

2.4 Control of electric drives

At the moment, the widespread topology to drive a speed controlled induction machine is represented by the two level 3-phase inverter. This topology has six switched semiconductors and additional six anti-parallel diodes. In the last decades, control of electric drives has been widely studied. Linear methods like the proportional-integral (PI) controllers using pulse width modulation (PWM) are well-documented in the literature and dominate industrial applications [32]. Commonly, a cascaded control structure that separates the current control and the overlying machine control is used as it is also a well-approved approach. The field oriented control of induction machines was pioneered in the early 1970s by K. Hasse and F. Blaschke. Today it is the most widely used linear strategy in high performance electrical drives [33]. However, model predictive control strategies allow an increase of control dynamics and the inclusion of constraints to the control system.

In the next subsections conventional field oriented control and various MPC strategies for electric drives control systems are described. In subsection 2.4.5 a comparison of the strategies is given.

2.4.1 Conventional field oriented control

The research of field oriented control (FOC) was motivated in the controllability of dc machines, which allows to control the machine flux and machine torque almost independently from each. However, machine flux and machine torque of induction machines are both dependent on the stator current. FOC is a possibility to achieve almost independent control of machine flux and machine torque for the induction machine. There are several modifications of FOC that differ mainly in the choice of the reference coordinate system and the used machine models. Common is the rotor flux orientation.

The FOC controls the stator currents of a three-phase electric machine using vectors in a time invariant coordinate system. Its components represent the torque and the flux of the machine. The direct control of the torque allows precise control of the machine rotational speed and load. The direct control of the magnetization flux can be seen as an additional degree of freedom for optimizing the machine performance. The procedure of the FOC is shown in Figure 2.7 and is described in the following:

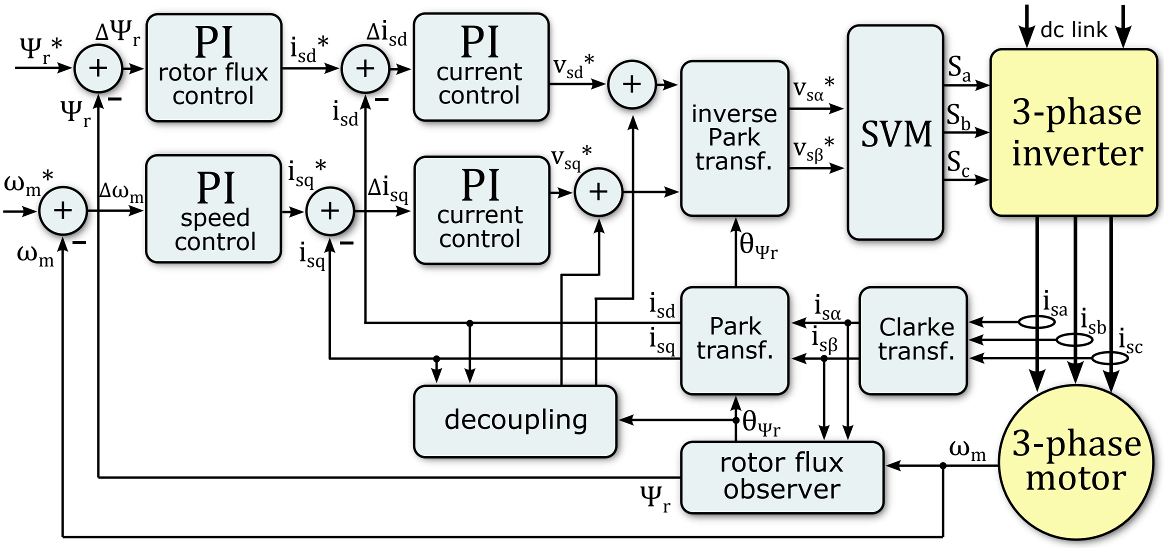

Figure 2.7: Field oriented control scheme of the induction machine using PI controllers.

The control of the three-phase induction motor is divided into an inner control loop to control the stator currents and an outer control loop to control the rotor flux and the machine rotational speed. Either all three stator phase currents are measured or two stator phase currents are measured and the third one is calculated according to Kirchhoff's laws:

$$i_{sa} + i_{sb} + i_{sc} = 0 \tag{2.6}$$

The three phase currents are converted from the stator's three-axis reference system into a two-axis coordinate system using the $\alpha\beta$-transformation, also called the Clarke-transformation:

$$\begin{bmatrix} i_{sd} \\ i_{sq} \end{bmatrix} = \begin{bmatrix} cos(\theta_r) & sin(\theta_r) \\ -sin(\theta_r) & cos(\theta_r) \end{bmatrix} \begin{bmatrix} i_{s\alpha} \\ i_{s\beta} \end{bmatrix} \tag{2.7}$$

The components in the biaxial $\alpha\beta$-coordinate system of the stator current are inherently time-variant. However, PI controllers are most suitable in compensating errors of stationary signals. Therefore, the stationary reference is rotated according to the rotor position determined by sensors or by back electromotive force (EMF). This is done by the dq transformation, also called the Park-transformation:

$$\begin{bmatrix} i_{s\alpha} \\ i_{s\beta} \end{bmatrix} = \frac{2}{3} \begin{bmatrix} 1 & -\frac{1}{2} & -\frac{1}{2} \\ 0 & \frac{\sqrt{3}}{2} & -\frac{\sqrt{3}}{2} \end{bmatrix} \begin{bmatrix} i_{sa} \\ i_{sb} \\ i_{sc} \end{bmatrix} \tag{2.8}$$

In this equation, i_{sd} and i_{sq} are the transformed stator currents relative to the rotor angle θ_r. The vectors of the Park-transformation are shown in Figure 2.8. The rotor flux Ψ_r rotates at synchronous speed ω_s. Therefore, the dq-frame rotates at the same speed. For measurement of the rotor angle, the rotor flux angle is detected. In order to determine the angle of the dq-frame, the angle of the rotor flux $\theta_{\Psi r}$ must be obtained at every sampling instant. It is defined as follows:

$$\theta_{\Psi r} = \int \omega_s dt \tag{2.9}$$

The input voltage of the induction machine is the stator voltage. The equation of the stator voltage in the stationary coordinate system is known as:

$$v_s = i_s \cdot R_s + \frac{d\Psi_s}{dt} \tag{2.10}$$

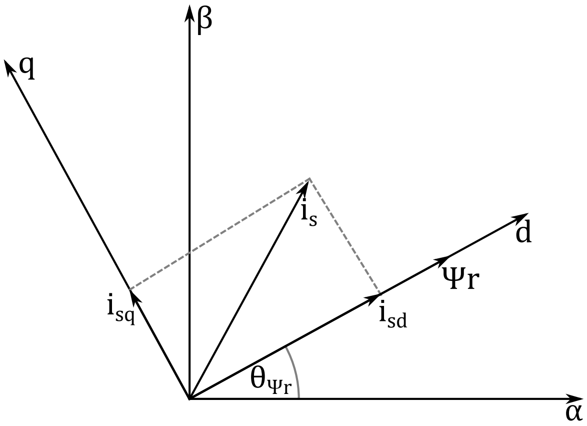

Figure 2.8: Rotor flux orientation.

It can be transformed in the dq-coordinate system:

$$v_{sd} = i_{sd} \cdot R_s + \frac{d\Psi_{sd}}{dt} - p \cdot \omega_m \cdot \psi_{sq} \tag{2.11}$$

$$v_{sq} = i_{sq} \cdot R_s + \frac{d\Psi_{sq}}{dt} + p \cdot \omega_m \cdot \psi_{sd} \tag{2.12}$$

The stator voltages evoke the corresponding stator currents. Their differential equations are:

$$\frac{di_{sd}}{dt} = -\frac{1}{\omega}\left(\frac{R_s}{L_s} + \frac{R_r}{L_r}(1-\sigma)\right) \cdot i_{sd} + \omega_s \cdot i_{sq} + \frac{1-\sigma}{\sigma L_m \frac{L_r}{R_r}} \cdot \Psi rd + \frac{1}{\sigma L_s} v_{sd} \tag{2.13}$$

$$\frac{di_{sq}}{dt} = -\frac{1}{\omega}\left(\frac{R_s}{L_s} + \frac{R_r}{L_r}(1-\sigma)\right) \cdot i_{sq} + \omega_s \cdot i_{sd} + \frac{1-\sigma}{\sigma L_m} \cdot p\omega_m \Psi rd + \frac{1}{\sigma L_s} v_{sq} \tag{2.14}$$

The d-component of the stator current is coupled with its q-component and vice versa. The coupling is not constant, it increases with increasing frequency of the feeding stator voltage. This coupling prevents the sheer separation of flux and torque control. However, a decoupling network is used to decouple the coupled components of the stator current. Input variables of the decoupling network are the reference value of the rotor flux, the measured and transformed stator current and the mechanical angular frequency multiplied by the number of pole pairs of the machine. From these quantities, the coupled d and q components of the stator current are calculated. For this step, the electrical characteristics of the induction machine and the mechanical angular frequency are mandatory.

Characteristic for the FOC is the cascaded control structure. The inner control loop controls the stator current. As the stator current was divided in dq components two PI controllers, one for each axis, are used to minimize the error between current measurement and reference. The current i_{sd} controls the magnetization flux of the rotor and the current i_{sq} controls the torque generated by the motor. For both currents, the references are the output of the outer control loop. This means the outer control loop is used to control the rotor flux and the machine speed. Both are controlled with additional PI controllers.

The rotor flux is calculated using a rotor flux observer as its direct measurement requires expensive hardware. The rotor flux reference value is set according to the induction machine parameters and system requirements. The usually chosen value of the flux reference depends on the desired operation. A high flux level increases the maximum torque of the machine. It is adequate for low-speed high-torque applications. To retain full torque capability over the entire speed range to compensate for load variations the nominal flux level of the machine is selected. For maximum efficient operation the flux reference is varied depending on the load torque. For field-weakening operation the flux reference is usually made proportional to the inverse of the rotor speed [34].

The speed reference for speed controller depends on the application. It may be controlled by a system controller at a higher level. In a real system which considers friction higher speeds lead to higher demand of torque. Accelerating an decelerating can also be expressed with the demand of torque. Therefore, instead of a speed controller a torque controller can also be used. The controller controls the demand of torque using i_{sq}.

A problem of cascaded controls like the FOC is the limitation of the dynamic behavior caused by the cascaded structure itself. The inner loop must be fast enough to reach an acceptable dynamic behavior of the whole system. This means the calculation times of the inner control loops limit the outer control loops and therefore the whole system. The non-linear characteristic of inverters, which is usually considered by linearization represents another problem. Linearization, however, leads to inaccuracies in the description of the inverter and drive characteristics [35].

2.4.2 Cascaded Control using MPC

Multiple variants of applying MPC for machine control are possible. The PI controllers of the conventional FOC can be fully or partial substituted with an MPC. This is possible, as the interface of both types of controllers, PI and MPC, can be designed identical. In this case the interface consists of an input for the reference value of the controlled parameter, the measured value of the controlled parameter and of the controller output. The controller within the interface can be substituted. However, most variants found in literature substitute both PI controllers of the conventional FOC inner loop with MPC, whereas PI controllers are chosen for both outer loop controllers [36], [13], [22], [37], [38].

The FCS-MPC can be used instead of PI controllers to control the stator currents. This allows to include e.g. more parameters, non-linearities and constraints into the control law. In Figure 2.9 a block scheme of a cascaded control of an induction machine is shown. A FCS-MPC is chosen for the current control. Rotor flux and machine speed are controlled in a field oriented control scheme using PI controllers.

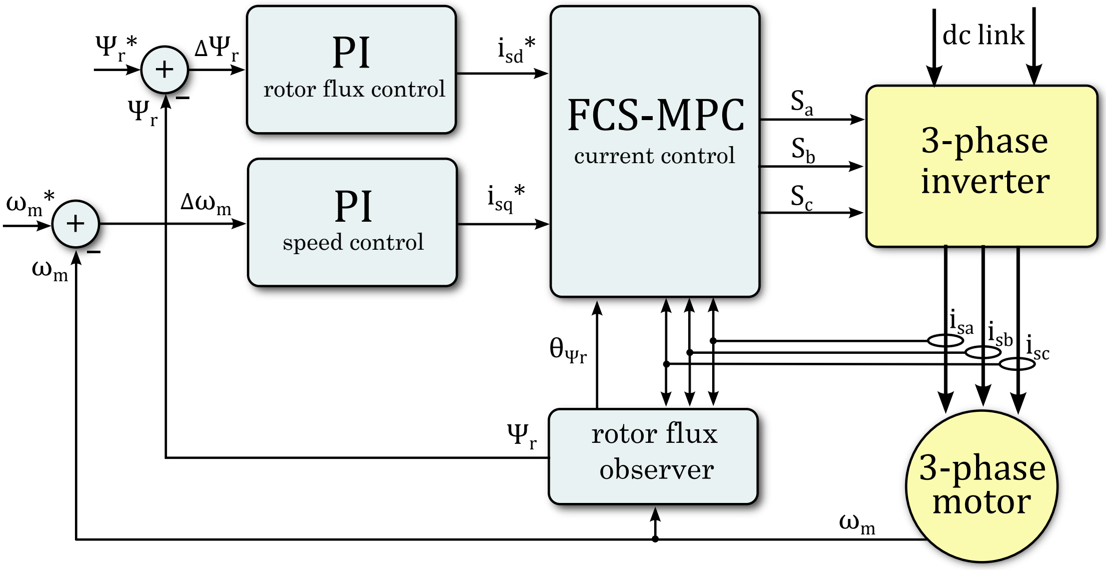

Figure 2.9: Cascaded motor control using FCS-MPC in the inner loop.

In [39] all four controllers of the FOC are designed as MPC. The cost functions of the outer loop MPC include the error of the observed flux and torque an constraints for its maximum values. For comparison the inner loop is designed with both, finite control set and continuous control set (CCS) with space vector modulation (SVM). The FCS-MPC is designed as described above. The CCS-MPC uses the system model to find two optimal stator voltage vectors that should be given on the system based on the cost function. in the SVM theses are selected from all the possible adjacent vector pairs using a cost function that considers the stator current prediction and duty cycles. These duty cycles determine the ratio for the active and zero voltage vectors within each sampling period [37]. The behavior of both control approaches is evaluated by applying reference and disturbance steps to the system. The ripple in current and torque are assessed. In the comparison of finite control set with the continuous control set, both approaches achieve similar performances and computational times [39].

2.4.3 Multiple input multiple output control using MPC

The induction machine can be considered as a multiple-input and multiple-output (MIMO) system. Inputs of the machine are at least the stator currents and the load torque or rotational speed at the machines shaft. Outputs are at least the measured or observed torque and machine flux. The behavior is not linear, as differential equations are used to describe its mathematical behavior. The electromechanical variables of the machine must be controlled to meet the application's demand. As the MPC is suited to act as a MIMO controller, the model of the induction machine can be directly integrated in the MPC [36]. The advantage is that this allows to include all nonlinear characteristics in the controller design [8] and the behavior of the system can be adapted to different demands by modifying the cost function accordingly [36]. Linearization of the machine equations is not necessary in contrast to conventional FOC.

The prediction model of a MIMO controller predicts the behavior of the induction machine's stator currents i_s, the machine's flux, in this case the stator flux Ψ_s, and the torque M_e according to the machine model. The cost function is evaluated for all space vectors and the space vector which minimizes the costs is applied on the system. Reference values for the machine flux and for the torque are necessary to compute the error that is evaluated in the cost function. In [8] the cost function for the induction machine g_{IM} is given as:

$$g_{IM} = \lambda_{\Psi} |\Psi_s^* - \Psi_{s,n,k}| + |M_e^* - M_{e,n,k}| + C_i \tag{2.15}$$

In this equation n is the sampling instant for which the prediction is done and k is the space vector. The tuning parameter λ_{Ψ} is used to define the importance of keeping the flux close to its reference value. This enables the controller to generate the flux at start up. The constraint C_i is defined as:

$$C_i = \begin{cases} 0 & i_{s,n,k} \leq i_{max} \\ \infty & \text{else} \end{cases} \tag{2.16}$$

2.4.4 Model Predictive Direct Torque Control

The Model Predictive Direct Torque Control is based on the Direct Torque Control and additionally predicts the flux and torque of the system using a prediction model [24]. This makes it a type of predictive controller and thus it is described here.

A non-linear hysteresis-based strategy is the direct torque control (DTC) [40]. It has found wide acceptance in academia and industry [41]. The principle of DTC is using the six active space vectors to guide the stator flux of the induction machine on a defined trajectory. The space vectors are changed continuously chronologically lead on a hexagonal trajectory. The corresponding voltage of the selected space vector is applied to the stator of the machine. Thus, the flux of the machine is set. The torque is determined by the speed at which the stator flux rotates on the trajectory, which in turn depends on the voltage of the space vector. The voltage of the resulting space vector is adjusted by periodically switching to one of the remaining two zero vectors.

When using conventional modulation, these space vectors are applied to the machine with a predetermined frequency. In DTC, the switching of the space vectors is determined by the stator flux, which can also be represented as a space vector. If the stator flux space vector exceeds a certain level, the next space vector depending on the current switch position is applied. Thus, the rotation of the flux triggers the switching to the next space vector.

A hysteresis flux controller compares the magnitude of the stator flux with the flux reference. At the same time, a hysteresis torque controller compares the current torque of the machine with its reference and switches one of the two zero vectors instead of the space vector selected by the flux controller. In common with FCS-MPC, the switching frequency can be significantly reduced, as the half-bridges must only be switched as soon as a deviation occurs. The switching frequency thus depends on the machine itself. In addition, another controller can be used, which changes the hysteresis of the torque controller as a function of the current switching frequency. Thus, for a given maximum switching frequency the optimal control of the torque is achieved. The control scheme of the DTC is given in Figure 2.10.

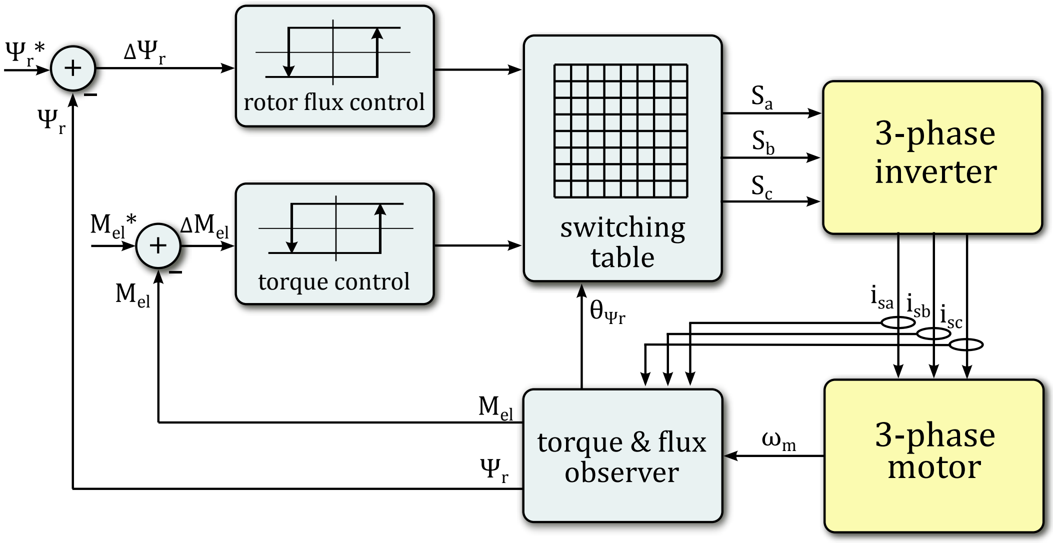

Figure 2.10: Direct Torque Control scheme.

The function of the DTC relies on the precise knowledge of the current machine stator flux and torque. To obtain these parameters, a mathematical model of the machine is required. This can be realized in the stationary $\alpha\beta$-coordinate system. A possibility to calculate the stator flux Ψ_s and electrical torque M_{el} is based on the stator currents i_s and stator voltages v_s. It is described in [42]. The main equations are given in the following:

$$v_{s\alpha} = R_s \cdot i_{s\alpha} + \frac{d\Psi_{s\alpha}}{dt} \tag{2.17}$$

$$v_{s\beta} = R_s \cdot i_{s\beta} + \frac{d\Psi_{s\beta}}{dt} \tag{2.18}$$

$$\Psi_{s\alpha} = \int (v_{s\alpha} - R_s \cdot i_{s\alpha})\, dt \tag{2.19}$$

$$\Psi_{s\beta} = \int (v_{s\beta} - R_s \cdot i_{s\beta})\, dt \tag{2.20}$$

$$M_{el} = p \cdot (\Psi_{s\alpha} \cdot i_{s\beta} - \Psi_{s\beta} \cdot i_{s\alpha}) \tag{2.21}$$

The controller calculates the desired quantities using measured parameters, such as stator currents and stator voltage. The DTC is applied in electric traction vehicles, as significant voltage fluctuations may occur due to short-term connection interruptions between pantograph and catenary. Since the DTC is robust against fluctuating dc link voltage, it is particularly suitable.

However, the main drawback of DTC are considerable torque ripples. For this reason finite control set model predictive direct torque control (FCS-MPDTC) was developed. FCS-MPDTC is a direct control method that predicts the flux and torque of the system using a prediction model [24]. It is build similar to the FCS-MPC as no modulator is used. The concept is to select in each control period one active and one zero vector to generate the desired output voltage. Therefore, a model of the machine is used to predict torque and flux for each possible active space vector and the one minimizing the costs is selected. In prior MPC approaches a zero vector is subsequently added to match the duty cycle. Several methods have been investigated to do this duty cycle optimization [43]. However, the separate selection of active and zero space vectors cannot ensure the minimization of torque error. This is hence the chosen space vector may no longer remain optimal if it is not applied for the whole control period. Also, the optimal solution may not have the lasting alternation between active vector and zero vector. A recent approach facing this problem is given in [44]. It is proposed to use a control horizon of two samples, predicting the impact of all possible two-vector switching operations and using a cost function to determine the most fitting one. In comparison with prior one-step prediction horizon MPC, torque and flux ripples as well as current harmonics could be reduced in steady-state using almost constant and even lower average switching frequency as validated in simulation and experiment. Like the DTC and FCS-MPC, the advantages of the FCS-MPDTC are its intuitive concept and straightforward implementation [45].

2.4.5 Comparison of the methods

A direct comparison in performance between FCS-MPC and a cascaded PI control with modulator for a two-level inverter connected to a permanent magnet synchronous machine is done in [13]. The proposed MPC has two different minimization goals, depending on whether the converter is in transient or steady-state operation. In transient mode, the goal is to minimize the current error as fast as possible, which features high control dynamics. However, in steady-state, the objective is to conduct a minimum amount of switching operations in order to reduce the losses. Therefore, two cost functions have been designed and one of them is selected for optimization by the controller depending on the detected operation point. In comparison with the PI control and modulator, a reduction of the average switching frequency is achieved using FCS-MPC. In Figure 2.11 the results of a Fourier analysis of PI controlled PWM currents and a Fourier analysis of MPC currents are given. The spectrum of the PI controlled currents is typical for currents created with a PWM modulator. Harmonics are found around the switching frequency and its integer multiples. The total harmonic distortion (THD) is 8.0 %. The noise of the MPC currents is spread over the full bandwidth. The THD is 9.8 %. Therefore, the MPC has a reduced THD compared to cascaded PI control with modulator. The different distributions of noise must be considered in the current filter design for the converter.

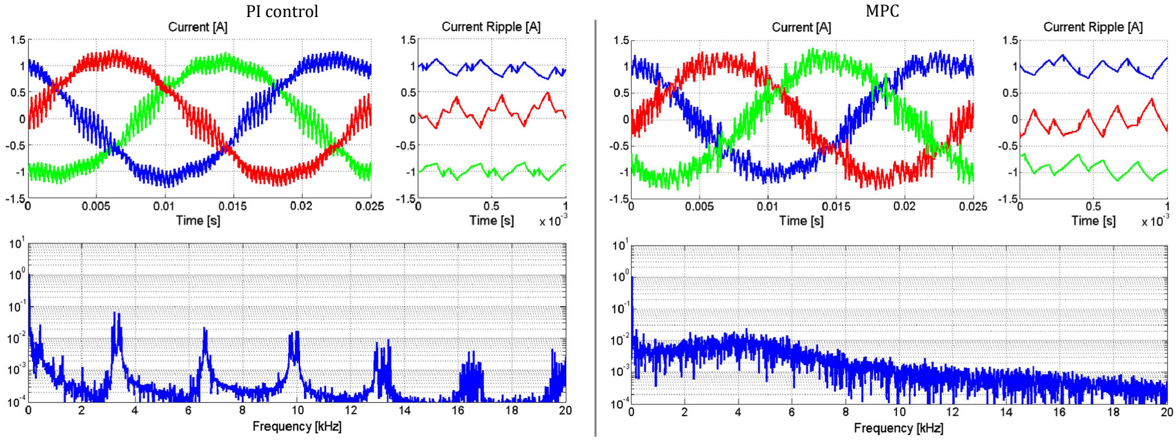

Figure 2.11: Comparison of Fourier analyses of the MPC currents and cascaded PI control currents [13].

In [37] MPC and PI control in the inner loop of a field oriented controlled drive system are compared. The MPC is more vulnerable to a parameter variation of the main inductance in the system with a change of at least 30 percent. In experimental work a slightly faster dynamic response was observed with the MPC in comparison to the PI controller for the inner current control. Also, a reduction of current ripples was reached with the MPC [37]. Figure 2.12 shows a comparison of MPC and PI control for a acceleration from standstill to operating speed. The machine performance of both control schemes is almost identical.

A comparison between FOC-based MPC and MIMO-based MPC has been done in [46] for a permanent magnet synchronous machine (PMSM). The control of the PMSM differs from the induction machine. However, different results in control quality of FOC-based MPC compared to the MIMO-based MPC that applies for the control of

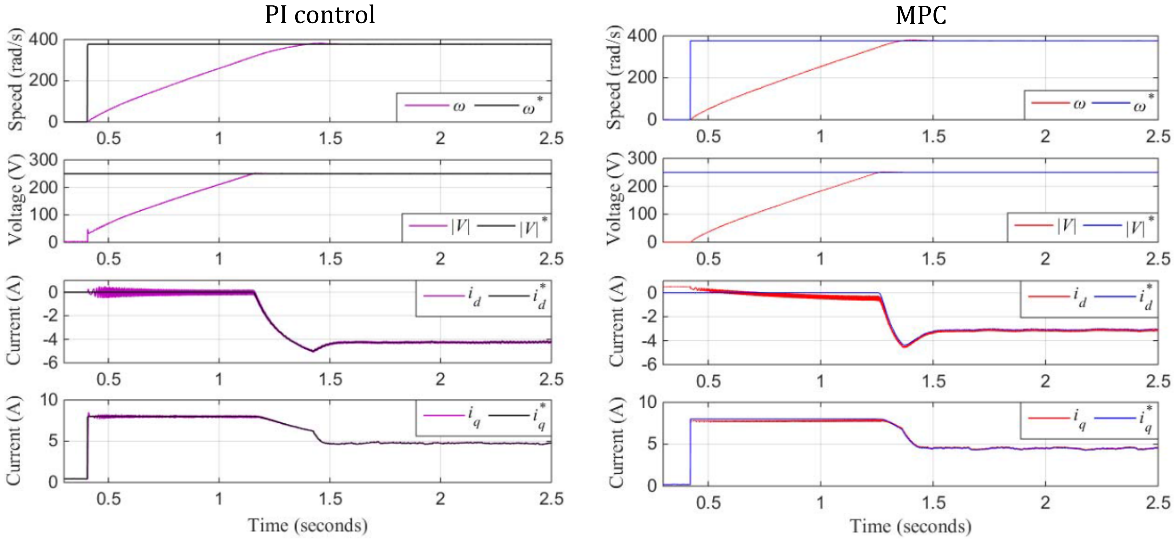

Figure 2.12: Comparison of the MPC currents and cascaded PI control PWM currents [37].

the PMSM also applies for the control of the induction machine. In simulation and experiments the MIMO-based MPC achieves less ripple in stator current and torque. These study has been done for steady-state and dynamic operation. The advantage of the MIMO-based MPC is a more precise predicting model of the machine as nonlinear behavior does not need to be linearized. This enables more precise control of the rotor especially for low-speed operation where linearization errors have most impact.

The FCS-MPTC is verified as having comparable performance with the field-oriented control method [11]. The calculation effort of FCS-MPTC is higher compared to conventional FOC. The calculation effort for increased prediction horizons rises in the same way as described for the FCS-MPC. In real systems, a large calculation effort burden means long sampling intervals and a low switching frequency, which increases the ripple in torque and stator currents [45].

In high power servo drive applications, classical cascaded PI control-loops reach their limits, when it comes to position control. The necessary higher level velocity control and current control need a higher bandwidth compared to the previous controller, each. Consequently, inadvertent high switching frequencies would be necessary. Thus, model predictive DTC is employed in ABB's ACS 6000 medium-voltage drive series [47]. In experimental performance evaluation a noticeable switching frequency reduction while maintaining the same control quality in the drive output variables as the motor torque, the stator flux and the inverter's neutral point potential could be achieved in comparison to standard DTC.

These comparisons in literature show that there is not a specific method to control electric drives that is superior in all aspects. However, MPC enables to reduce the ripple in current control but has higher calculation effort compared to conventional FOC. Control structures that are not based on FOC and directly regard the equations of the electric drive like the MIMO-based MPC and the MPTC can increase the bandwidth of the control, as no cascaded control loops are used, in which outer control loops need to be slower as the next inner loop. The MPC-based approaches have no disadvantage in control quality compared to conventional control, but they need more computational effort which concludes in more complex control hardware.

In this thesis a thermal model is used to optimize the control of an induction machine towards increased lifetime of the power electronics in the driving inverter. Since multiple inputs and constraints are necessary to fulfill this goal, a MPC-based approach seems the best choice. However, applications that require critical bandwidth are not aimed in this thesis and a comprehensible structure is more important. Therefore, a FOC-based structure with FCS-MPC for the current control is chosen. As the FCS-MPC of the current is directly applied on the power electronics in the inverter, it is possible to include thermal and lifetime related behavior to the control. This is done in chapter 5.. Another possibility is to add thermal and lifetime related behavior to the outer control loop of the FOC, which is done in chapter 6..

3. Reliability in power electronics

From the engineering point of view, reliability is the probability that a system or component will perform a required function without failure under stated conditions for a specified period of time [48]. It is distinguished from robustness, which is the ability of a system to operate adequately over a specified range of parameter variations. The reliable operation over the designed lifetime is essential for any power electronic system [49], particularly because the reliability of power electronics is becoming a prerequisite for the system safety in several key areas like energy, medicine and transportation [50].

Demanding operation environments challenge the reliability aspects of power electronics [51]. Depending on the application of a specific system, several stressors like high temperatures, temperature cycling, humidity, dust, vibration, EMI and radiation can endanger the safe operation of its components. The large number of fragile components in power electronic systems includes semiconductors, capacitors, magnetics, controllers, sensors and auxiliary devices. Failures of a single component cause downtime of the whole system and costs for maintenance.

3.1 Components in power electronics systems

With increasing demands on power electronics in terms of its functions and performance, the complexity of these systems rises. For demonstration, the system level schematics of a wind power system, photovoltaic system and electric vehicle are shown next. The system components are grouped in categories given in Figure 3.1.

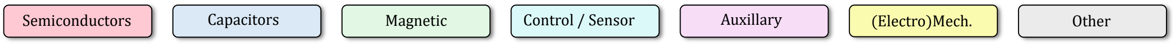

Figure 3.1: Categories to group components.

The block diagram of a generic wind power system is shown in Figure 3.2. Mechanical components include the rotor, pitch and yaw system, gearbox and wind measurements. The generator side converter is controlled using maximum power point tracking (MPPT). A grid side converter handles the grid feeding.

The photovoltaic system shown in Figure 3.3 gives a more detailed view of a power electronic system, as it also covers the relays to disconnect from the grid and relays for bypassing the boost converter to increase efficiency.

A system overview of an electric vehicle and a charging station is given in Figure 3.4. In addition to the electric drive system (electric motor and inverter), various electromechanic auxiliary subsystems are additionally present. An on-board rectifier for

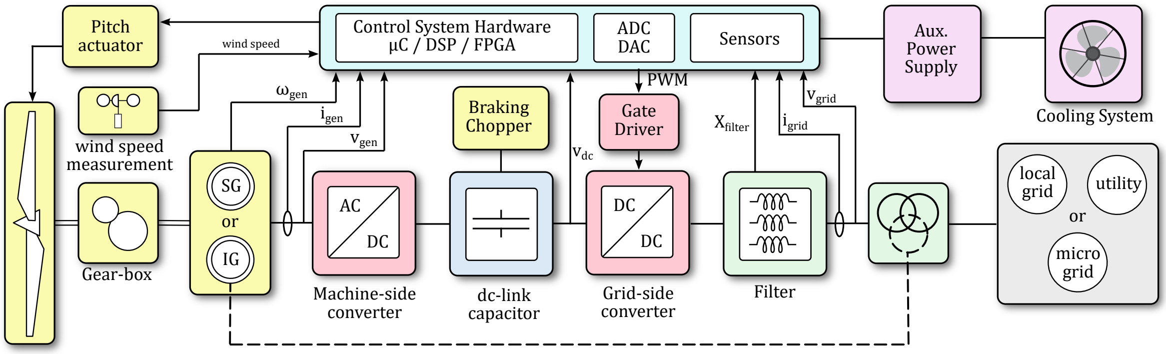

Figure 3.2: Components of a wind power system.

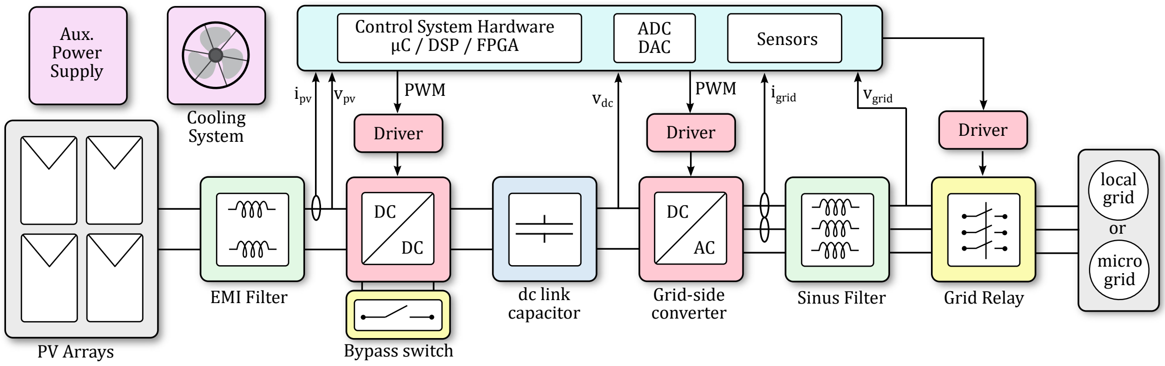

Figure 3.3: Components of a photovoltaic system.

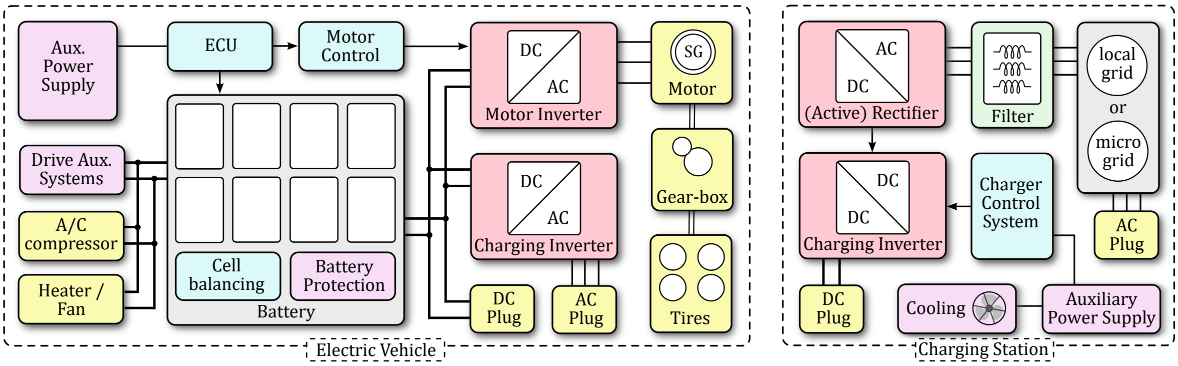

Figure 3.4: Components of a electric vehicle system and charging station.

AC-charging is installed and a much larger rectifier for fast dc-charging is present in the charging station.

The system level schematics show only the major components and do not include components such as data-busses, communication-links as well as sensing and protection circuitry. The large number of system components increases the risk of malfunction and failures. Therefore, it is very important to address not only the main components like the power semiconductors, capacitors and drivers but also the complete set of system components when examining the reliability of power electronics.

3.2 Empirical study on power electronics reliability

Most critical are the components where the gap between the actual reliability and the required reliability is the highest. To identify such components the targeted lifetime, typical stressors and failure mechanisms have to be analyzed.

Until now only very few wider survey-based investigations of reliability aspects of power electronics as seen by the experts have been accomplished. Most surveys were conducted within the wind power industry and deal with the wind park availability [52], the comparison of different turbine concepts [53] and the reliability of the subassemblies [54], [55], [56], [57]. However, all these investigations only encompass the analysis of failure rates of the components of power electronic systems. The only industry-wide survey reported in literature was conducted by Yang et al. in 2008 [58]. It also takes into account the analysis of stressors.

Therefore, the results of a comprehensive industry-wide survey that was recently conducted in collaboration with the international organization European Center for Power Electronics (ECPE) are used in the next sections of this chapter. The survey served to get an overview of the perceived reliability issues and the view on the current state of research in this field. It also helped to identify possible future approaches that may support further reliability improvements. In the initial section, the participants were asked to select for which application fields they would like to answer the application specific questions in the application specific sections. Each participant was able to perform the application specific part of the survey for multiple application fields. The distribution of the responses in the application specific part is given in Table 3.2. The later sections of the survey are applicable to power electronics in general and are thus based on the results of the 51 participants, as this section was only completed once by each participant.

Application	**Responses**
All	83
Wind Power	8
Photovoltaic	9
Electric Vehicles	21
Drive Systems	20
Traction	8
UPS & Power Supplies	7
Lighting	2
Air & Spacecraft	5
Energy Transmission	3

Table 3.1: Distribution of responses across the different application fields.

3.3 Requirements in lifetime and reliability

Today, the industry is in a paradigm change toward more reliable power electronics. Especially the automotive and aerospace industry have raised the reliability requirements of their power electronic systems due to safety requirements [1]. The definition of reliability given at the begin of this chapter shows three developments that can lead to demands for an increased level of reliability: The required function may become more complex or difficult to fulfill, the stated conditions may become harsher and the specified period of time may increase. For most applications, the required function and the operating conditions are fixed. The required target lifetimes depend on the application, power scale and the target market [59].

To find out the expected lifetime of power electronic systems in the in predetermined applications the survey participants were asked on the target lifetime of power electronics manufactured by their company. Multiple selections were possible. The responses are given separated by application fields in Figure 3.5. Very few respondents indicated that lifetimes shorter than 5 years are typical. Instead, for the most applications, the target lifetime between 5 and 20 years appears to be the norm. A longer target lifetime of 20 to 30 years is expected in wind power systems. These results agree with the investigations of Yang et al. in 2008 [58] and with identified target lifetimes in Wang et al. in 2014 [59]. Further this indicates that the expectancy on power electronic system lifetimes has not changed significantly in the last decade.

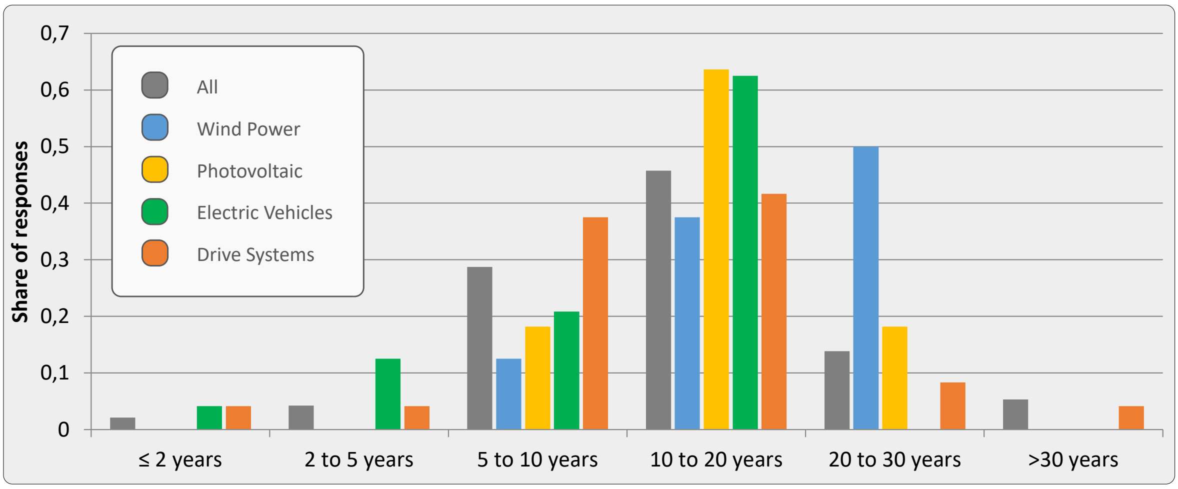

Figure 3.5: Typical target lifetimes of power electronics by application.

3.4 Component failure mechanisms

To facilitate the target lifetimes of the whole system the reliability of all system components needs to be ensured. In this section, the failure mechanisms and the resulting failure modes are given for selected components of power electronic systems. They are evaluated regarding their effect on the reliability. A focus is set on failure mechanisms of IGBT modules, as the general goal of this thesis concentrates on the reduction of the thermal stress in those devices.

3.4.1 Power semiconductor failure mechanisms

Failures of power semiconductors can be attributed either to failures occurring on chip level or to failures occurring in the package of the semiconductor. In literature, many reviews that describe the various relevant failure mechanisms can be found [60], [61], [62]. IGBT modules are offered in a variety of variants by the manufacturers. Three-phase full straps, half bridges and individual switches are usual but also more complex topologies which are optimized on special application fields, like use of photo voltaic voltage source converters or the connection to electric engines are sold. The advantages of the integration into a single component lie in the saving of material, volume and assembly working time. Besides the power semiconductors also sensors, protective mechanisms and drive electronics become increasingly integrated into the modules [63].

Failures on the packaging level are often the consequence of continuously varying thermal stress applied on the interconnections between the semiconductor device and the external contacts of a power module. To be able to discuss the main failure mechanisms of IGBT modules the internal structure of an IGBT module is represented schematically in Figure 3.6.

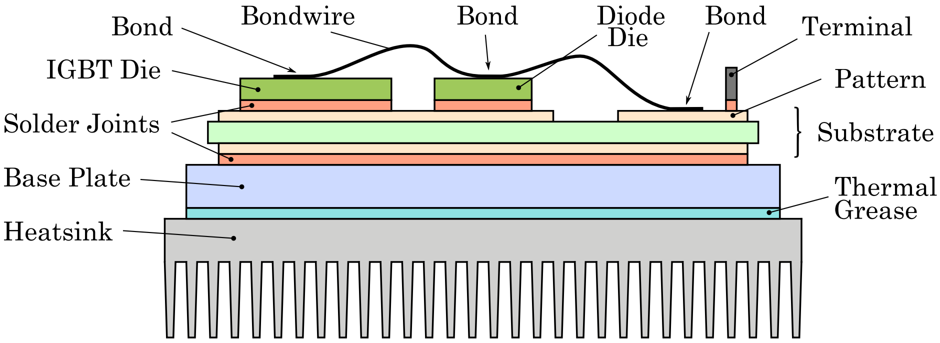

Figure 3.6: Layer sequence of an IGBT-module connected to a heatsink.

The top layer contains the IGBT and power diode semiconductor chips. They are connected to the substrate using solder to reach thermal dissipation and mechanical fixing to the substrate.

For the electric connection between the semiconductor contacts and the terminal connection contacts led out from the module, bonding is normally used. Therefore an aluminium wire is fastened with a cold welding procedure on both of the surfaces of the contact partners. To make sufficient current intensities possible, several bonding wires are transferred in parallel. The diameter of the bond wires depends on the module's current rating.

The next layer is a substrate, which works as insulator between the current carrying semiconductors and the electric conductive base plate. Aluminium oxide is frequently used as a substrate material, since it is both, an electric insulator and it has a good heat conductivity to lead away the dissipation power caused in the chips [63]. The substrate is connected to the base plate by an extensive solder joint.

The base plate represents the outermost layer of the module. It serves a superior heat expansion within the area of the module and also increases the mechanical stability. To maintain a low thermal resistance of the base plate, a material with high thermal conductivity, such as copper, is usually used [63]. The dissipation of the heat happens by the use of a heatsink. To lower the thermal resistance between the module's base plate and the heatsink, thermal grease is used.

The different materials of the module components extend differently on temperature changes. The coefficient of thermal expansion (CTE) of the most common used materials are represented in table 3.2. As a consequence, when changing the temperature, mechanical tensions occur at the connection points between chip and substrate, between substrate and base plate as well as at the contact points of the bonding wires due to their extension.

Material	**CTE**	**Thermal conductivity**
Silicon	$4,1 \cdot 10^{-6}\,\mathrm{K}^{-1}$	$148\,\mathrm{kW\,K}^{-1}$
Aluminium	$22,5 \cdot 10^{-6}\,\mathrm{K}^{-1}$	$230\,\mathrm{kW\,K}^{-1}$
Aluminium oxide	$8,3 \cdot 10^{-6}\,\mathrm{K}^{-1}$	$24\,\mathrm{kW\,K}^{-1}$
Copper	$17,5 \cdot 10^{-6}\,\mathrm{K}^{-1}$	$394\,\mathrm{kW\,K}^{-1}$
Solder	$22,5 \cdot 10^{-6}\,\mathrm{K}^{-1}$	$70\,\mathrm{kW\,K}^{-1}$

Table 3.2: Coefficients of thermal expansion and thermal conductivity of selected materials used in IGBT modules [63].

For cyclic heating and cooling processes, so called thermal cycles, the resulting expansions and contractions of the material at sufficiently frequent repetition lead to fatigue of solder joints and thus affect the heat dissipation in the module [64]. Particularly problematic is the solder of between substrate and base plate due to its large surface. Also, the high CTEs of aluminum and solder leads to mechanical stress at the bond wires fixation points.

In Figure 3.7, the solder joint between substrate and the base plate is represented by acoustic microscopy at four increasing time points of operating, measured by the number of thermal cycles. The test parameters were chosen as follows: Thermal cycle amplitude $\Delta T = 80\,\mathrm{K}$, maximum temperature $T_{max} = 105\,^{\circ}\mathrm{C}$ and period of a thermal cycle $t_{cycle} = 300\,\mathrm{s}$. It can be seen that the fatigue of the solder attaches at the corners

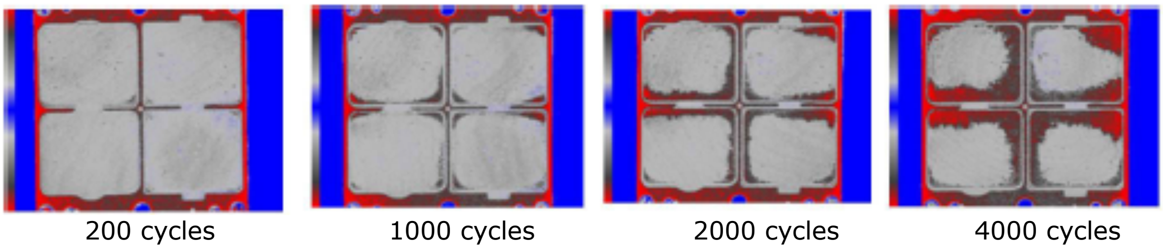

Figure 3.7: Acoustic microscopy images of the solder joint between the substrate layer and the base plate of an IGBT module exposed to thermal cycling [65].

after operating 1000 thermal cycles under the given test conditions. After 4000 cycles about a quarter of the surface of the solder joint has decomposed.

The consequence of the missing solder is an increasing thermal resistances within the module, in this case between the substrate and the base plate. This in turn leads to a deterioration of the overall thermal resistance between the junction of a semiconductor and the heat sink. The consequences are increased temperatures in the chips, and thereby, increased losses. This forms a positive feedback loop, which accelerates the aging process [66].

Due to thermal cycles also the length of the bonding wires changes periodically and thus mechanical stress on the joints arises. Is a point of contact fatigue, the bonding wire will dissolve and thus it is no longer available for current flow. If multiple parallel guided bonding wires exist, the module is initially functional, but by the increased current load experienced on the remaining wires, the process of detachment of the other connections is accelerated.

Over a longer period of time this stress leads to the deterioration of the interconnects as wire-bonds and solder layers within power modules. The increasing degradation is referred to as aging [67].

Device level failures of power semiconductors can occur due to various failure mechanisms [68]. As long as devices are operated within datasheet parameters it may be safe to expect that issues such as parameter shifts and other degradations will not occur. However, overload stress applied to the devices can cause device failures. A specific failure mechanism that cannot be completely avoided is single-event-burnout induced by cosmic radiation. In the case of this specific failure mechanism, the robustness of the device and the applied voltage in the application can be analyzed to estimate whether the expected failure rate is acceptable for a given application [69].

Failures in the driver circuits can also be the reason for a malfunction of the system. An open circuit failure of the driver circuit disrupts the operation of the power electronic system. Delayed switching or short circuit failures can also harm the power semiconductor elements. Integration of driver circuits and sensors into power electronic modules can decrease the occurrence of parasitic elements due to lower paths of the current. However, amplifying circuits are sensitive to EMI, which can occur in direct closeness to the switching elements.

3.4.2 Capacitor failure mechanisms

Capacitors are components that are most prone to failures in power electronics [70]. The three main types of capacitors are aluminum electrolytic capacitors (Al-Caps), metallized polypropylene film capacitors, (MPPF-Caps) and multilayer ceramic capacitors (MLC-Caps). The wear out mechanisms depend on the type of capacitor. Al-Caps suffer from electrolyte vaporization that is accelerated at high temperatures and ripple currents. Electrochemical reactions are increased by voltage stress. The same stressors and humidity lead to dielectric loss in MPPF-Caps. MLC-Caps suffer from oxide vacancy migration and insulation degradation at the same stressors and vibration [59]. Wear out leads to a drift in the electrical parameters and can give rise to open circuit or closed circuit failure modes as shown in [71].

A well accepted lifetime model for electrolytic capacitors is given in [72]. The equation to describe the lifetime L_0 is:

$$L = L_0 \cdot 2^{\frac{T_{max}-T_h}{10K}} \cdot 2^{1-\left(\frac{I_a}{I_0}\right)^2 \cdot \frac{\Delta T_0}{A}} \cdot \left(\frac{V_a}{V_0}\right)^{-m} \tag{3.1}$$

In this equation T_{max} is the maximum permissible temperature, I_a is the applied capacitor current, I_0 is the rated capacitor current, ΔT_0 is the temperature increase when I_0 is applied, A is the temperature coefficient, V_a is the applied voltage, V_0 is the nominal voltage, and m is a manufacturer dependent voltage factor. The model consists of three parts, where each part is considering one of three major stressors: First the impact of the hotspot temperature T_h follows the Arrhenius rule, which constitutes a doubling in lifetime for each 10 K temperature decrease. Second is the ripple current which is acting on the temperature rise. Third the applied voltage is taken into account, as an increasing voltage level causes degradation due to electrolyte evaporation effects [72].

3.4.3 Printed circuit board failure mechanisms

Printed circuit boards (PCBs) have to maintain their electrical and thermal capabilities in electrical lines and solder joints. Vibration is a main stressor for PCBs. Different resonance frequencies of soldered components and the PCB itself lead to mechanic strain and finally fatigue on the interconnections, which are the solder joints. The relation of vibration to other stressors like frequency [73], temperature [74] and power cycling [75] were investigated. Humidity caused by both split water and condensation, can compromise board functionality [76]. Deformation and tension during the assembly of the PCB in the case can lead to damaging of the soldered components [77].

3.4.4 Critical Components

The analysis of stressors, failure mechanisms and failure modes is used to conclude which components are prone to failures. Semiconductors and capacitors are used in the power stage of the system. As these components have a failure mode of short circuit, they are a potentially high risk regarding the safety of the system. For both components, omnipresent stressors like temperature cycles and voltage stress are crucial. Therefore, these components have most reasons to be prone to failures.

For mechanical and electromechanical components and subsystems, vibration and chemical exposure are relevant stressors in addition to temperature. The occurrence of these stressors depends on the application and their operating place. Especially for electric vehicles wide spread environmental conditions may occur which stresses these components.

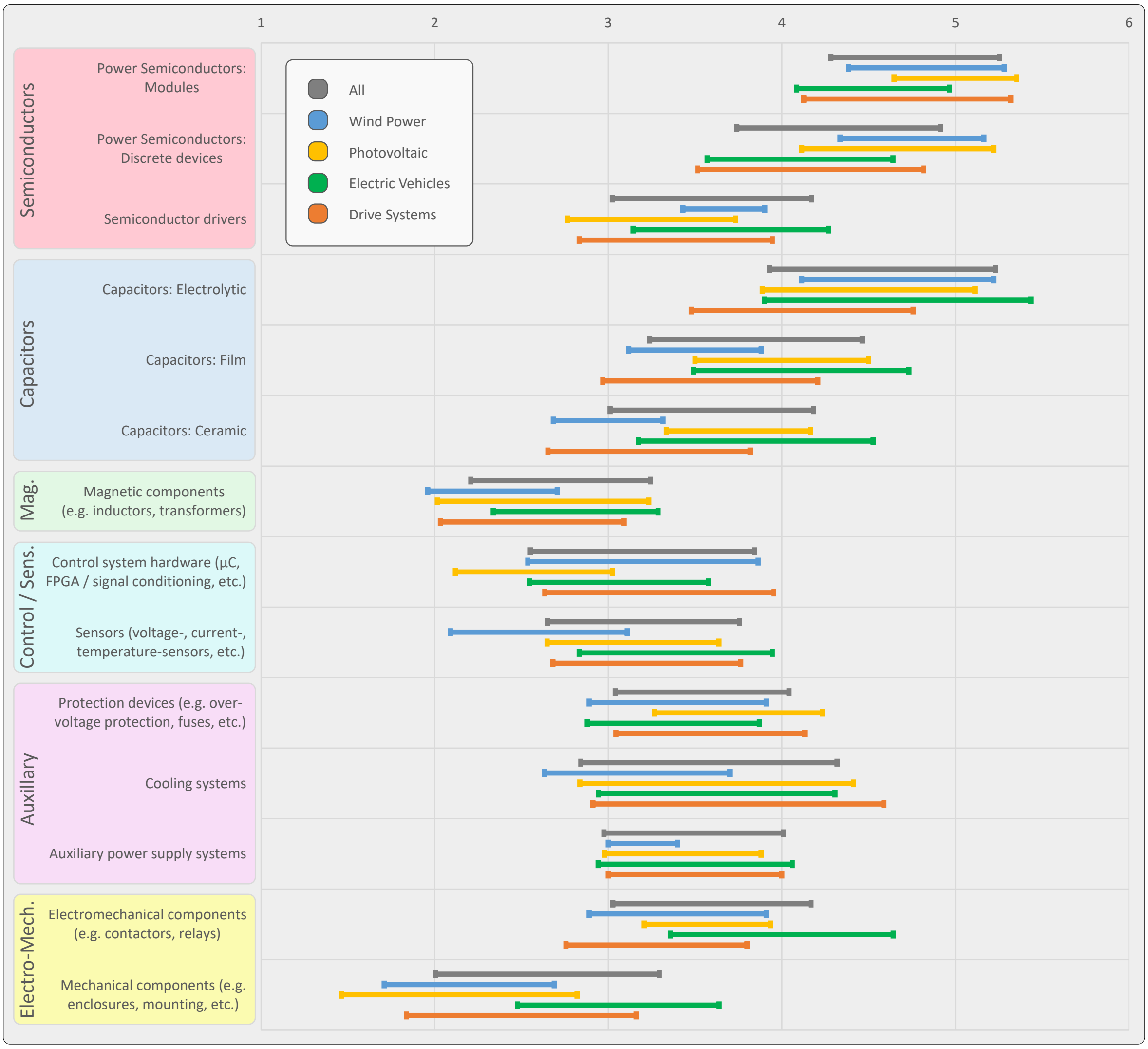

Figure 3.8: Critical components of power electronic systems by application. The bars show the standard deviation around the mean. The scale is from 1 (Not critical) to 6 (Very critical).

These results are also reflected in the conducted industry survey. It was asked for components of power electronic systems that are perceived to be susceptible to failure. The participating industry experts were asked to assign scores between 1 (not susceptible) and 6 (very susceptible) to each of the given components. The results are shown in Figure 3.8. The components evaluated to be most susceptible to failure across all applications are the semiconductors, both modules and discrete devices as well as electrolytic capacitors. This result is in agreement with the results of a previous survey conducted in 2008 [58]. Film and ceramic capacitors are next, followed by semiconductor drivers, electro-mechanical components and protection devices and cooling systems. It was further analyzed how the evaluation of the components in terms of their susceptibility to failures varied for the different application fields. The results appear to show little difference between the applications. However, for the application of electric vehicles mechanic and electro-mechanic components are considered more susceptible to failure than in the other applications.

3.5 Critical Stressors

The components in the power electronic systems are exposed to stressors that depend on the application and the operating conditions. Thus the knowledge of the application relevant stressors is extremely important.

Temperature related stressors affect the reliability of several components of power electronic systems, like the printed circuit boards (PCB) [74], the semiconductors [78] and the capacitors [79]. For semiconductors it is distinguished between the average and the cycling of the junction temperature [67]. In addition, thermal cycling evoked by ambient temperature and temperature cycles evoked by self-heating of the components also known as power cycling are distinguished [80]. The temperature related stressors are omnipresent stressors, which makes them more relevant. At the same time, thermal cycling due to internal losses is hard to avoid.

Power electronic systems are exposed to a wide variety of ambients including the ones with high humidity. Humidity builds up within the enclosure of the system leads to water condensation, which can cause corrosion [81]. The exposure to cycling ambient temperatures typical for night-day cycles causes significant increase of the water vapor concentration [82]. The effect of humidity on printed circuit board assembly is studied in [76].

Mechanic impacts such as vibration and shock primarily affect the robustness of mechanical components and interconnections of electric components [83]. Like most reliability concerns, processes of mechanical fatigue are multi-parameter problems [74]. The combined effect of thermal cycling and mechanical vibration on solder connections is investigated in [75]. The results show that the solder crack propagation on PCBs is increased for the combined stressors compared to the individual stressors.

Sources of electromagnetic interference (EMI) can be found in the power electronic system itself, other electronics within range and the grid. They can endanger the undisturbed operation of the system [84]. Terrestrial cosmic radiation can cause single-event-burnouts on power semiconductors, which has been experimentally shown in 1994 [85] and is still topic of active research (e.g. [86]). The harmfulness of EMI depends on the possible shielding and density in which the power electronic system is installed.

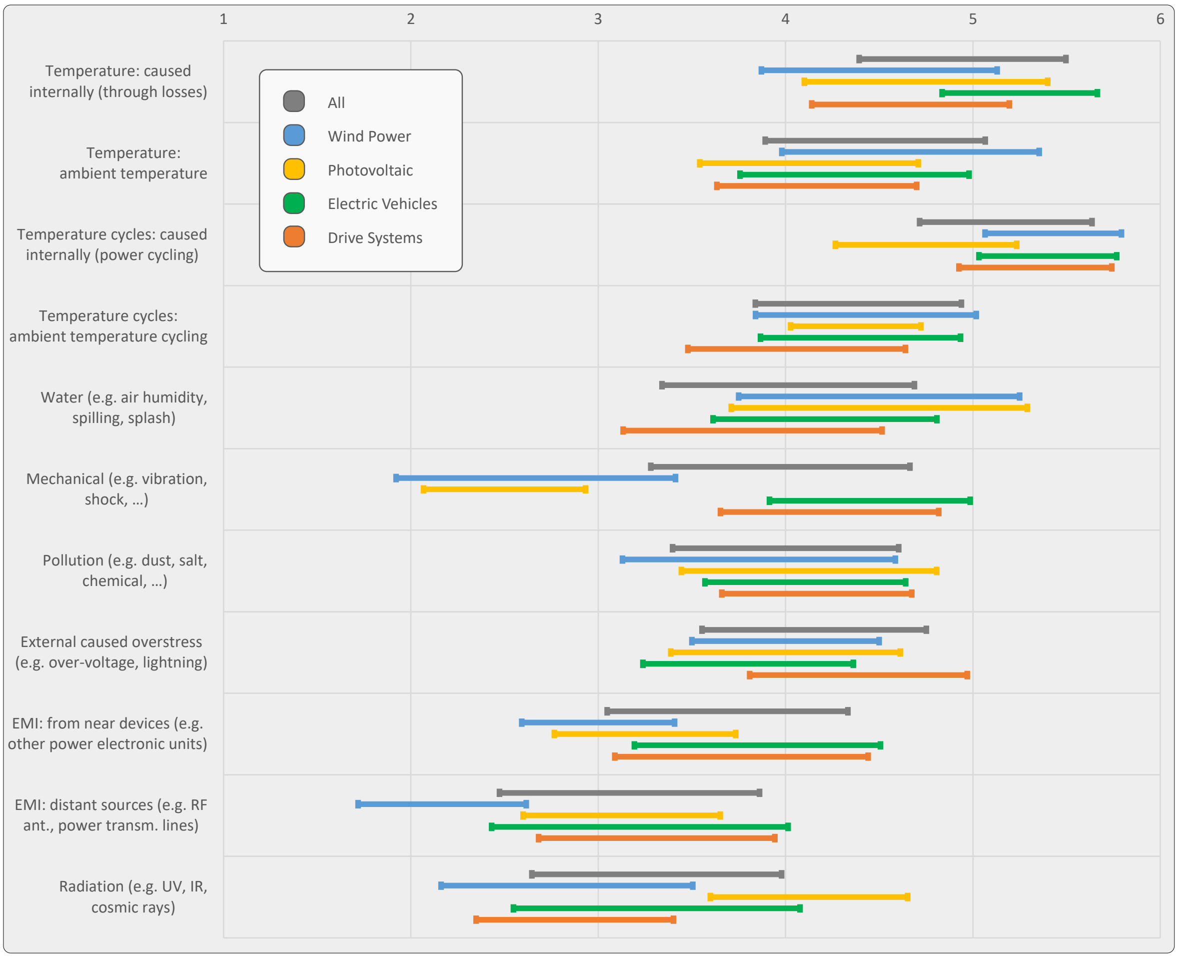

Figure 3.9: Critical stressors for power electronic systems by application. The bars show the standard deviation around the mean value. The scale is from 1 (Not critical) to 6 (Very critical).

The industry survey was formed by considering the founding of those research and with cooperation of industry experts. The participants were asked to rank the discussed stressors according to how critical they are considered to be for the selected application. This is given in Figure 3.9. The results aggregated across all applications show that almost all of the considered stressors were judged critical as all received mean scores lie above 3.5. All thermal stressors were considered particularly critical with power cycling identified as the most critical stressor. It can also be observed that mechanical stress such as vibration is certainly application dependent. For many other stressors there is only little difference between the applications. The results were broken down into the different application fields to identify particularly critical stressors in the different applications.

3.6 Components to focus in research

Based on the previous analysis on stressors and components along with their possible failure mechanisms and failure modes a reasonable focus of future research is detected. Components that are prone to failures are more important to be addressed research. These are the switching devices, capacitors, electromechanical components and cooling systems. This coincides with the investigations in [70].

The industry survey participants were asked to define components that are most important to be addressed by future research to improve the reliability of power electronic converter systems. For this question, free text answers were used. The responses were assigned to the previously used categories. This is shown in Figure 3.10. It is apparent that the majority of participants wish to see more research to focus on power semiconductors and power semiconductor modules as well as capacitors. In the area of capacitors, electrolytic and film capacitors were named most often. In some of the free text responses, no specific components were named but it was claimed that in general components that are exposed to hash environments such as high temperature or humidity should be addressed.

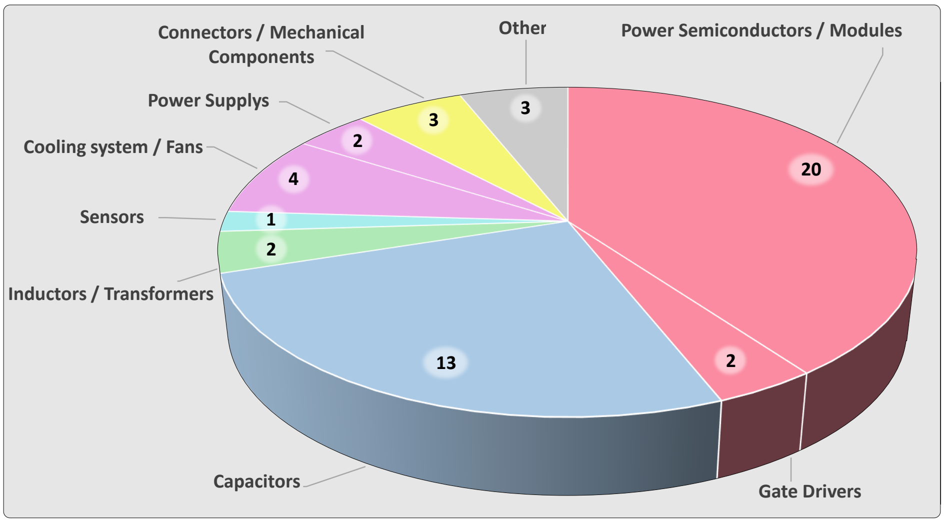

Figure 3.10: Components of power electronic systems to be addressed by future research.

3.7 Active methods to improve reliability to focus in research

A possibility to improve reliability is to increase the robustness of the components. Instead of increasing the capability of the hardware to take more damage, the control of device can be adressed to reduce the stress that occurs in the component. To evaluate the potential of such methods in improving the reliability, it was asked which trends would improve the system reliability of power electronic converters in the future. This is shown in Figure 3.11 and Figure 3.12. Hardware related methods are colored in blue and software related methods are colered in green. The results show that all mentioned trends are evaluated as overall beneficial, as the mean values lie between 3.6 and 4.2. However, there is a relatively wide spread in the scores which shows that the different participants have varying views on the benefit of these trends.

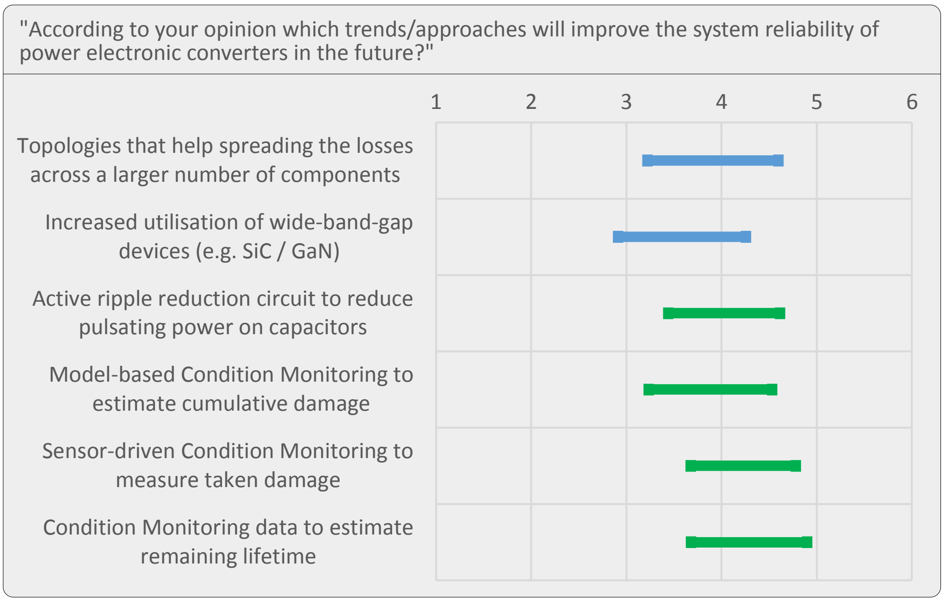

Figure 3.11: Trends or approaches that will improve the system reliability of power electronic converters in the future. Scale: Not beneficial 1 to very beneficial 6. The bars show the standard deviation around the mean.

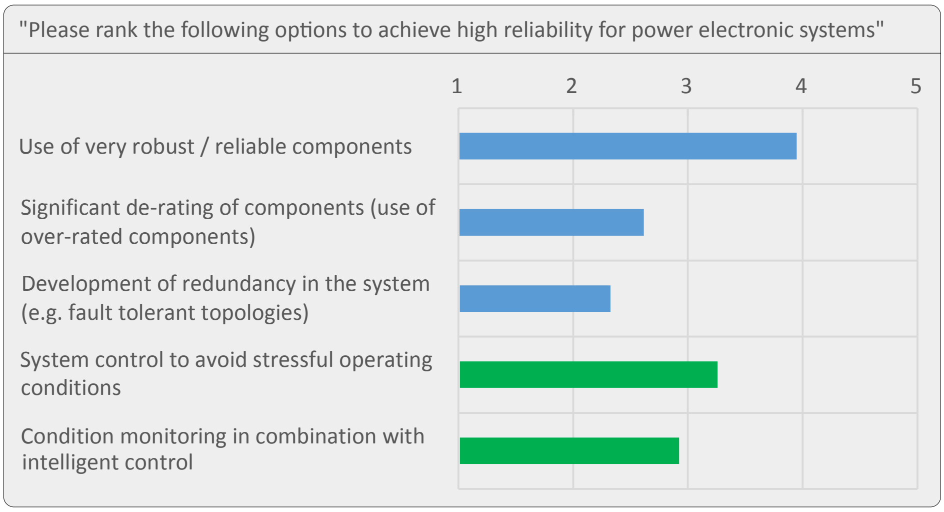

Figure 3.12: Methods to achieve high reliability for power electronic systems. Highest priority 5 to lowest priority 1. The bars show the mean values of all answers.

Experimental verification of active methods to improve the reliability is complicated. The components have a rated lifetime in the scale of years which makes real-time lifetime tests time consuming. Also constant test conditions like humidity or radiation have to be kept constant during the whole test. Therefore, lifetime related models [63] and accelerated lifetime tests [87] are used to estimate the lifetime of the components. However, the considered parameters and the accuracy of these approaches are limited. The commonly applied lifetime models for IGBT and capacitors rely on empirical data and estimation of the junction temperature cycling. A frequency-domain approach is provided [88], but field verification is still pending. The lack of easy applicable verification methods [89] is a general issue in reliability research.

3.8 Conclusion of the chapter

A comprehensive industry-wide survey has been conducted to analyze which topics future R&D should concentrate on and how to perform this research. Firstly, typical target lifetimes of 5 to 30 years with a strong dependency on the application field were identified. The investigation on stressors that limit these requirements showed that all thermal stressors were considered particularly critical with power cycling identified as the most critical stressor. Along the same lines, semiconductor devices were identified the most critical components closely followed by capacitors. Also the cooling system, protection devices and electromechanical components were identified critical. This corresponds with the components that should be addressed in future research. Active methods that help to increase the reliability during operation like condition monitoring and avoiding stressful operating conditions were indicated only slightly positive. However, there is potential in these methods as the majority wish to see more research on these topics.

4. Methods to improve reliability of power electronic modules

In the previous chapter was shown, that the reliability of a system is an essential indicator for any power electronic system. Stressors like temperature, humidity, radiation and mechanical impacts quicken the aging of power electronics systems and increase the probability of failures [90]. Harsh environments and uncertain conditions stress the safe operation [1].

This chapter starts with an overview on methods to improve the reliability. These methods can be divided in four main categories that represent the lifespan of a power electronics system from design to end of life (EOL) as shown in Fig. 4.1.

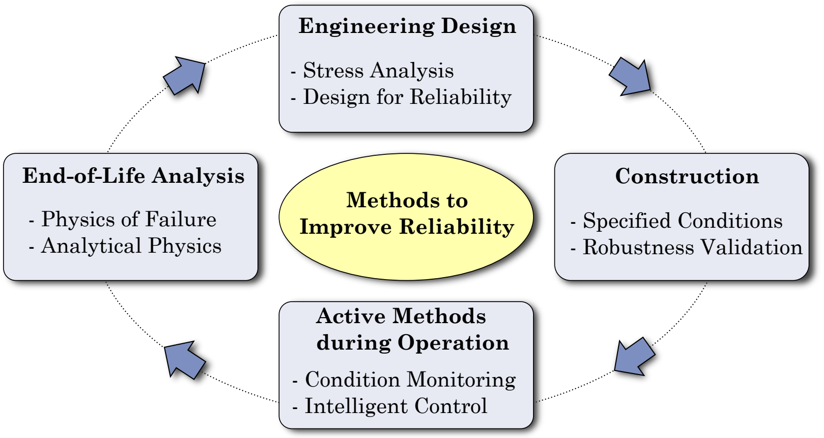

Figure 4.1: Methods to improve the reliability of power electronics systems from design to end-of-life.

The first category is the design process of the system's components. In this process the term Design for Reliability (DFR) is key [91], [71]. Its goal is to assure sufficient robustness of the system by proper engineering [59]. Load profiles for the components are computed regarding the stressors that occur during field operation [92]. Using the stress analysis, the necessary strength of the system is determined [93], which is usually a multi-parameter problem [94].

The second category is the construction of the components and system. In the construction process of the system's components product testing routines are used to detect abnormal performance that may lead to early failures in the final product.

The third category is active methods to improve the reliability. These are software-based control structures that are applied during operation. The goal is changing system operation to release stress from its components while allowing none or only minor influence the overall performance. In collaboration with condition monitoring, which allows to obtain the health status of the system's components [62] and is used to predict reliability [95]. An intelligent control can drive components with respect to their remaining lifetime.

The last category is the end-of-life analysis. The triggering failure mechanism is tracked down to its root cause in order to improve the weak point in the design stage of upcoming product versions. This procedure is a Physics of Failure approach.

In the following, methods to improve the reliability are studied with a focus on the active methods for power semiconductor modules.

4.1 Physics of Failure Approach

Physics of Failure (POF) is an approach that employs the knowledge of the root cause of failure mechanisms to improve product reliability. The concept is based on the understanding of the relationships between requirements and the physical characteristics of the product and the reaction of product elements to stressors and their influence on the degradation with respect to the use conditions and operating time [59]. The influence of stressors to product components and materials is evaluated according to their influence on the fitness for use. Further variables are their variation in the manufacturing processes, use conditions and time of service [62]. This approach has been applied to increase lifetime and reliability of power electronic modules [78].

Analyzing of product returns allows detecting components that are prone to failures in a system. This led to several improvements to increase the strength. These improvements can be changes of the material properties as well as optimized utilization to relieve critical stress: Improvements in the connection technology and assembly of the modules have been done [61]. Sintering, also low temperature joining, instead of soldering of the chips is used to increase robustness of the connections and bonds are replaced by pressure contacts in high reliability product lines [63]. Delaminating of the substrate can be reduced by avoiding 90° angles on the pattern [96]. An overview of different approaches to increase the cycling capability is given in [97]. PCB layout and cooling flow can be optimized to enhance the capacitor cooling.

Manufacturers of power semiconductor modules use a silicon gel filling inside the modules to protect it against corrosion and environmental influences as well as increasing the proof voltage. The gel is losing some strength of its protective properties during usage, but this is not a critical degradation concerning the lifetime of the module [98]. Fault tolerant topologies are discussed in [99].

4.2 Junction temperature detection

Aging of power electronic modules is the destruction of the component due to wear-out and fatigue of its materials. In section 3.4 the related failure mechanisms of power electronic modules were shown with the result that thermal stress has a particular meaning for their destruction. As the general goal of this thesis concentrates on the reduction of the thermal stress of power electronic modules, thermal- and stress-based modeling of those devices is necessary for the their control.

Measurements of the junction temperatures are also possible, but the necessary high-bandwidth sensors are expensive and only used in experimental setups. As high potential for lifetime extension is in elimination of short-term thermal cycles [80], usual thermocouples connected to the chips cannot fulfill the bandwidth demand. Thus, in commercial product solutions, model-based junction temperature estimations that apply electrical measurements are more realistic as there is no need to increase complexity of power modules.

Therefore, in this section the power losses that occur in the modules are discussed first. The consequential thermal effects are depicted afterwards. In the end the impact of the temperature on the power module lifetime is given.

4.2.1 Power losses model

In power electronic systems usually the switching losses and conduction losses are the dominant losses [63]. The conduction losses of an IGBT $P_{cond,igbt}$ are computed in dependency of the collector current i_C and the collector-emitter voltage v_{CE}. This voltage drop is substantially dependent on i_C, the junction temperature $T_{j,igbt}$ and the applied gate voltage v_{GE}.

$$P_{cond,igbt} = i_C \cdot v_{CE}(i_C, T_{j,igbt}, v_{GE}) \tag{4.1}$$

Conduction losses in power diodes $P_{cond,diode}$ have a similar structure. They are depend on the forward current i_f and its forward voltage v_f characteristic, which is dependent on i_f and the junction temperature $T_{j,diode}$.

$$P_{cond,diode} = i_f \cdot v_f(i_f, T_{j,diode}) \tag{4.2}$$

For online computation the characteristics of the chips are placed in look-up tables. These can be written compact, as the characteristics have usually linear behavior in the main stages.

The amount of switching losses in IGBTs $P_{sw,igbt}$ depends on the switching energies E_{on} and E_{off}, which depend mainly on i_C, v_{CE} and $T_{j,igbt}$. Most manufacturers indicate the switching energies only for a specified operation point, so approximations have to be done for general calculation. A linear approximation for one fundamental period is given in [63], using the parameters of a given reference operating point from the datasheet i_{ref}, v_{ref}, $T_{j,igbt,ref}$ and scaling it to the desired operating point:

$$P_{sw,igbt} = f_{sw} \cdot (E_{on} + E_{off}) \frac{\sqrt{2}}{\pi} \frac{i_C}{i_{ref}} \left(\frac{v_{dc}}{v_{ref}} \right)^{K_v} \cdot \left(1 + c_{T,sw} \left(T_{j,igbt} - T_{j,igbt,ref}\right)\right) \tag{4.3}$$

The parameters K_v and $c_{T,sw}$ are empirically determined constants set to $K_v = 1.35$ and $c_{T,sw} = 0.003$. In power diodes reverse recovery losses $P_{sw,diode}$ occur during switch-off and their amount depends on the recovery energy E_{rr}. Similar to the IGBT switching energies, an approximation is given:

$$P_{sw,diode} = f_{sw} \cdot E_{rr} \left(\frac{\sqrt{2}}{\pi} \frac{i_f}{i_{ref}} \right)^{K_i} \left(\frac{v_f}{v_{ref}} \right)^{K_v} \cdot \left(1 + c_{T,rr} \left(T_{j,diode} - T_{j,diode,ref}\right)\right) \tag{4.4}$$

Again, the additional parameters K_i and $c_{T,rr}$ are empirically determined constants set to $K_i = 0.6$ and $c_{T,rr} = 0.006$. Anyway, these equations give only estimations of the switching losses which could deviate from reality, especially when the system works far from the reference values.

4.2.2 Temperature model

To estimate the IGBT and power diode junction temperatures of the module, the heat dissipation in the whole system has to be evaluated. For this purpose a thermal network, also referred to as thermal equivalent circuit diagram is used. The thermal resistance R_{th} can be considered as an electrical resistance that is giving a measure of how fast stored heat can be dissipated and the thermal capacity C_{th} as a capacitor that is storing heat in the thermal mass instead of charge. The thermal network is used to model transitions between and within material layers of the setup as thermal resistances and also regarding the components thermal capacities.

The thermal resistance is defined by the temperature difference between the place x and y that is set up when applying power losses P_{loss} [100]:

$$R_{th} = \frac{T_y - T_x}{P_{loss}} \tag{4.5}$$

The thermal capacitance can be expressed using the differential temperature change $\frac{dT_x}{dt}$ at place x [100]:

$$C_{th} = \frac{P_{loss}}{\frac{dT_x}{dt}} \tag{4.6}$$

This means, the energy $P_{loss} \cdot dt$ is used to apply a temperature change of dT_x at the material of x.

The time dependent thermal resistance is represented with the thermal impedance of the device and the thermal time constant τ_{th}. It can be obtained by measuring the heating up or cooling down temperature curve for defined power losses. It is defined as:

$$Z_{th}(t) = \frac{T_j(t) - T_j(t=0)}{P_{loss}} = \sum_{\nu=1}^{n} R_{th,\nu} \cdot \left(1 - e^{-\frac{t}{\tau_{th,\nu}}}\right) \tag{4.7}$$

Using the real-time power losses estimation of the IGBT and power diode junctions presented in the previous section, the dissipation of the released heat can be estimated in the physical setup. A linear Cauer-type thermal network can be used to describe the heat propagation in the power electronic system [100]. Necessary parameters for the thermal resistances and capacities are given in the module's datasheet. Modeling the performance of the attached thermal grease and heatsink is challenging, because the characteristic depends on the complete cooling system of the application and not only on the module itself. Therefore, a low-bandwidth temperature sensor on the modules substrate is included into the model. A sensor like that is often build into commercial IGBT modules. Its temperature measurement is notated T_c as is refers to the module's case temperature. The advantage is, that only the temperature difference between the substrate and the junctions need to be calculated and the temperature difference between ambient and substrate is not needed. This makes the control independent from the cooling system and results in a smaller thermal network having less computational effort compared to approaches using heatsink or ambient temperature measurement. A drawback is that short-term cycles of substrate temperature cannot be detected. However, due to the thermal capacitance of the substrate these fast cycles are small compared to the junction temperature cycles.

Figure 4.2 shows the Cauer-type thermal network. In the one-dimensional equivalent circuit diagram, the heat input P_{loss} is represented by a current source connected to the substrate temperature reference point. In between lays a network of the heat capacities C_{th} and the thermal resistances R_{th}. In the Cauer model, the capacities are inserted between the nodes and the reference potential. In datasheets a four-part thermal network is usually used to describe the transient from junction to case.

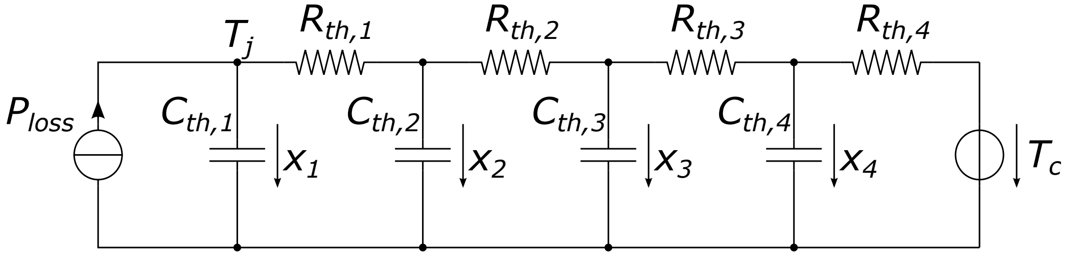

Figure 4.2: Cauer-type thermal network from junction to substrate.

To implement the thermal network on a control system, a discrete state-space model is built. Therefore a continuous state-space model is established first and a discretization is applied afterwards. The estimated power losses P_{loss} and the low-bandwidth case temperature T_c are used as input parameters. Outputs are the junction temperature estimations for IGBTs and power diodes. The temperatures of the thermal capacities are used as state-variables x_1 to x_4, as they are the energy storages in the thermal system.

The state equations can be deduced from the thermal network using Kirchhoff's circuit laws:

$$\frac{dx_1}{dt} = -\frac{1}{C_{th,1}R_{th,1}}x_1 + \frac{1}{C_{th,1}R_{th,1}}x_2 + \frac{1}{C_{th,1}}P_{loss} \tag{4.8}$$

$$\frac{dx_2}{dt} = \frac{1}{C_{th,2}R_{th,1}}x_1 - \frac{R_{th,1}+R_{th,2}}{C_{th,2}R_{th,1}R_{th,2}}x_2 + \frac{1}{C_{th,2}R_{th,2}}x_3 \tag{4.9}$$

$$\frac{dx_3}{dt} = \frac{1}{C_{th,3}R_{th,2}}x_2 - \frac{R_{th,2}+R_{th,3}}{C_{th,3}R_{th,2}R_{th,3}}x_3 + \frac{1}{C_{th,3}R_{th,3}}x_4 \tag{4.10}$$

$$\frac{dx_4}{dt} = \frac{1}{C_{th,4}R_{th,3}}x_3 - \frac{R_{th,3}+R_{th,4}}{C_{th,4}R_{th,3}R_{th,4}}x_4 + \frac{1}{C_{th,4}R_{th,4}}T_c \tag{4.11}$$

As the junction temperature is the only output of the system, the output equation is denoted:

$$T_j = x_1 \tag{4.12}$$

This continuous state-space representation can be transformed into matrix notation, using a system matrix A , an input matrix B, an output matrix C and a feed-through matrix D. The continuous state equation and output equation are notated as:

$$\frac{d}{dt}\,\mathbf{x}(t) = A\cdot\mathbf{x}(t) + B\cdot\mathbf{u}(t) \tag{4.13}$$

$$\mathbf{y}(t) = C \cdot \mathbf{x}(t) + D \cdot \mathbf{u}(t) \tag{4.14}$$

In these equations $\mathbf{x}(t)$ is called state vector, $\mathbf{u}(t)$ is called input vector and $\mathbf{y}$(t) is called output vector.

The content of the continuous matrices A, B, C and D are deduced from state equations (4.8) to (4.11):

$$A = \begin{bmatrix} -\frac{1}{C_{th,1}R_{th,1}} & \frac{1}{C_{th,1}R_{th,1}} & 0 & 0 \\ \frac{1}{C_{th,2}R_{th,1}} & -\frac{R_{th,1}+R_{th,2}}{C_{th,2}R_{th,1}R_{th,2}} & \frac{1}{C_{th,2}R_{th,2}} & 0 \\ 0 & \frac{1}{C_{th,3}R_{th,2}} & -\frac{R_{th,2}+R_{th,3}}{C_{th,3}R_{th,2}R_{th,3}} & \frac{1}{C_{th,3}R_{th,3}} \\ 0 & 0 & \frac{1}{C_{th,4}R_{th,3}} & -\frac{R_{th,3}+R_{th,4}}{C_{th,4}R_{th,3}R_{th,4}} \end{bmatrix} \tag{4.15}$$

$$B = \begin{bmatrix} \frac{1}{C_{th,1}} & 0 \\ 0 & 0 \\ 0 & 0 \\ 0 & \frac{1}{C_{th,4}R_{th,4}} \end{bmatrix} \tag{4.16}$$

$$C = \begin{bmatrix} 1 & 0 & 0 & 0 \end{bmatrix} \tag{4.17}$$

$$D = \begin{bmatrix} 0 & 0 \end{bmatrix} \tag{4.18}$$

The state equation and output equation of the discrete state-space are denoted:

$$\mathbf{x}(k+1) = A_d \cdot \mathbf{x}(k) + B_d \cdot \mathbf{u}(k) \tag{4.19}$$

$$\mathbf{y}(k) = C \cdot \mathbf{x}(k) + D \cdot \mathbf{u}(k) \tag{4.20}$$

To convert the continuous state-space into a discrete one sampled with sampling time T_s, following equations are used:

$$A_d = e^{(A \cdot T_s)} \tag{4.21}$$

$$B_d = e^{(A \cdot T_s - I)} \cdot A^{-1} \cdot B \tag{4.22}$$

$$C_d = C \tag{4.23}$$

$$D_d = D \tag{4.24}$$

Here, e is the exponential function for matrices and I is the identity matrix.

To estimate the junction temperatures of all semiconductors in the module several state-space models are used. However, this is a basic approach of arranging a thermal network having several inaccuracies. In this model cross coupling between semiconductors in module are neglected even though especially junctions that are placed next to each other on the module's substrate influence each other. In [101] a thermal network is used that considers this influence. These parameters are usually not provided in the module's datasheets.

To achieve unknown thermal element parameters without experiment also a finite element analysis (FEA) can be done [102], [103]. FEA is a numeric method to determine parameters of a thermal network using accurate geometric and material properties of a whole setup. But even these parameters are computed using a 3D model there is a information loss when converting them to a 1D thermal network having a finite amount of RC links. When determining parameters using a FEA, inaccuracies occur when entering the exact volume of applied thermal grease as it is hard to apply it with a precise thickness. Also its properties changes over time due to aging.

4.2.3 Electro-thermal model

To achieve the resulting structure of the full electro-thermal-model the power losses that are calculated in the losses model are used as an input to the thermal network. As both parts are computed at every sampling instant the resulting junction temperature can also be estimated online. The merged structure of the thermal-electro-model is shown in Fig. 4.3.

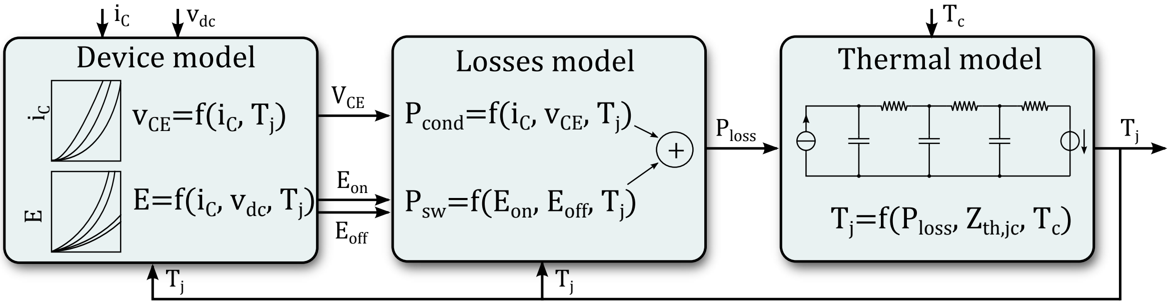

Figure 4.3: Online junction temperature estimation model.

The electro-thermal model uses measurements of the output current i_c, the dc link voltage v_{dc} and a low-bandwidth measurement of the module's case temperature T_c in the IGBT module. The first two measurements are realized in the system to operate to the current controller in the majority of systems. The case temperature sensor is often build into commercial IGBT modules, thus only a low-bandwidth sampling for this signal needs to be added to the control system. This makes the model-based temperature estimation a low-invasive solution to obtain the junction temperatures.

Another concept is to use a Luenberger-style closed-loop observer [2]. In this concept the case temperature is also used as an input parameter to feed a model of the heat dissipation of the setup, which contains the junction temperature is an accessible state. The feedback of the case temperature is used to ensure that the output of the model actually complies with the measurement of the real system. When input and output of the model comply with the real system, the internal states of the model have also a great accuracy. As the junction temperature is one of those states, it can be determined.

An alternative to the model-based junction temperature estimation is to determine it based on electrical parameters which have a dependence on T_j. They are known as thermo sensitive electrical parameters (TSEP) [104]. A first possibility is determining T_j via the voltage drop over the IGBT V_{CE} at a low current value (e.g. 100 mA). V_{CE} is rising as T_j increases [105]. Furthermore, T_j can be determined via the gate threshold voltage $V_{GE,thr}$. This voltage decreases as the T_j increases [106]. It is also possible to determine T_j via a transconductance g_m as a thermo-sensitive parameter. It is defined according to equation (4.25) [107].

$$g_m = \frac{\frac{dI_c}{dt}}{\frac{dV_{GE}}{dt}} \tag{4.25}$$

4.2.4 Parametrization of the electro-thermal model

The electro-thermal model has to be parametrized for use with a particular module. For the following demonstration in simulation and experiment it is now parametrized for a three-phase converter IGBT module that has a nominal collector current of 25 A and a maximum DC-link voltage of 1200 V.

The device model is parametrized using the output characteristic of the IGBT module. It is given in Figure 4.4. For the junction temperature detection is required to perform the calculation of the conduction losses online in each switching period. Therefore it is necessary to find a tradeoff between computation time and accuracy of the model. In [108] an approximation is done using a second order polynomial. Since the output characteristic has an approximately linear behavior for collector currents greater than approximately 10 A, the relationship can be stored in a computational light look-up table. The data points concentrate in the non-linear range of low collector currents.

The thermal model is parametrized using thermal impedance of the device. It is defined using the junction to case thermal parameters from the datasheet. They are given in

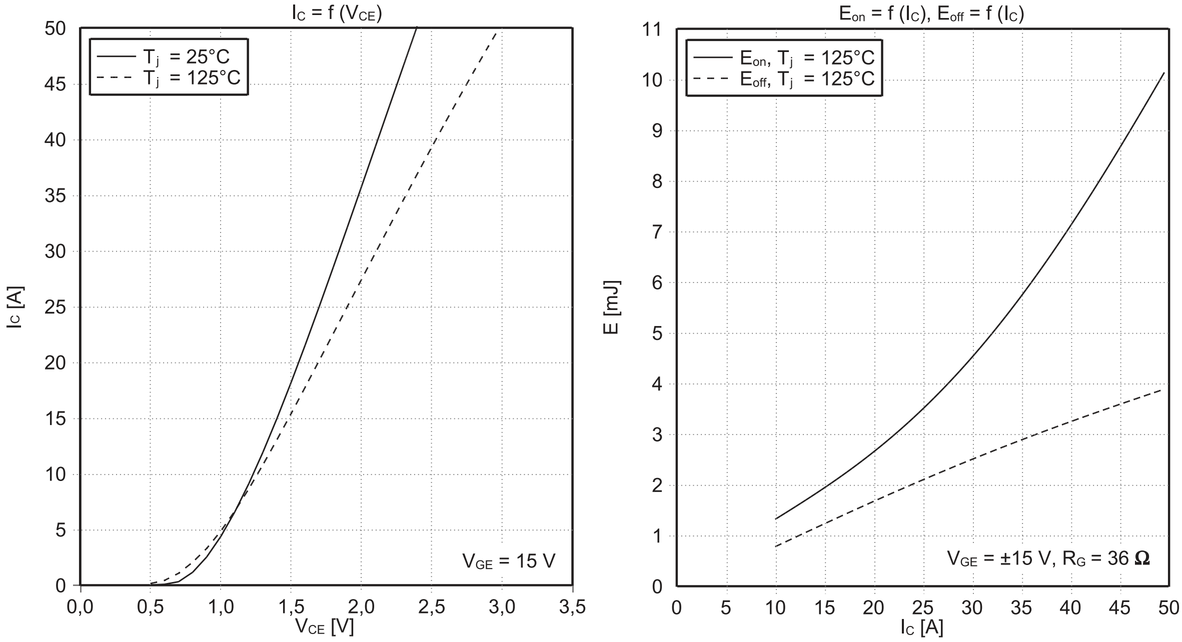

Figure 4.4: Output characteristic and switching energies of Infineon FP25R12KT3 IGBT module (taken from datasheet).

Table 4.1. As the designed model relies on a low-bandwidth measurement of the case temperature, a parametrization of the cooling system is not necessary.

	$i = 1$	$i = 2$	$i = 3$	$i = 4$
$R_{th,jc,i}$ in [K/W]	0.09025	0.3612	0.2031	0.1403
$\tau_{th,jc,i}$ in [J/K]	0.002345	0.0282	0.1128	0.282

Table 4.1: Transient thermal impedance parameters of Infineon FP25R12KT3 IGBT module (taken from datasheet).

The electro-thermal model is implemented in simulation and a comparison with the Plexim PLECS (Piecewise Linear Electrical Circuit Simulation) software is done. A transient process is simulated in figure 4.5. The electro-thermal model is in conformance with the PLECS model.

4.2.5 Experimental validation of the electro-thermal model

The junction temperature estimation provided by the electro-thermal model is compared to a direct temperature measurement. The experimental validation is done on a two-level dc/ac inverter in H-bridge topology. A three-phase inverter IGBT module with a nominal current $i_{nom} = 25\,\mathrm{A}$ and a maximum voltage $v_{dc,max} = 1200\,\mathrm{V}$) is used. The module is provided by the manufacturer without the use of isolating gel filling. This allows direct temperature measurements on the chips but decreases the isolation voltage below the rated values. For power input a 10 kW dc power supply is used. The load is ohmic-inductive. The control is implemented on a dSPACE DS1006 processor

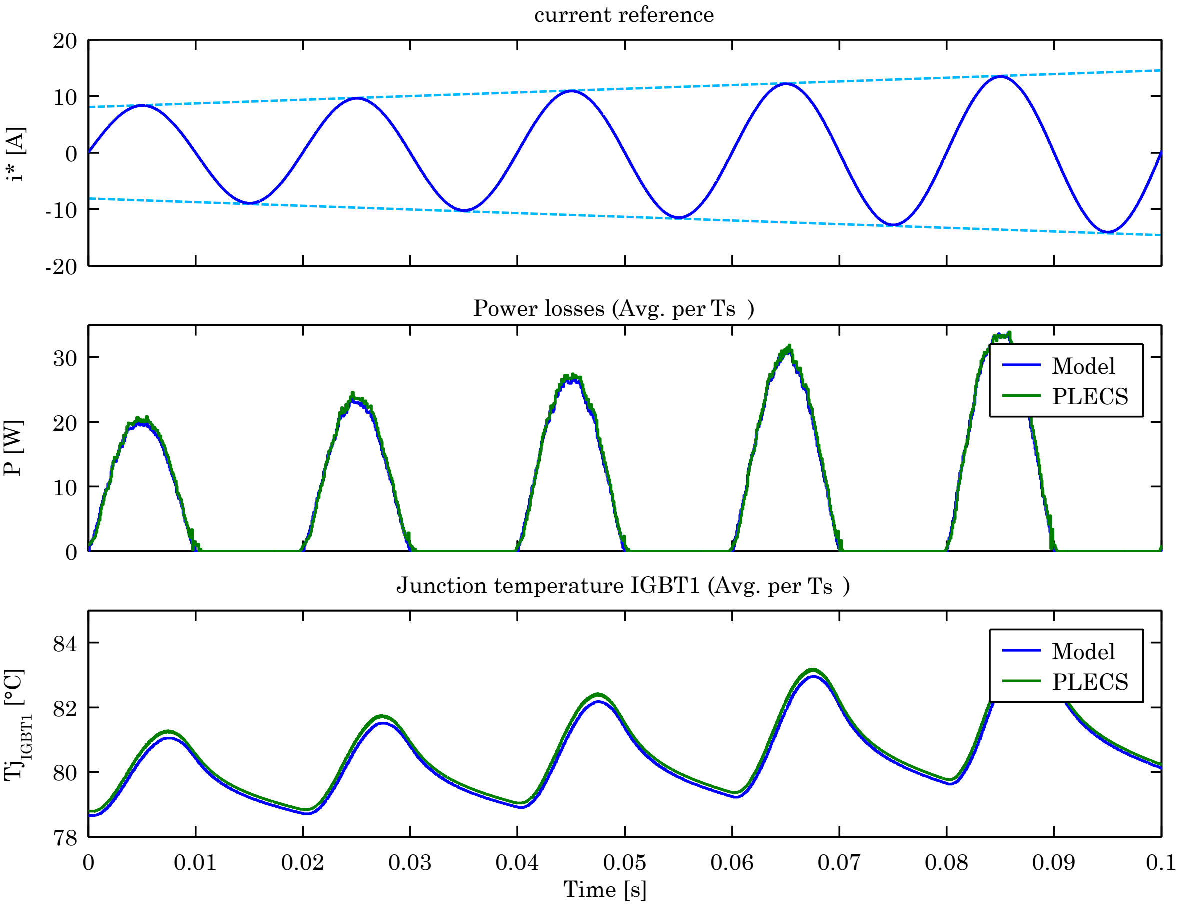

Figure 4.5: Transient simulation of the electro-thermal model in comparison with the PLECS model. Parameters: $v_{dc} = 650\,\mathrm{V}$, $f_{sw} = 10\,\mathrm{kHz}$, $f = 5\,\mathrm{Hz}$.

board. For junction temperature measurement an optic fiber sensor is used that utilizes the temperature-dependency of GaA crystal bandgap. The response time is rated 5 ms and the accuracy is rated ±0.8 K.

A series of experiments has been made to compare different operation points in switching frequency and fundamental frequency. An IGBT o the upper side of the H-bridge is chosen for the temperature measurement. Since the source of data and the principle of the junction temperature estimation is similar for all IGBTs and power diodes in the module it is expected to have similar results concerning model accuracy for the other semiconductors.

First, the switching frequency is modified while output power and fundamental frequency are fixed. The results are presented in figure 4.6. In the first row the switching frequency profile is given and temperature measurement versus estimation are given in the second row. For the junction temperature estimation the model in Figure 4.3 is used.

It can be seen that the estimated junction temperature deviates from the measurement in average and cycling amplitude. While average value estimation improves for higher switching frequencies, the thermal cycling amplitude impairs. For this experiment,

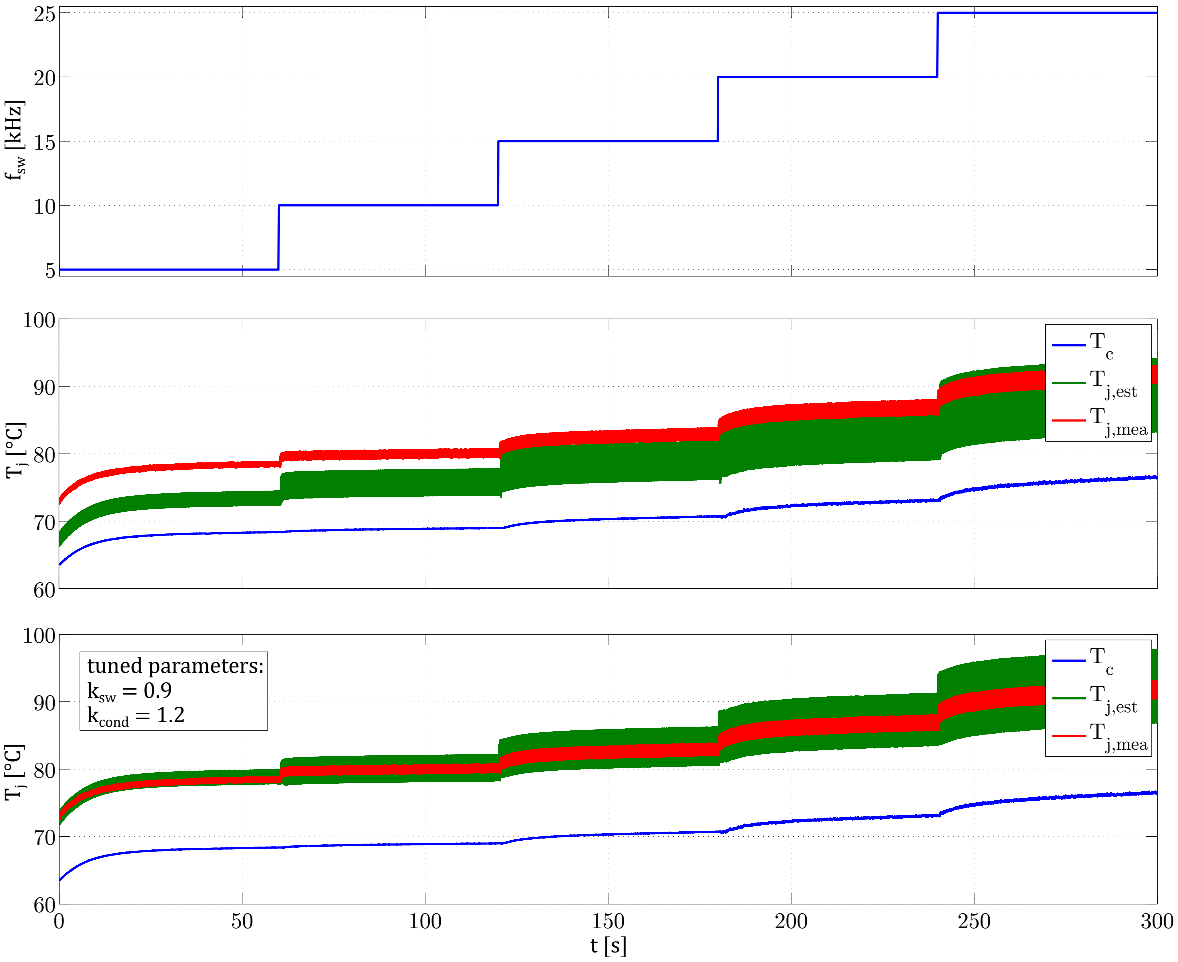

Figure 4.6: Comparison of junction temperature detection by electro-thermal model and measurement. Variation of the switching frequency. Output current is controlled to sinusoidal waveform with $\hat{i} = 10\,\mathrm{A}$, dc voltage $v_{dc} = 270\,\mathrm{V}$, fundamental frequency $f = 20\,\mathrm{Hz}$.

these dependencies are described by equations (4.3) and (4.4). However, these are generalized formulas which are not valid for every IGBT module. When changing the switching frequency, switching losses are the most important factor of influence in the electro-thermal model while the conduction losses can be considered constant. Thus, this experiment is suitable to define tuning parameters of the power losses model that adjust the total amount of switching losses and conduction losses.

$$P_{sw,tuned} = k_{sw} \cdot P_{sw} \tag{4.26}$$

$$P_{cond,tuned} = k_{cond} \cdot P_{cond} \tag{4.27}$$

Variation of k_{sw} adjusts the slope of the temperature estimation in Figure 4.6 and variation of k_{cond} adjusts the level. The experimentally detected tuning parameters for the given IGBT module are a constant gain for the switching losses $k_{sw} = 0.9$ and a constant gain for the conduction losses $k_{cond} = 1.2$. In the third row of Figure 4.6 the junction temperature estimation is repeated with the tuned parameters.

As steady-state of the junction temperature is reached for each selected switching frequency within the measurement, pictures have been taken with the infrared camera to validate the correct fitting of the optic fiber temperature probe. In figure 4.7, the photos for switching frequencies of 15 kHz and 25 kHz are shown. For both pictures, the four IGBT chips of the H-bridge can be seen clearly as the hottest spots. The bond wires can be recognized over the substrate due to their lower temperature. The substrate temperature is noticeable inhomogeneous, as the edges are about 10 K colder than the middle location. In addition, the temperature probe can be seen as the cold wire, leading from the top-right edge to the top left IGBT where it becomes the same temperature.

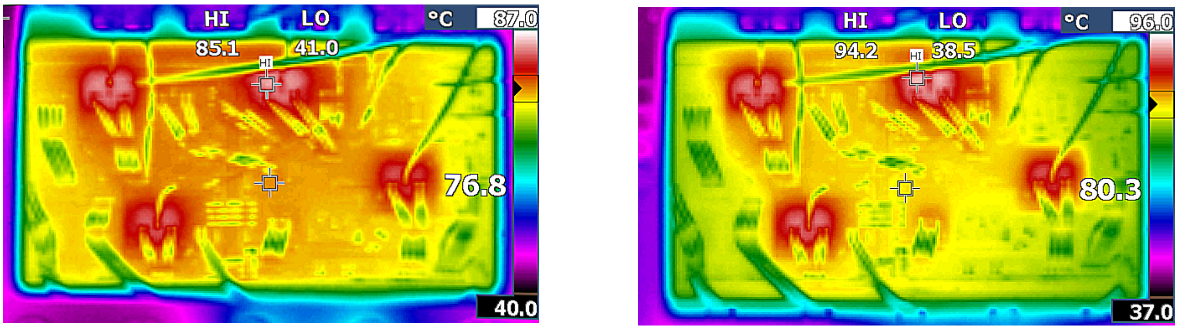

(a) (b)

Figure 4.7: Infrared camera photos of the IGBT module. (a) switching frequency of 15 kHz and (b) 25 kHz. Other parameters comply with figure 4.6.

Both, junction and case temperatures, fit to the steady-state values of matching switching frequency in Figure 4.6. The junction temperature is given by the hotspot measurement on the pictures top and the case temperature is given by the center measurement on the right side. Both infrared junction temperature measurements fit in the corresponding switching frequency which validates the correct placement of the temperature probe. The infrared measurements of the case temperature are about 5 K higher than those, determined by the module's NTC resistor. This is reasoned by the position of the NTC resistor, situated between the right IGBT and the top module border, and is therefore also a valid measurement.

In a second experiment, a variation of the fundamental frequency is done, while average output power and switching frequency are fixed. The fundamental frequency f is changed to values of 0.1 Hz, 1 Hz, 10 Hz, 50 Hz and 200 Hz in periods of 60 s to achieve steady-state in each test. The tuned parameters from the previous experiment are used. The results are shown in Fig. 4.8.

In figure 4.9 a close-up view of the previous figure is shown for the fundamental frequencies of 1 Hz, 10 Hz and 50 Hz. It can be seen, that waveform and synchronization

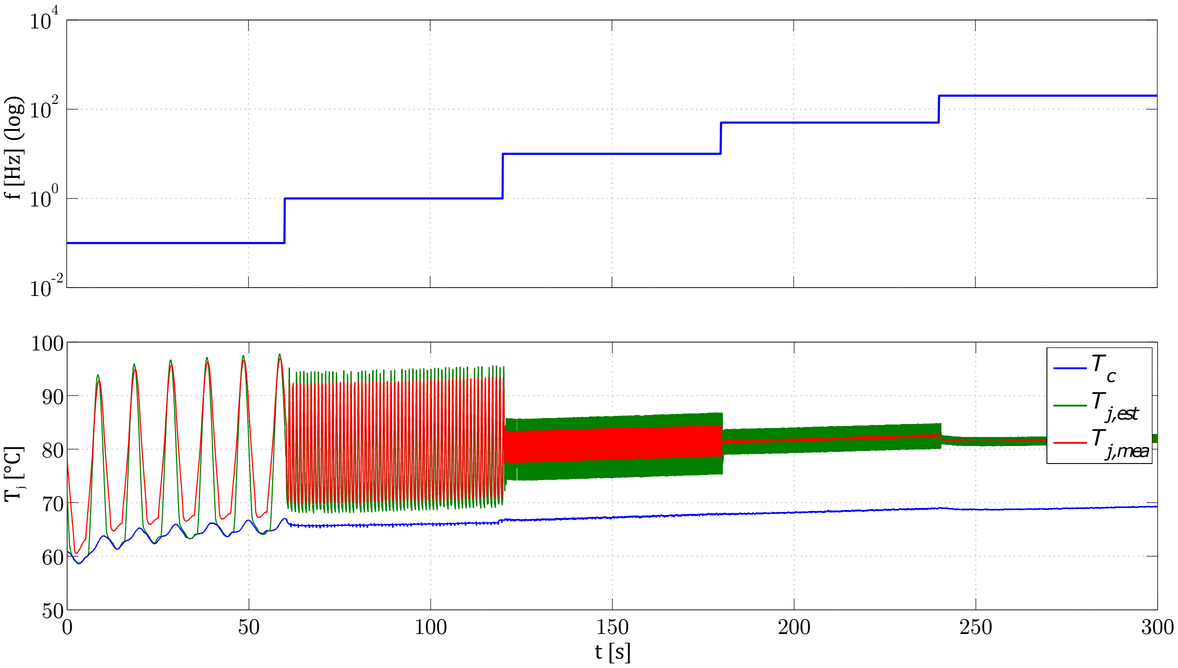

Figure 4.8: Comparison of junction temperature detection by electro-thermal model and measurement. Variation of the fundamental frequency. Output current is sinusoidal with $\hat{i} = 10\,\mathrm{A}$, dc voltage $v_{dc} = 270\,\mathrm{V}$, switching frequency $f_{sw} = 20\,\mathrm{kHz}$.

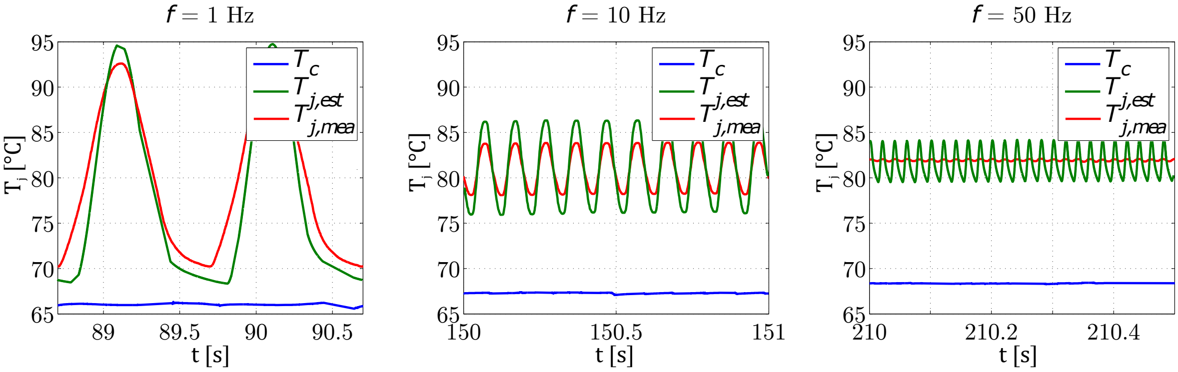

Figure 4.9: Variation of the fundamental frequency, close-up from figure 4.8 for selected time ranges.

of estimation and measurement match while the amplitude decreases for higher fundamental frequencies.

The average temperatures of estimation and measurement are in a good match for the tested fundamental frequency band. A deviation is in the thermal cycling amplitude which is rising with increasing fundamental frequencies. An explanation can be found in the used sensors of the measurement. The response time of the used temperature sensor limits the measurements for high frequencies. Therefore, for these frequencies neither validation nor disproof of the temperature estimation is achieved. However, a structural error in the power losses estimation is less likely as only the fundamental frequency is changed, which has minor influence on the losses.

4.3 Remaining lifetime model

A lifetime model is used to estimate the remaining lifetime of an IGBT module by modeling its increasing degradation. The aim is to assess over which time interval a module can be used reliably for a particular application.

The main failure mechanisms of power semiconductor modules are induced by plastic strain of inside interconnections caused by temperature cycling. The most vulnerable interconnections are the bond wire fixation and the chip solder [63]. In the 1990s a study to quantify the effect of power cycling on the modules using accelerated lifetime tests called LESIT (Leistungs Elektronik Systemtechnik Informations Technologie) was conducted [63]. In this study accelerated lifetime tests were conducted in which the component is stressed with controlled dosage until its end-of-life. In order to relate the failure mechanisms and quantified reliability performance, several models have been proposed. These are based on the Coffin-Manson model that describes the occurrence of plastic deformation due to a periodic process, firstly presented in the 1950s [109]. The Coffin-Manson-Arrhenius model considers temperature cycling and average temperature based on the LESIT results. Its analytical equation is:

$$N_f = a \cdot \Delta T_j^{-n} \tag{4.28}$$

The number of cycles to failure N_f is described in dependency of the amplitude of a thermal cycle ΔT_j and the constant coefficients a and n which are extracted from the LESIT data set [110]. The Coffin-Manson-Arrhenius model shows the main dependency on the junction temperature amplitude, but it has been proven that module lifetime is also considerable dependent on other parameters which describe the underlying conditions of the module operation in more detail [111].

The Norris-Landzberg Model additionally takes into account the cycling frequency of the junction temperature [112]. The Bayerer model [113] also includes more specific parameters on the operating conditions. Its analytical equation is:

$$N_f = A \cdot \Delta T_j^{\beta_1} \cdot exp\left(\frac{\beta_2}{T_{j,min}}\right) \cdot t_{on}^{\beta_3} \cdot i_B^{\beta_4} \cdot V_C^{\beta_5} \cdot d_b^{\beta_6} \tag{4.29}$$

In the Bayerer model the number of cycles to failure N_f is described in dependency of the amplitude of thermal cycles ΔT_j and the average temperature $T_{j,avg}$. Other coefficients consider the pulse duration t_{on}, the current per bond foot i_B, the voltage class V_C, the bond wire diameter d_b and a technology factor A. The equation can be derived for a specific IGBT module and operating conditions using the coefficients and values given in Table 4.2. The coefficients β_{1-6} are extracted from the LESIT data set of multiple reliability experiments. The values are adjusted for best match of a three-phase inverter IGBT module ($i_{max} = 25\,\mathrm{A}$, $v_{dc,max} = 1200\,\mathrm{V}$) that is used for the experimental validation using data provided in datasheets and application manuals.

Parameter	**Symbol**	**Value**	**Coefficient**
Technology Factor	A	$2.03 \cdot 10^{14}$	n.a.
Temperature difference	ΔT	variable	$\beta_1 = -4.416$
Min. chip temperature	$T_{j,min}$	variable	$\beta_2 = 1285$
Pulse duration	t_{on}	variable	$\beta_3 = -0.463$
Current per bond foot	i_B	$i_C/4$ bonds	$\beta_4 = -0.716$
Voltage class /100	V_C	$12\,\mathrm{V}$	$\beta_5 = -0.761$
Bond wire diameter	d_b	$300\,\mu\mathrm{m}$	$\beta_6 = -0.5$

Table 4.2: Parameters for Bayerer model

The cycles to failure chart of the Bayerer model is illustrated in Figure 4.10. In the chart the strong dependency between the number of cycles to failure and amplitude of thermal cycles is displayed for different temperature levels.

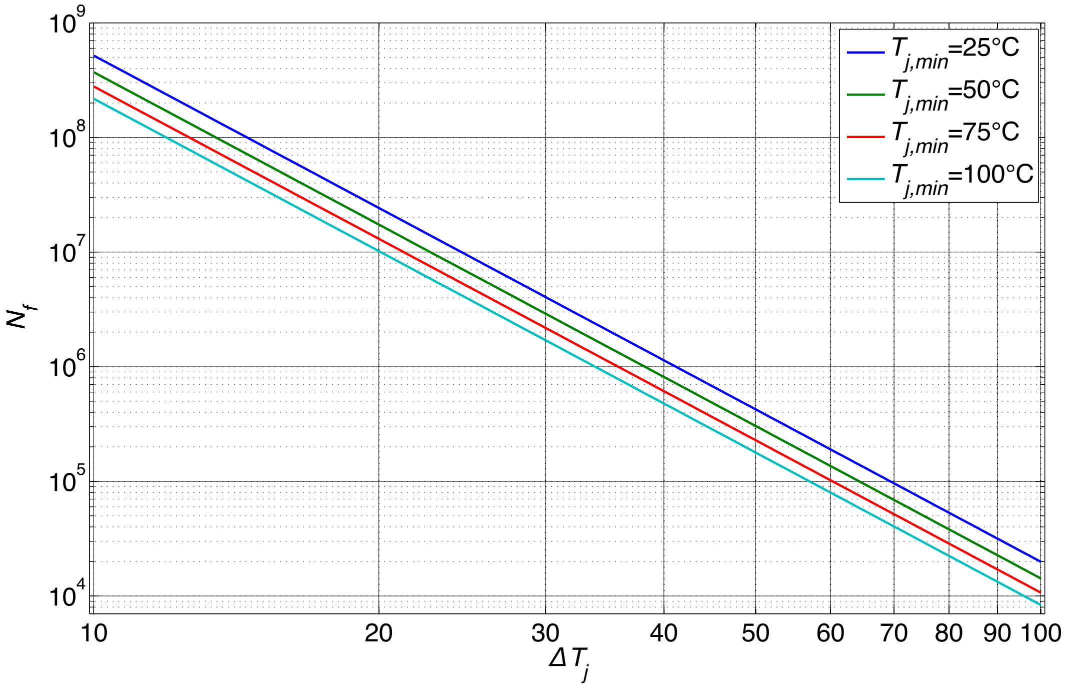

Figure 4.10: Cycles to failure of the Bayerer lifetime model for IGBT module using parameters of Table 4.2 and a fixed pulse duration of 30 s.

To achieve a quantity of the damage taken by a specific thermal cycle the reciprocal of N_f is applied. If almost no junction temperature cycling takes place or noise occurs in the estimation N_f^{-1} is close to zero. For larger thermal cycles the damage rises according to the exponential influence of ΔT_j. The weighting of harmful temperature cycles makes N_f^{-1} a good choice as an input to the active thermal controller.

To consider multiple thermal cycles with multiple properties as they occur in most applications, Miner's cumulative damage rule is applied [66]. Miner's rule can be written as:

$$C = \sum_i \frac{n_i}{N_{f,i}} \tag{4.30}$$

Here C is the cumulative damage, n_i the number of cycles and $N_{f,i}$ the durability of the i-th stress range. Thus, the cumulative damage will rise the more thermal cycles occur in the mission profiles. If the cumulative damage reaches 1, the module will fail according to the lifetime model [114]. If every thermal cycle amplitude occurs only once in the profile the number of cycles is set to $n_i = 1,\ \forall i$.

If it is necessary to perform an end of life (EOL) test by experiment, high magnitude thermal cycles must be used to obtain results within a reasonable amount of time. If a period of 30 seconds is assumed for a thermal cycle, an unaccelerated test would take about ten years to fulfill 10^7 cycles, which may not even be enough to reach EOL for the module depending on test parameters. Therefore a time acceleration factor f_a is introduced, to carry out a test in less time but higher stress having the same impact to the modules lifetime [65]. All thermal cycles in a temperature profile ΔT_{op} are converted to a corresponding amount of thermal cycles with an appropriate amplitude for the experiment ΔT_{test} The Coffin-Manson acceleration factor definition is [96]:

$$\left(\frac{\Delta T_{test}}{\Delta T_{op}}\right)^c \tag{4.31}$$

In c the fatigue ductility is expressed. Other models for acceleration factors exist, regarding more parameters to the investigated failure mechanism [96]. Instead of using a model-based approach, another possibility to detect the aging of a module during operation is the measurement of a physical parameter such as the collector-emitter voltage v_{CE}. An increment of v_{CE} is observed for bond wire lift-off [78]. However, v_{CE} is also sensitive to the applied power level and changes in the temperature. A method to detect degradation of the solder joints is given in [102]. The stressed material joints lose their capabilities in heat transfer leading to non-uniformities in the heat distribution in the module. These can be detected by measurements at multiple positions on the substrate.

4.4 Condition Monitoring

The concept of Condition Monitoring (CM) is to assess the current health status of a system component and detect incipient faults in order to take corrective actions before failures occur [62]. This allows performing maintenance according to the system's needs instead of sticking to fixed intervals. Starting from a known system's condition, the CM allows predicting the onset of failures due to wear-out. The CM notifies the system controller when a critical state is diagnosed the device can be addressed for planned maintenance. Detection of failure precursors is a method to predict malfunctions before they occur [59].

4.4.1 Model-based Condition Monitoring

The CM can be applied to obtain the health status of power semiconductor modules. A concept based on the lifetime model presented in the previous section is shown in Fig. 4.11. It considers the stressors temperature swing and average temperature. The thermal swing can be extracted from the mission profile using the rainflow counting algorithm [115]. The main advantage is the sheer software implementation, which can operate without additional hardware.

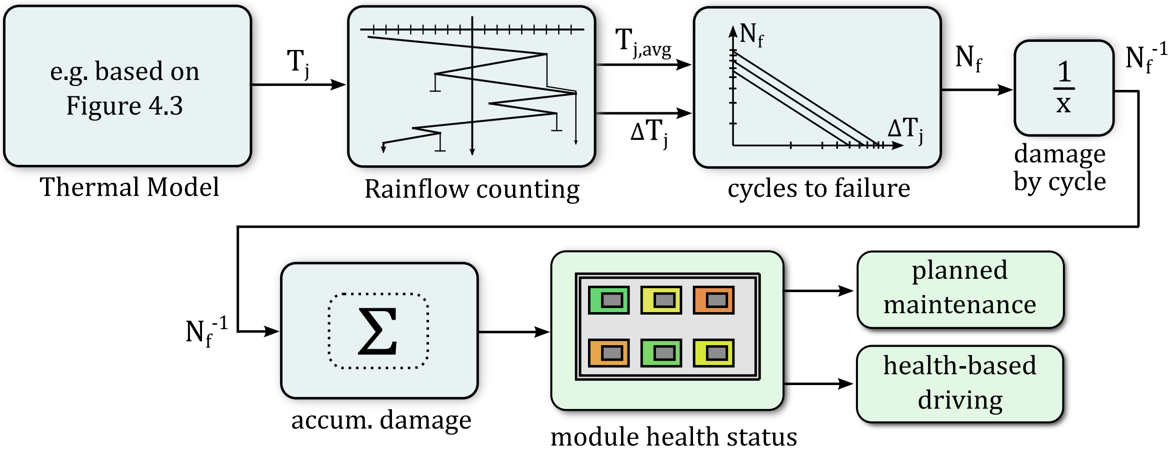

Figure 4.11: Block scheme of model-based condition monitoring applied to a power semiconductor module.

The accumulated damage is derived with Miner's rule and represents the current health status of the semiconductor.

4.4.2 Sensor-driven Condition Monitoring

Instead of a model-based estimation, the system's health status can be obtained by measurement of suitable parameters. The aging model shown in the previous paragraph is not essential for this approach. However, additional sensors and software evaluation is necessary.

Sensor-driven condition monitoring has been applied for detection of bond-wire lift off in power semiconductor modules. In [116] external dc currents are injected into the power unit to detect loosened bond wires. Another possibility is to use an electronic speckle pattern interferometry to measure optical displacement or strain of wire-bonds during operation [117]. The need for additional sensors is an additional invasiveness to the system.

One way to predict a bond wire failure is to look at the saturation voltage of the IGBT $V_{CE,sat}$ at low current levels. An increase of $V_{CE,sat}$ by 5% is a criterion to indicate an error of the bonding wires. An increase of $V_{CE,sat}$ by 15% indicates that the IGBT is seriously degraded. The monitoring of the bonding wires can be realized by measuring the on-state voltage across the IGBT and current trough the device. For a specific device current, the measured on-state voltage across the IGBT is compared against a value stored in a look-up table. In the lookup table, the reference values of the voltage of the IGBT in the switched-on state are stored as a function of the current and the temperature. An additional scaling factor allows calibration [95].

Another possibility is the use of the short-circuit current of the IGBT module for detecting the material fatigue of the bonding wires. In the process, the short-circuit current becomes smaller with increased material fatigue because of the increased line resistance for a constant gate voltage V_{GE}. As a criterion for determining the end of life, a reduction of the short-circuit current by 4% can is used [118].

The fatigue of the solder causes the thermal resistance R_{th} of the considered transitions to increase. The criterion for defining the end-of-life is an increase of R_{th} by 20%. In order to determine the thermal resistances, both the junction temperature and the case temperature Tc must be detected and stored periodically. Furthermore, the current through the IGBT must has to be measured and stored periodically. The thermal resistance between junction and case can then be determined [95].

4.4.3 Health-based driving

The health information given by the condition monitoring can be used for health-based driving of the monitored components. This is illustrated in the left of Fig. 4.11 for a power electronics IGBT module. When the first chip on the module fails, the system has to be shut down and the whole module must be replaced. The controller of the health-based driving can release the stress from the most damaged chips in the module. Consequently, the time to failure can be increased and the module durability is consumed more efficient.

To realize the health-based driving, the controller must be capable to influence the stress on specific semiconductors in the module. A possibility is to use direct control schemes like the Finite Control Set Model Predictive Control (FCS-MPC) as it is capable to control the conducting of each switch on a module individually. This approach is addressed in chapter 5..

4.5 Active thermal control

Junction temperature control uses temperature related control parameters to influence the junction temperatures in power semiconductor modules online. The goal is to reduce the thermal stress in the module by smoothing the temperature variation in order to prevent damages caused by thermal cycling. To influence the junction temperatures, the thermal control increases or decreases the temperatures in the chips temporary.

The main approach of present junction temperature control is to alternate the power losses in the semiconductors while maintaining the application's mission profile. By applying additional losses in the module, the temperature can be raised temporary or vice versa reducing the losses decreases the temperature temporary. As the temperature is controlled active during operation, this method is called active thermal control (ATC) [2]. The thermal stress is relieved in the module and the aging can be reduced.

In the following subsections, the origin and scale of thermal cycles in selected applications for power modules are pointed out. Afterwards a classification of active thermal control methods is given. An active thermal control algorithm capable to reduce the thermal cycles and therefore increases lifetime and reliability of the module is presented. In the end, the algorithm is validated experimentally.

4.5.1 Occurrence of thermal cycles

Thermal cycles in power electronic modules can generally be caused by the switching of the inverter itself, by the mission profile of the application and by environmental conditions. They distinguish in period, amplitude and quantity, therefore they also distinguish in their importance towards module lifetime. In figure 4.12 the general structure of thermal cycles is shown and their notations are introduced.

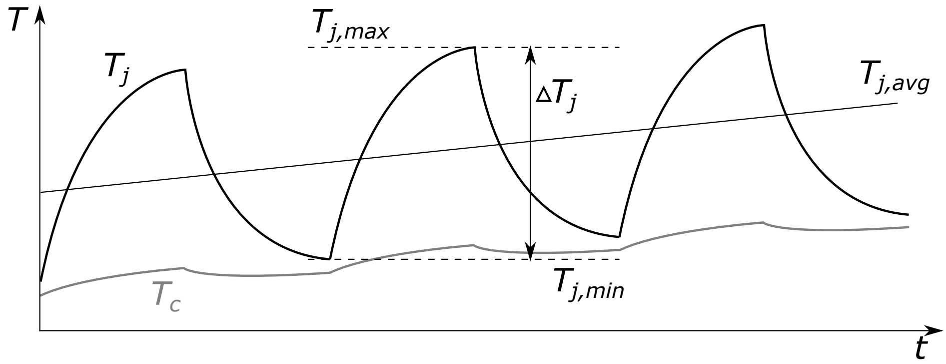

Figure 4.12: Notations for thermal cycles. The amplitude of a thermal cycle ΔT_j is the difference between the temperature maximum $T_{j,max}$ and minimum $T_{j,min}$ of a cycle. $T_{j,avg}$ is its average.

Thermal cycles occur with varying periods. When going from short-term to long-term cycles, the first to investigate are thermal cycles in the duration of the switching period.

During a switching period a semiconductor is either in on-state, off-state or within a switching-state. In on-state it is conducting, thus conduction power losses occur and the junction temperature is heating up. In equal measure it is heating up during switching-states as switching power losses arise, whereas during off-state only negligible reverse losses occur and the junction temperature is cooling down again. However, as the switching frequency is usually in the range of several kHz the amplitude of the temperature changes are minor due to the very short-term alternation between heating and cooling stages. Thermal cycles with an amplitude less than 3 K do not effect the module's lifetime as the material strain is still elastic in this order [119]. Conversely there is no need to reduce these very short-term cycles.

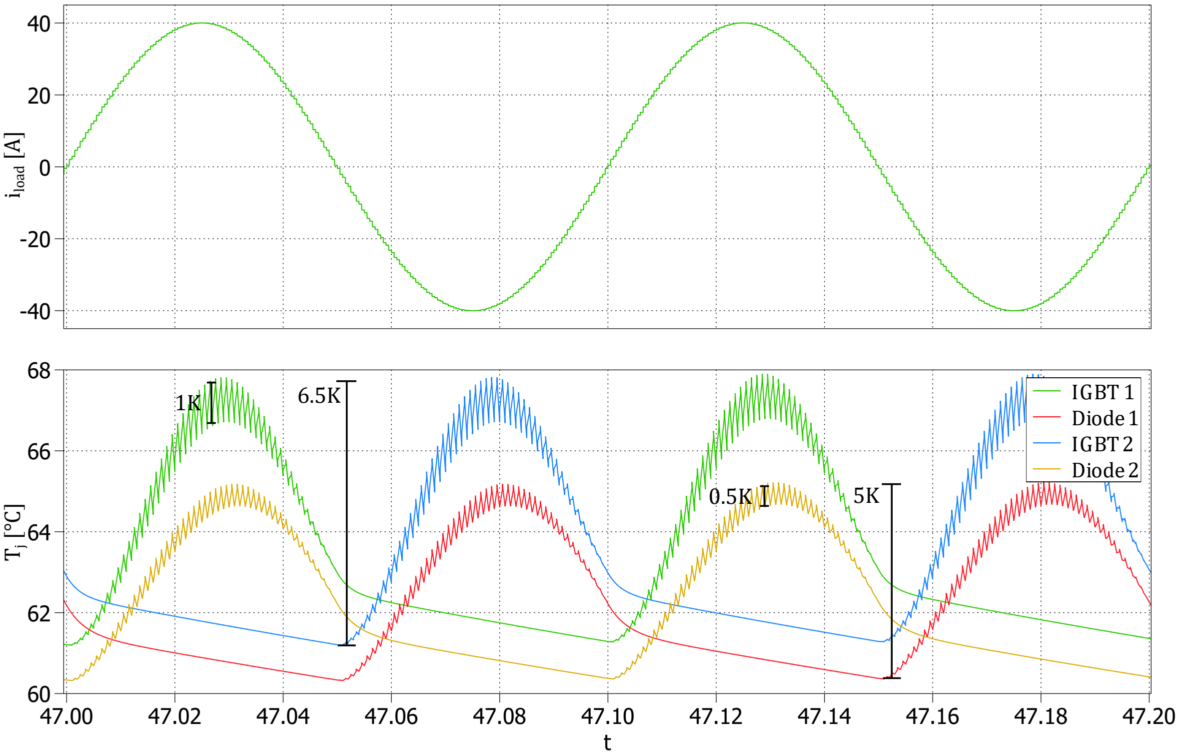

Figure 4.13: Simulation of the thermal cycling in the scale of the switching frequency $f_{sw} = 5\,\mathrm{kHz}$ and fundamental frequency $f = 10\,\mathrm{Hz}$.

Next, short-term thermal cycles in the duration of the fundamental frequency occur for sinusoidal AC currents or other periodic waveforms, as conduction losses increase for high currents and vanish during zero crossings. The frequency is usually in the range of several Hz. Therefore, the junction temperature also cycles with this period. Its amplitude is depending on the thermal parameters and the operating point and can easily exceed 3 K. Therefore, they can influence the module's lifetime. The thermal cycles in the bandwidth of the switching frequency and the fundamental frequency are shown in comparison for IGBTs and diodes in figure 4.13. The output current is sinusoidal with $i = 25\,\mathrm{A}$, $v_{dc} = 800\,\mathrm{V}$.

Especially for inverters that feed variable speed drives, operating points containing high currents at low frequency occur, for example during acceleration of an electric vehicle. This can lead to considerably larger thermal cycles as both the heating and cooling periods increase. Therefore, the thermal cycling amplitude increases for lower fundamental frequencies because of the larger heating up and cooling down times. A more general view on the dependency between output frequency and thermal cycling amplitude is shown in figure 4.14. This means that mission profiles that include low fundamental frequencies can cause significant thermal cycling amplitudes even if the peak value of the power in the mission profile is constant.

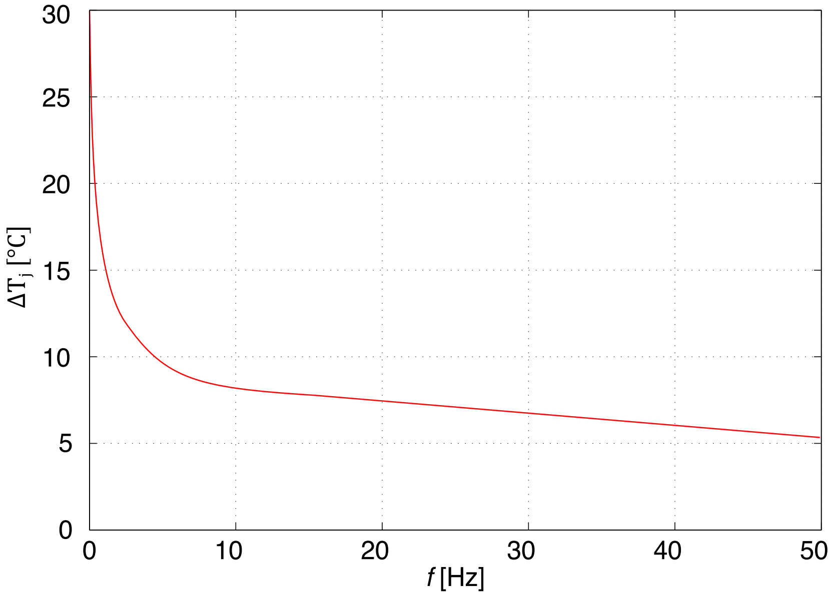

Figure 4.14: Junction temperature cycling amplitude as a function of the fundamental frequency.

In the mission profile also long-term thermal cycles may occur. As the junction temperatures depends on the power flow in the inverter, the power profile of the application is a critical parameter. In Figure 4.15 the occurring cycles of an alternating mission profile with a period of 10 s are shown in comparison with the fundamental frequency. This is the same simulation as Figure 4.13 but in a larger time scale.

Depending on the application of a power module various short-term and long-term thermal cycles may occur. These can appear almost unpredictable and not periodic like i.e. the mission profile of an electric vehicle, a photovoltaic inverter or a wind turbine converter. Others like some motor drive inverters for industrial processes or city railway drives may have periodic or particularly predictable mission profiles.

Eventually, for outdoor applications environmental conditions affect the modules directly. That means in case of a not only the electric load but also the ambient temperature and therefore the module temperature itself changes dependent on daily or yearly cycles. However, these cycles occur rarely in comparison with the cycles to failure of a module and thus are less relevant.

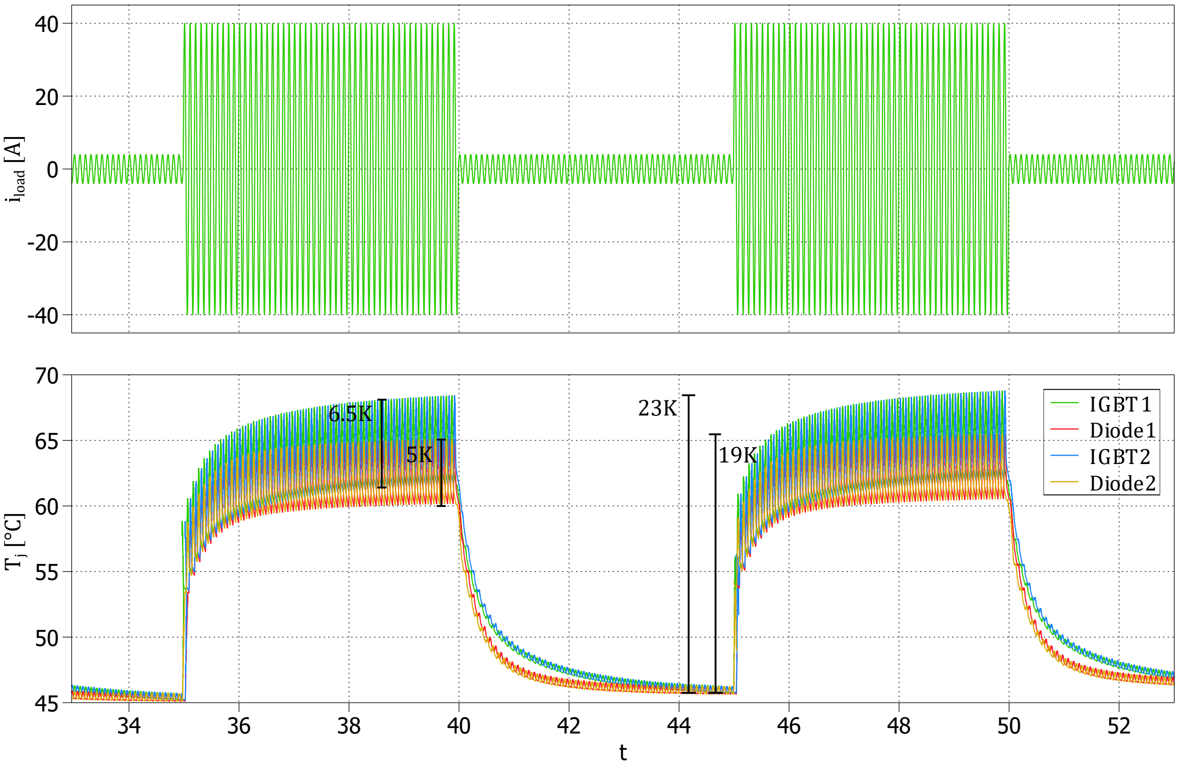

Figure 4.15: Simulation of thermal cycling for an alternating mission profile.

4.5.2 Classification of ATC

A precursor of thermal control is to optimize the mission profile for a better thermal behavior of the hardware components. However, no active reduction of the thermal stress happens here.

The active thermal control can be classified by the hierarchic level of interaction with the power electronic system. This is done in Figure 4.16. The levels reach from system control down to the gate driver. On the layer of the current control a variation of the current limit [108], circulating current among parallel connected converters [120], circulating reactive power [121] and the dc link voltage [122] have been applied to control the junction temperature. On the layer of the modulator a selection of the switching frequency [2] and the modulation method [123] have been applied. On hardware layer the gate voltage has been adjusted [124], [125]. As an example, a short-term temperature drop can be prevented or reduced when losses are increased temporary by increasing the switching frequency.

The ATC can be performed without knowledge of the junction temperature, but using estimation of the power losses. An electro-thermal model as given in section 4.2 can be used to achieve online estimations of the junction temperatures on the basis of electrical measurements to enable more precise control of the thermal stress [108].

Although ATC is a recently introduced concept to regulate power losses and control thermal stresses, several approaches have been proposed in literature. In the following,

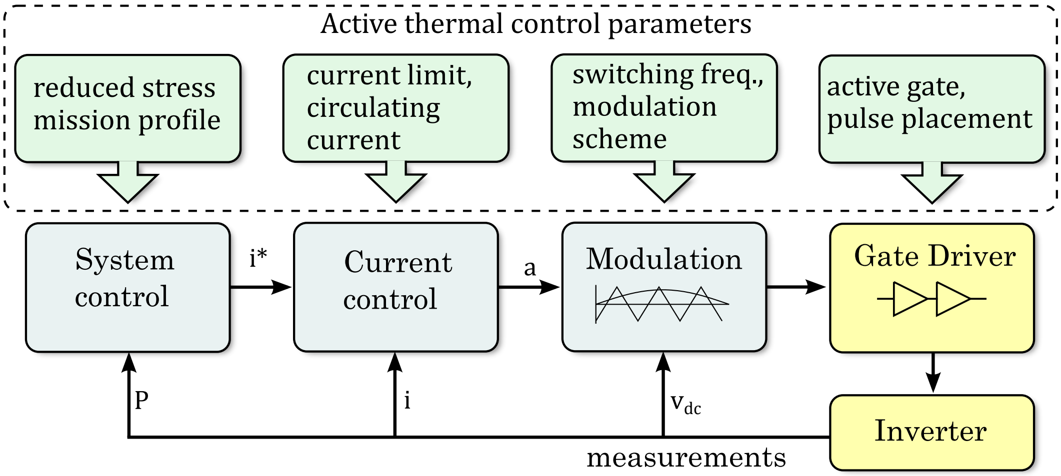

Figure 4.16: Classification of parameters for Active thermal control by point of interaction with the power electronics control system.

the previously introduced categories of ATC are described in more detail and state of the arts examples are given. It is notable that there exists no systematic and complete study even of one of these possible control approaches highlighting in deep the possibilities and limitations.

4.5.2.1 System Control

The reactive power delivered by a converter is a system control reference that is normally not fully utilized. It is not restricted to the available mechanical and electrical power of the converter system. However, it can significantly influence the loading of components and thereby is a very suitable candidate to achieve active thermal control.

In [121] a 3L-NPC converter is operated under maximum over-excited as well as under-excited reactive power, respectively, with rated active power output. The loss distribution of the same 3L-NPC converter is influenced by introducing different reactive power. The reactive power not only modifies the phase angle between the output voltage and current of converter, but also modifies the current amplitude flowing in the power devices. As these parameters are related to the power loss and thermal loading of power devices, the approach can be utilized for ATC.

In modular multilevel converters (MMC) the modules are stressed unequally leading to higher thermal stress in particular modules. An algorithm is proposed in [126] for active balancing the junction temperatures of the MMC cells.

4.5.2.2 Converter Control

The converter's control generates the reference for the lower-level systems that implement the modulation, meaning that at this level the active thermal control can be used to modify the control variables. The goal can be either the junction temperature limitation, in order to perform an active de-rating that pushes the semiconductors close to their limits with a minimum over-design or the thermal cycle reduction.

Junction temperature limitation usually involves the saturation of a control variable such as the dc voltage, the duty cycle or the load current when the temperature reaches a certain level. A dynamic limit of the inverter current under thermal constraints is proposed in [2]. This enables low-power operation of nearly overheated systems to prevent further gain in temperature complete shutdown or damage of the module due to over temperature. Another possibility is to reduce the maximum temperature derivative, which at the same time reduces the thermal cycle. This concept was explored in [127], where the duty cycle of a dcdc converter for a photovoltaic system is actively modified in order to limit the maximum junction temperature derivative in presence of irradiation changes.

An approach for thermal cycle reduction is to adjust the switching frequency as it has a direct influence on the power losses without notable affecting the operating point of the application when adjusted within system constraints. The switching frequency control is done using linear control [2] or hysteresis control [123], [108]. The reduction of fast thermal cycles is achieved by increasing or decreasing the switching losses when the output power drops or increases. As the used active thermal controllers decrease the switching frequency below that of the uncontrolled system at the price of an increase of the current ripple. In a comparison done in [108] the active thermal controller is reducing the current and is therefore influencing the mission profile. Another limitation of these approaches is that a selective temperature control of specific semiconductors in the module is not possible. Therefore, when the active thermal controller changes the switching frequency, temperature changes occur even in those semiconductors that were not critically affected by thermal cycling.

Another approach is to manipulate the loss distribution between IGBTs and diodes, by adjustment of the dc link voltage which influences the modulation index [128]. This can be used to relieve specific semiconductors on the cost of additional losses in the inverter caused by a higher current magnitude.

4.5.2.3 Modulation method

Reducing the switching loss by using discontinuous PWM (DPWM) in two-level three-phase converter is a well-known strategy for the device loading control [129]. The principle of discontinuous PWM is to clamp the voltage reference of the converter output to the upper or lower dc-link potential in a certain interval so that the corresponding power device will keep its status without switching, and the switching loss is thereby mitigated in that interval. Since the total loss of the power device during this clamping period is reduced, the mean value and variation of the junction temperature are therefore both relieved [123].

In [130] modulation methods for the three-phase neutral-point-clamped inverter are developed with the aim to redistribute the losses among the power devices and balance the thermal stress.

4.5.2.4 Gate driver

Active gate control is a possibility to control the semiconductor losses, without affecting the functionality of the device. As the gate drive voltage influences both conduction and switching losses of semiconductors, it can be used to decrease thermal cycling [125]. In literature an active gate driver has been reported that is applied for counteracting variations in the on-state resistance of IGBTs [131]. Another active gate control has been used to balance the currents among parallel connected IGBT devices [132]. By adjusting the control parameters in these active gate controls, they can also be applied to reduce the thermal cycling in the semiconductors.

Active gate control in the context of gallium nitride (GaN) power semiconductors is from particular interest. Compared to Si-devices GaN-devices provide in particular a higher switching speed and higher operating temperature. As a consequence, they have an increased power density which makes the temperature management critical especially for the PCB and components to which the GaN is connected. Therefore, active gate control has been applied in [124] to reduce the thermal cycling in a GaN-based dcdc converter. The variation of energy loss during turn of of the devive is depends on the tunable parameters of the active gate driver.

4.5.3 ATC by variation of the switching frequency

In this subsection an active thermal control is presented that reduces the thermal stress without interfering the system operation such as preventing switching operations which adds current ripple or limiting the maximal power. Using the proposed ATC, the applications operation points stay untouched, as only temporary increments of the switching frequency are performed.

In Figure 4.17 this approach is demonstrated. On the right-hand side of this figure the physical system is shown, in this case an H-bridge inverter module. It provides the necessary measurements for the converter control, e.g. the load current i_{load} and the dc link voltage v_{dc}. In addition the IGBT module's case temperature T_c is measured using a low-bandwidth sensor on its substrate.

The duty cycle a is generated by a general closed-loop converter current control, which can be a proportional-integral (PI) controller as presented in [32]. Its input i_c^* is the current reference and i_{meas} is the measurement feedback. The required gate signals are created in a pulse width modulator (PWM), using a and the switching frequency f_{sw}.

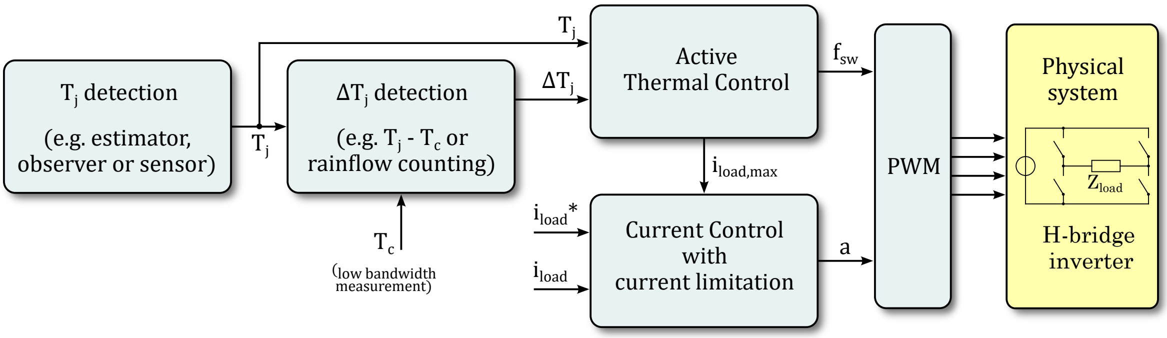

Figure 4.17: Control structure of an active thermal control system.

This system is extended by the ATC, which selects the switching frequency f_{sw} in order to control the junction temperature cycling in the module. This can relieve the thermal stress from the module. In addition it can limit the maximum load current in an event of overtemperature. This allows to continue the inverter operation with reduced power instead of a complete shutdown of the system.

The junction temperature estimations are provided by any kind of temperature detection, e.g. an electro-thermal model as demonstrated in section 4.2. There are several possibilities to determine the thermal cycle amplitude ΔT_j.

From the analytic point of view it is defined as the difference of the maximum temperature $T_{j,max}$ and the minimum temperature $T_{j,min}$ of a given thermal cycle, as shown in figure 4.12:

$$\Delta T_j = T_{j,max} - T_{j,min} \tag{4.32}$$

However, for this procedure it needs to be detected, at which time a maximum and a minimum is reached. The rainflow algorithm is a common solution to detect full and half cycles of the irregular mission profile. In its original form it cannot be applied online, which makes it impractical for ATC. However, an adaption for the online usage has been presented in [115]. The method processes each minimum or maximum when it occurs and thus it does not require any knowledge of the time history of the mission profile.

Another possibility is to detect the momentary thermal cycling amplitude. It is the difference between the junction temperature T_j from the case temperature of the module T_c.

$$\Delta T_j = T_c - T_j \tag{4.33}$$

If no power losses occur, the junction temperature will decrease to the value of the case temperature. When short term power losses occur, the junction temperature will rise very fast compared to the case temperature due to its small thermal capacitance. The thermal resistance ensures a temperature difference between the layers at all times. For short-term cycles this method can be used to detect ΔT_j. An advantage of this method is that computation time is saved compared to the rainflow counting.

A hysteresis controller is used to react on the detected thermal cycle amplitude. The switching frequency is changed according to the amplitude of thermal cycles between three given frequencies. The higher this amplitude is, the more losses have to be added in order to compensate the thermal cycle, so a higher switching frequency is selected. When the cycle ends its amplitude vanishes and the switching frequency is reset to its normal value. To prevent the controller from fast toggling between two output values on the input threshold, a sufficient hysteresis is used. Figure 4.18 shows the proposed hysteresis diagram.

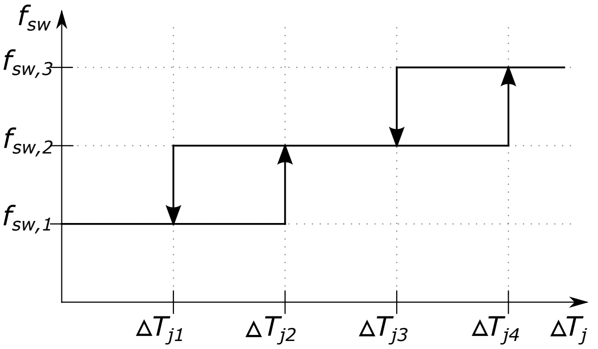

Figure 4.18: Hysteresis controller diagram.

4.5.4 Parametrization of the ATC

The hysteresis points ΔT_{j1} to ΔT_{j4} shown in the figure have to be set reasonable for an effective operation of the hysteresis controller. Positive values of ΔT_j are compensated by an incremental of the power losses and, respectively, negative values by a reduction of power losses if this is provided. However, a reduction of the switching frequency is not investigated here as this may lead to additional harmonic content in the controlled current and therefore worsen the system operation. Consequently, only positive hysteresis points are set.

For best results, the maximal amplitude of thermal cycles $\Delta T_{j,max}$ has to be identified. This can either be done by a step-response experiment or can be achieved adaptive during normal operation by doing an online maximum search and storing the maximum value within a given sufficiently large time period. Next the hysteresis points are distributed inside the interval $[0 \, .. \, \Delta T_{j,max}]$. A definition that proved good results in practice is given as follows:

$$\Delta T_{j1} = 0.15 \cdot \Delta T_{j,max} \tag{4.34}$$

$$\Delta T_{j2} = 0.25 \cdot \Delta T_{j,max} \tag{4.35}$$

$$\Delta T_{j3} = 0.4 \cdot \Delta T_{j,max} \tag{4.36}$$

$$\Delta T_{j4} = 0.5 \cdot \Delta T_{j,max} \tag{4.37}$$

To demonstrate the effectiveness of the thermal control algorithm, simulation is done using MATLAB, Simulink and PLECS Blockset. The simulation parameters are set so that they are fitting to a 1200 V, 25 A IGBT module that is also used in the thermal model validation. The passive load is set to $R_{load} = 10\,\Omega$ and $L_{load} = 8\,\mathrm{mH}$. The trapezoidal mission profile of a grid connected photovoltaic inverter compliant with norm EN50530 is used for the simulation.

For comparison the mission profile is run with and without the use of the active thermal control. The reference is given in Figure 4.19. The switching frequency is kept constant at 10 kHz. The thermal cycling due to the mission profile is about 20 K for the IGBTs and about 7 K for the diodes. In this simulation the load over a fundamental period is equal for the IGBTs and diodes in the module, respectively.

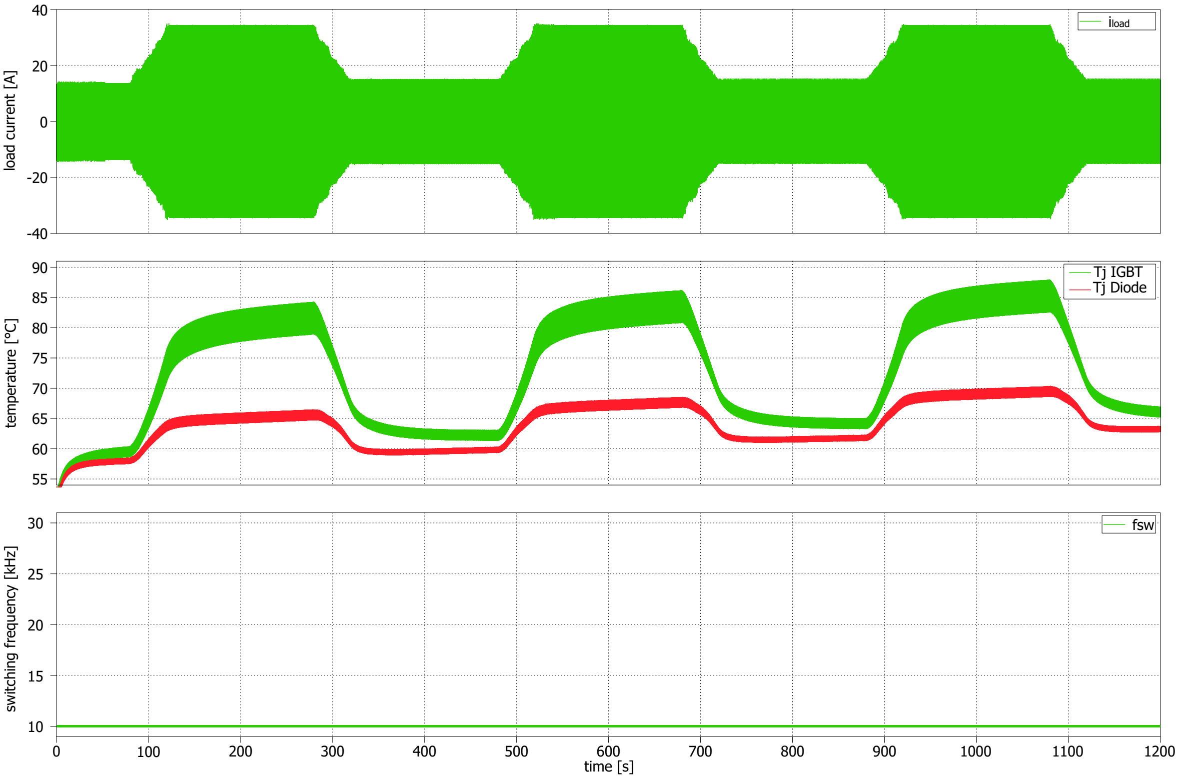

Figure 4.19: Simulation of a trapezoidal mission profile of a photovoltaic inverter. Active thermal control is not applied.

In Figure 4.20 the active thermal control is applied for the same mission profile. The active thermal control counteracts the cooling down in the low power stages by increasing the switching losses temporary. The nominal switching frequency of 10 kHz can be increased by the controller in two steps to 20 kHz and 30 kHz. Consequently, the thermal cycling of the IGBTs is reduced the about the same level as the thermal cycling caused by the fundamental frequency. For the diodes, the thermal cycling can nearly be prevented.

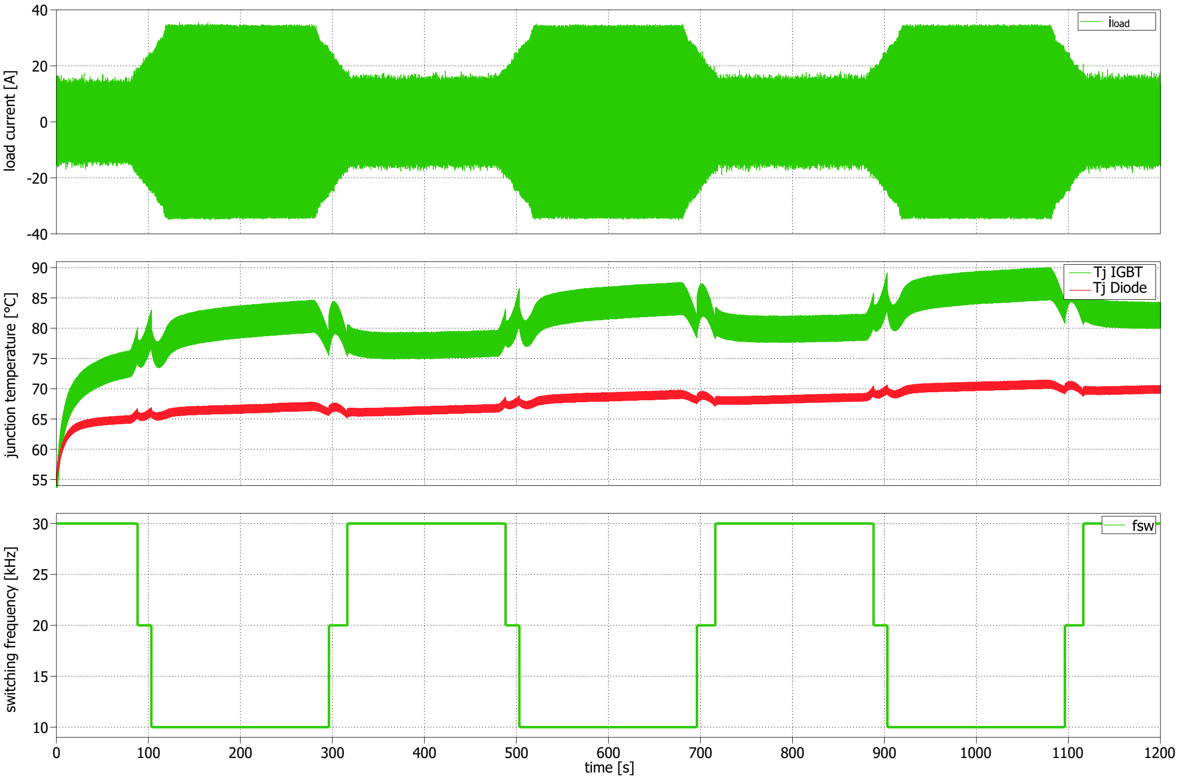

Figure 4.20: Simulation of a trapezoidal mission profile of a photovoltaic inverter. Active thermal control is applied.

As a side-effect on the partially increased losses, the average junction temperatures of both, IGBT and diode, are increased slightly. This does affect the losses and also the lifetime the average temperature is a parameter of the given lifetime models. However, the negative impact on the lifetime of the average temperature increment is minor in comparison to beneficial impact on the lifetime due to the reduction of thermal cycles.

4.5.5 Experimental validation of the ATC

Detailed experimental validation using a high-bandwidth temperature measurement is done for a crane application, an electric vehicle and an industrial process. On basis of the experimental data and the lifetime model given in section 4.3 an estimation on the extension of the modules lifetime using the thermal control is done.

4.5.5.1 Crane application

A mission profile of a 10 minutes crane application which is changing between holding and lifting is used. A similar profile appears for conveyor bands and elevators with changing loads. Temperatures are measured with and without the use of active thermal control. The output current is controlled to fit $\hat{i} = 10\,\mathrm{A}$ times the mission profile. The fundamental frequency is fixed to $f = 50\,\mathrm{Hz}$, the dc voltage is $v_{dc} = 400\,\mathrm{V}$. The results are shown in Figure 4.21.

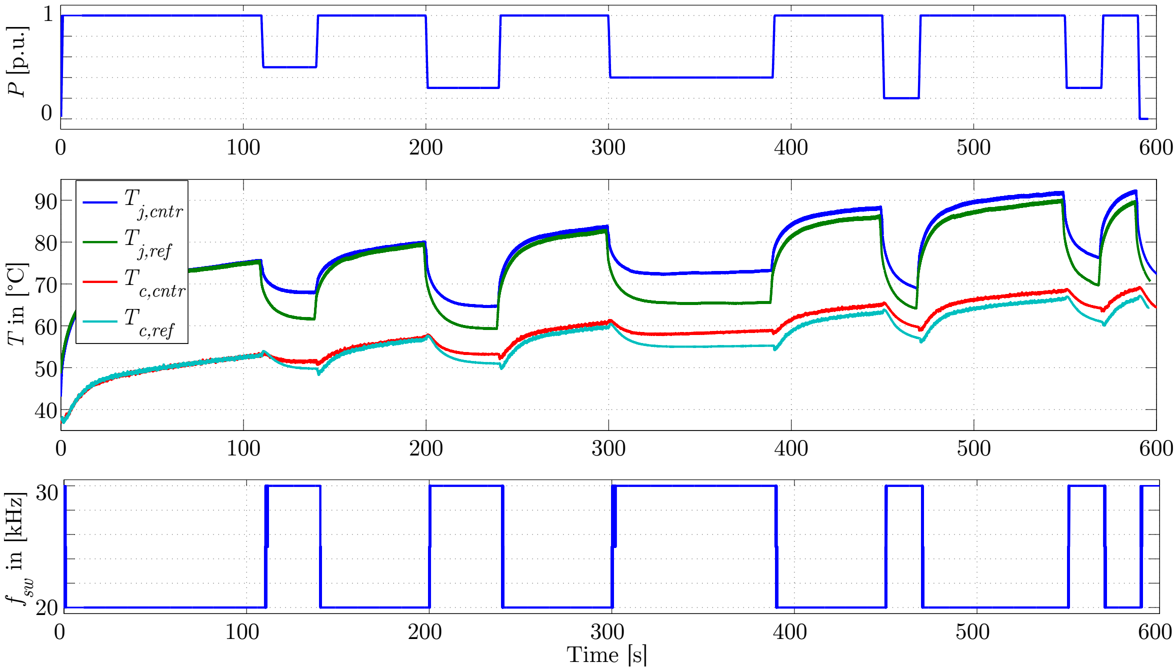

Figure 4.21: Measured junction and case temperatures with and without the use of active thermal control for crane application.

	$i = 1$	$i = 2$	$i = 3$	$i = 4$	$i = 5$
$\Delta T_{j,ref,i}$	13.7 K	20.8 K	18.6 K	21.3 K	20.4 K
$N_{f,ref,i}$	$1.1 \cdot 10^9$	$1.2 \cdot 10^8$	$2.2 \cdot 10^8$	$1.1 \cdot 10^8$	$1.4 \cdot 10^8$
$\Delta T_{j,cntr,i}$	7.3 K	15.1 K	11.0 K	18.6 K	15.8 K
$N_{f,cntr,i}$	$2 \cdot 10^{10}$	$6.6 \cdot 10^8$	$3.5 \cdot 10^9$	$2.2 \cdot 10^8$	$5.2 \cdot 10^8$
$q_{Nf,i}$	18.2	5.5	15.9	2.0	3.7

Table 4.3: Thermal cycle amplitudes and number of cycles to failure

A reduction of the thermal cycle amplitudes is achieved for both, junction and case temperatures. Besides a slight increment of the average temperature has taken place for both measurements. The thermal cycle amplitudes are shown in Table 4.3 for the five occurring major thermal cycles. To evaluate the impact of the thermal control, the Bayerer lifetime model is applied. The number of cycles to failure N_f is noted for each thermal cycle. For better comparison, the quotient $q_{Nf,i}$ is given to represent the factor of increment in the number of cycles to failure achieved by the active thermal control.

Subsequent, Miner's Rule [111] is used to compute the amount of cumulative damage taken by one run of the profile for both curves, fixed c_{ref} and thermal controlled c_{cntr} switching frequency:

$$c_{ref} = \sum_{i=1}^{5} \frac{n_i}{N_{f,ref,i}} = 3.00 \cdot 10^{-8} \tag{4.38}$$

$$c_{cntr} = \sum_{i=1}^{5} \frac{n_i}{N_{f,cntr,i}} = 8.32 \cdot 10^{-9} \tag{4.39}$$

When the cumulative damage reaches 1, the device fails according to Miner's Rule. The number of cycles is set to $n_i = 1,\ \forall i$, as every thermal cycle amplitude occurs only once in the profile. To give a more descriptive result on the impact of lifetime, the amount of cumulative damage is converted to the number of repetitions of the given mission profile until failure:

$$N_{f,profile,ref} = \frac{1}{c_{ref}} = 3.3 \cdot 10^{7} \tag{4.40}$$

$$N_{f,profile,cntr} = \frac{1}{c_{cntr}} = 1.2 \cdot 10^{8} \tag{4.41}$$

As a result, the lifetime of the module can be extended by a factor more than 3 using the proposed active thermal control algorithm on the given mission profile. The enhanced lifetime saves costs and materials due to reduced replacement parts, maintenance and loss of production. The drawbacks are additional losses resulting in higher average temperatures and additional energy consumption costs in operation.

4.5.5.2 Electric vehicle application

The mission profile of a 20 minutes urban drive of a small electric vehicle without energy recuperation is run on the experimental setup. Junction temperatures are measured with and without the use of active thermal control. The results are shown in Figure 4.22.

Again, a reduction of the thermal cycle amplitudes is achieved for both, junction and case temperatures. Besides an increment of the average temperature occurred for both measurements. During acceleration after stop low fundamental frequencies and high currents occur resulting in temperature swings. These fundamental frequency thermal cycles can not be reduced with the proposed thermal control structure for the given H-bridge setup. During low load on one IGBT, the opposite IGBT has a high load in a fundamental period. Therefore, an increment of the switching frequency would lead to increasing temperatures in both IGBTs and the thermal cycle amplitude in the opposite IGBT would increase.

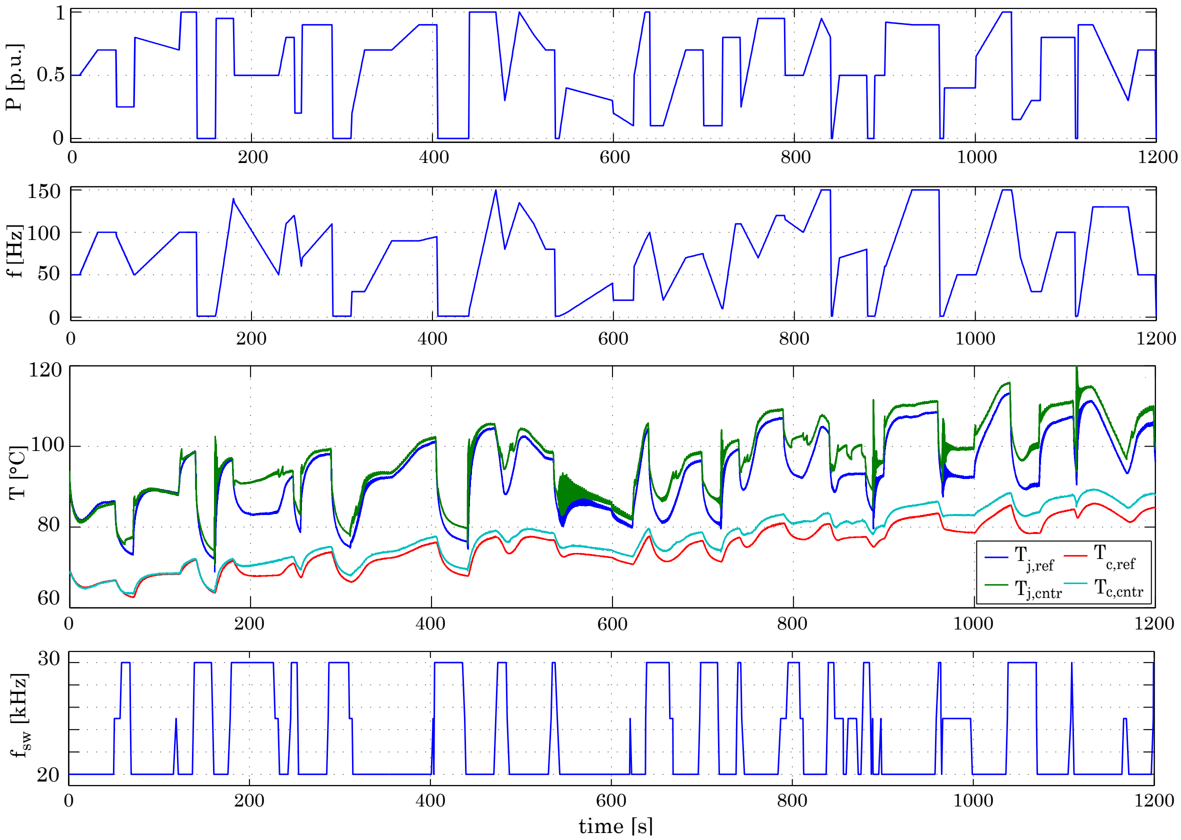

Figure 4.22: Electric vehicle temperature profile with and without active thermal control. Output current is controlled to fit $\hat{i} = 12\,\mathrm{A}$ times the mission profile and given fundamental frequency, dc voltage $v_{dc} = 400\,\mathrm{V}$, uncontrolled switching frequency $f_{sw} = 20\,\mathrm{kHz}$.

The amount by that a thermal cycle can be reduced depends on the remaining losses that can be scaled within a thermal cycle. On a remaining partial load, as the cycles in $600\,\mathrm{s} < t < 800\,\mathrm{s}$ they can be reduced quite efficiency, as the increment of the switching frequency leads to a fair amount of additional losses for partial load. However, if the mission profile is reduced to zero, an increment of the switching frequency does not have the same effect, as only a small residual current is flowing having not much effect on the power losses and therefore temperature.

The overall reduction of thermal cycles is less distinct than in the previous crane application. Since the electric vehicle urban drive mission profile includes segments of no power, the proposed thermal control can only add a slight amount of additional losses in these segments when increasing the switching frequency. In changes from full to partial load, thermal cycles can be reduced more efficient as the thermal control has a stronger effect on the losses.

To analyze the impact of the reduced thermal cycling in the used electric vehicle mission profile, a rainflow counting algorithm is performed on the measurement data of the IGBT junction temperature. This is given in Figure 4.23. Thermal cycles below 2 K are not considered in order to focus on the thermal cycles caused by fluctuations of the load. The total number of thermal cycles N is not changed when applying the active thermal control, but its distribution on the area of thermal cycle amplitude ΔT_j and average temperature of cycles $T_{j,avg}$. For most bars with a $\Delta T_j > 4\,\mathrm{K}$, a migration of about 1 K towards smaller amplitude can be observed and most bars having a lesser amplitude migrate by a smaller amount. A slight increment of the average temperature is noted for some bars, but the amount does not stand in a context with either of the parameters.

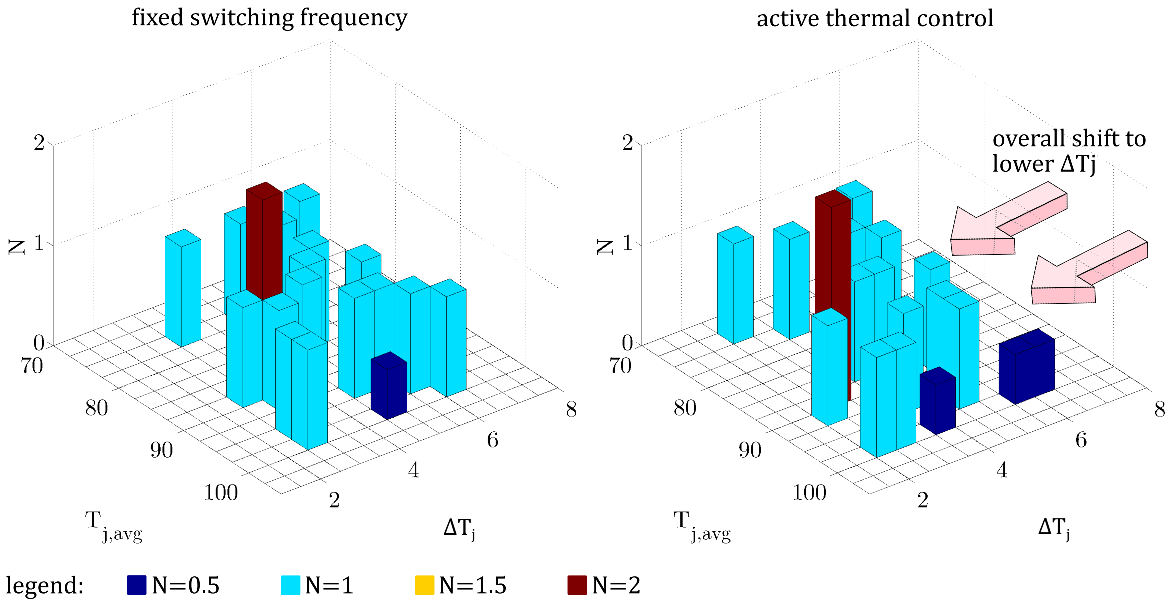

Figure 4.23: Rainflow matrices of the performed electric vehicle mission profile without and with active thermal control.

Altogether, a experimental proofed reduction of thermal cycles is achieved for the electric vehicle application by the use of active thermal control. The small reduction is caused by the overall small amplitude of thermal cycles in this run due to low average power of 2.5 kW and maximum power of 5 kW in this experiment.

4.5.5.3 Industrial process

The active thermal control has been implemented to reduce the thermal stress in the IGBT module on the test setup. The mission profile of an industrial process shown in Figure 4.24 is applied. For comparison the process is also run without the thermal control. A reduction of the thermal cycling amplitude of about 10 % to 30 % can be observed. The model-based condition monitoring according to Figure 4.11 in section 4.4 on condition monitoring has been applied to show the accumulated damage in both cases. The slope of the accumulated damage over time is reduced to a third of its initial value. The reduction in the damage affects an increase of the remaining useful lifetime.

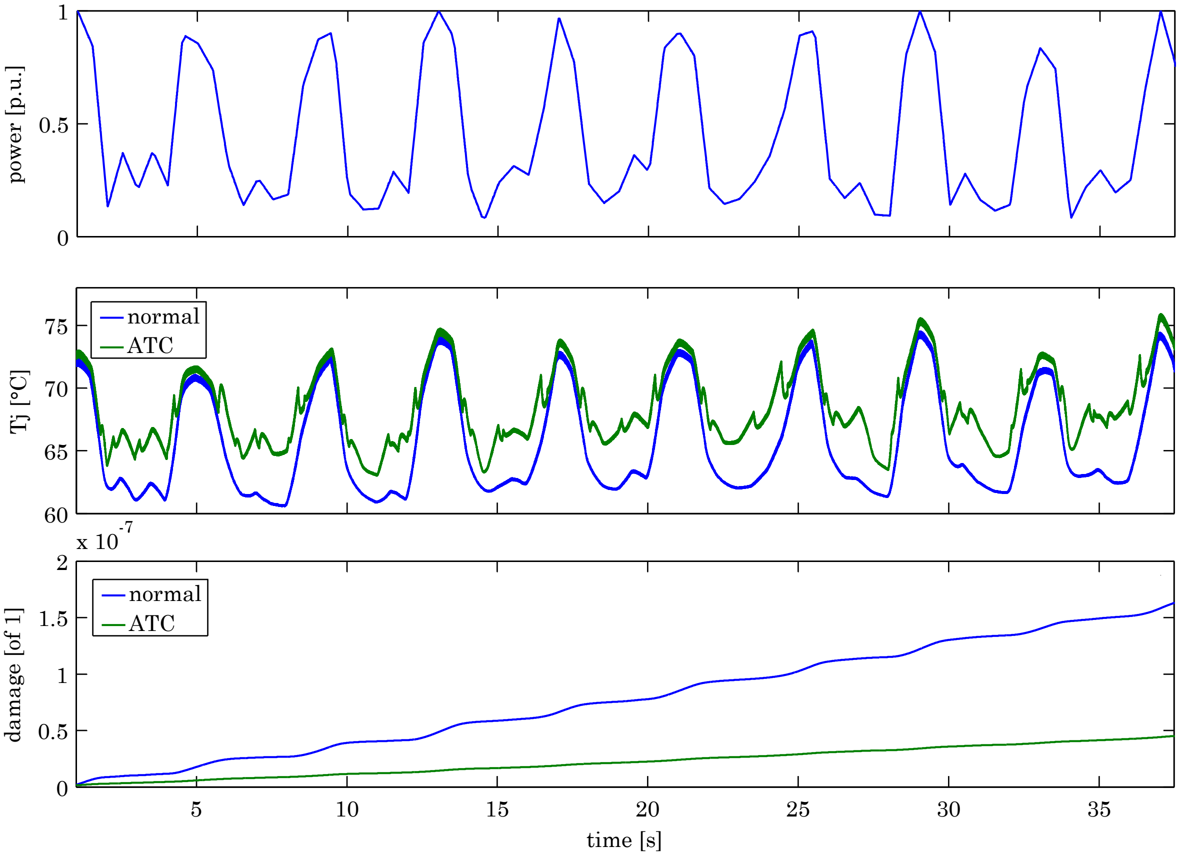

Figure 4.24: Experimental demonstration of the active thermal control and model-based condition monitoring. A mission profile of an industrial process is used.

4.5.6 Capabilities of ATC

Thermal control can be used to lower the amount and amplitude of thermal cycles and therefore increase the module's lifetime and reliability. At this the thermal control is subordinate to the main control (i.e. a current or voltage controller) which means neither the mission profile nor the system constraints must be disregarded at any time by the thermal controller. The mission profile contains commonly information on the demanded active and reactive power or output current, which therefore must not be modified by thermal controllers in most cases. System constraints may involve electromagnetic compatibility and standards regarding total harmonic distortion, which are limiting but not excluding the alternation of the switching frequency or of the output waveform.

When designing a thermal controller for an application system, it is assumed that the system is already optimal constructed concerning efficiency and legal constraints. Thus the switching frequency, for example, is already configured to its minimal permitted value and cannot be reduced any further by the thermal controller in order to decrease power losses temporary. This strict regulation ensures true enhancements when evaluating simulation and experimental results of new thermal control algorithms.

Consequential, this means thermal control cannot be a possibility to improve the systems electrical efficiency coefficient, in fact it may even deteriorate the systems electrical efficiency. However, considered on the whole, energetic and economic benefits of thermal control will dominate increased power losses when it is used properly, as shown in a Fermi-estimation next.

Fermi-estimations are used to obtain approximate values for a problem whose parameters are not known exactly or spread widely. In this case it is investigated how long a thermal controller may increase losses to prevent a single thermal cycle and the benefits still outweigh the drawbacks. Knowing the order of magnitude of this time, it can be determined for which mission profiles and therefore applications thermal control is appropriate. First, parameter estimations for a fictional inverter system are done in table 4.4.

Parameter	**Symbol**	**Value**	**Unit**	**Comment**
Inverter power	P_{inv}	40	kW	
Inverter losses	P_{loss}	400	W	1 % P_{inv}
Additional losses	$P_{loss,add}$	100	W	if activated by thermal control
Energy cost	c_E	0.20	EUR/kWh	
Module replacement cost	c_M	1000	EUR	module + service

Table 4.4: Parameters used for Fermi-estimaion.

The additional rate of costs c_{add}, arising when the thermal controller activates increased losses to prevent thermal cycles is written as

$$c_{add} = P_{loss,add} \cdot c_E = 100\,\mathrm{W} \cdot 0.20\,\frac{\mathrm{EUR}}{\mathrm{kWh}} = 5.5 \cdot 10^{-6}\,\frac{\mathrm{EUR}}{\mathrm{s}}. \tag{4.42}$$

Employing the dependency between cycles to failures and amplitude of a thermal cycle given prior in the lifetime modeling in section 4.3, the costs per thermal cycle c_{Cy} can be expressed as

$$c_{Cy} = \frac{c_M}{N_f}. \tag{4.43}$$

Combining the rate of costs with the costs per thermal cycle, the maximum time t_{max} to activate the additional losses can be determined as

$$t_{max} = \frac{c_{Cy}}{c_{add}}. \tag{4.44}$$

Using the Bayerer lifetime model and equations (4.43) to (4.44), the maximum time to apply additional losses to prevent a thermal cycle with a given amplitude is presented in table 4.5.

As this is a Fermi-estimation, results cannot be interpreted by their actual value, but only by their order of magnitude. Thus, the result of this Fermi-estimation is that

ΔT_j in [°C]	N_f	c_C in [EUR/cycle]	t_{max} in [s]
20	10^8	0.00001	1.8
30	10^7	0.0001	18
45	10^6	0.001	180

Table 4.5: Fermi-estimation results.

thermal control can reduce long-term costs of a system, if it is capable to reduce thermal cycles by increasing losses for the time of a few seconds to a few minutes per thermal cycle.

A general listing of periods that occur in applications and in power electronics control systems is given in Figure 4.25.

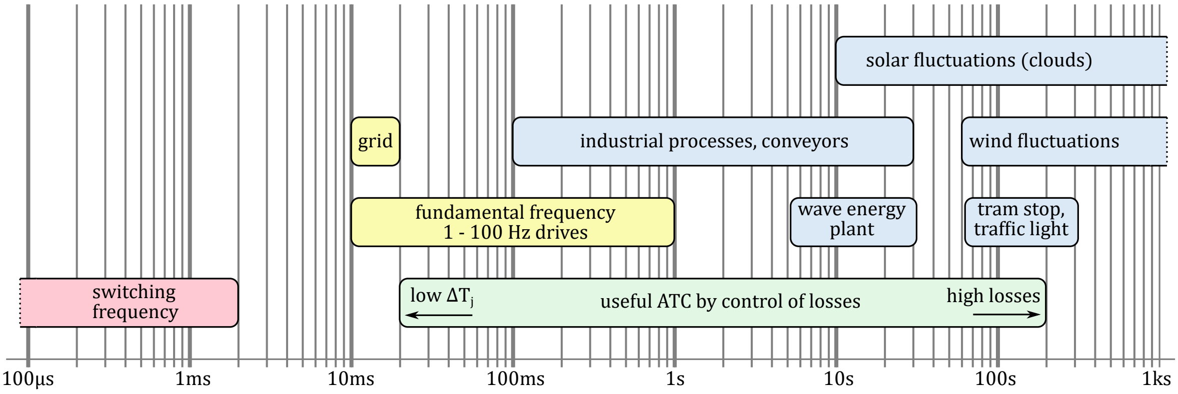

Figure 4.25: Periods that occur in power electronics applications and in the control system.

The bandwidth that is useful for ATC utilizing the power losses is given in the diagram. It is limited as follows: Thermal cycles with a period of less than about 20 ms have an amplitude of less than 3 K, which do not effect the module's lifetime as the material strain is still elastic in this order [119]. Thermal cycles with a period of more than 200 s cause additional losses, which make the use of ATC inefficient according to the Fermi estimation.

This overlaps with the time periods of thermal cycles in the mission profile of regenerative energy plants such as photovoltaic, wind power and wave energy. Also train stops of urban railway and traffic lights overlap, which includes electric metro, buses and vehicles. The best overlapping is for industrial processes such as conveyors, cranes, robotic arms, sorting plants, etc. The fundamental frequency of electric drives overlaps for slow speeds. However, the fundamental frequency of the grid and railway grid causes no relevant thermal cycles in general. Thermal cycling caused by the switching frequency is even less relevant. All these periods serve to give an overview of general time constants and can differ in individual cases.

4.6 Power routing

Power routing itself is not necessarily a technique to reduce the thermal stress in power converters. However, it can be employed to increase the reliability and therefore it is represented here. As the Smart Transformer is a promising application for power routing it is outlined first. Afterwards the concept of power routing and the power routing to improve reliability are described.

4.6.1 Concept of the Smart Transformer

The structure of conventional electric grids is build in layers that are based on the idea of power flow in only one direction: Large power plants are connected in a extra high voltage grid of up to 380 kV. In the high voltage grid of mostly 110 kV medium sized power plants and factories with high energy demand are connected. In the medium voltage grid of 1 kV to 50 kV city power plants, wind power plants and industrial customers are connected. In the low voltage grid of 400 V households are connected. Conventional transformers are used to convert the voltages between the grids. Consequently, control of the power flow and connection of dc systems is not possible. However, the demand for more renewable energy needs additional functionalities to connect intelliget loads, storage devices and dc grids [133] as well as control the load of grid feeders.

A possibility that enables power flow control are solid state transformers (SST). SSTs are basically ac to ac power electronics converters that replace conventional transformers. Architectures of the SST are built with one to three stages. A one stage solution is a direct ac-ac converter like the matrix conveter. The two stage configuration is a ac-dc and a dc-ac converter. The three stage topology has an additional dc-dc converter that enables connectivity to the dc link and guarantees the decoupling of input and output voltages and currents.

Especially the three stage SST provides the system control more degrees of freedom and the possibility to connect to the dc link. A SST between the medium voltage grid and the low voltage grid can provide services to both nets. It provides hybrid (ac and dc) and multimodal connectivity and allows power flow control. Because of its increased functionality a SST for this purpose is also called a Smart Transformer (ST) [134].

Modular architectures of the ST allow to increase the efficiency and use low volage power semiconductors. The modular design consists of several cells rated for LV or low current, which are the building blocks of the entire system [134]. In periods with only partial demand of power it is more efficient to use only the amount of building blocks that is necessary to fulfil the demand on power and disable the remaining building blocks. This procedure saves the power losses that would apply in the disabled building blocks and generates only minor additional losses in the active devices, as they can run in their optimal efficiency operating point.

4.6.2 Concept of power routing

Power routing is a method to route the power through the building blocks of a modular power converter like the modular ST. This enables to control the load of the building blocks in the power converter. Without power routing a given power is shared equally between the building blocks. Power routing allows to specify the amount that is processed in each building block.

The power routing can benefit different aims. Aims can be to minimize the power losses in a microgrid [135] or to maximise the system loadability of an islanded microgrid [136]. The aim that is relevant for this section is the possibility of active thermal control through power routing [134], [137].

In the modular converter the buliding blocks are connected in series, parallel or a mixture of both. In a serial connection the current through all building blocks is constant. However, the output voltage of a specific building block can be variated in order to control the processed power of that building block. In a parallel connection all building blocks share the same voltage. In this case the output current is a degree of freedom that can be used to control the power of a specific building block. Consequently, in a mixed configuration of series and parallel, both, voltage and current are used to control the power of the building blocks [134].

4.6.3 Power routing to increase the reliability

Power routing can be used to unevenly load building blocks in modular power converters and thereby control the stress for all devices in a specific building block. It is proposed to equalize the useful remaining lifetime of the building blocks in modular power converters in order to enable planned maintenance.

Key of active thermal control through power routing is the direct relation between the device temperature and its lifetime as explaind in section 3.4. The temerature of a specific building block is dependent on the power losses that apply in that building block. As the power routing controls the power that is processed in a specific building block, it can also be used to control the temperature of that building block.

The active thermal control presented in the previous section can be applied in a modular converter, but their disadvantages by means of increased losses remain. The power routing was proposed for series connected building blocks [138], parallel connected building blocks [139] and building blocks connected by a multi-port transformer [140]. The advantage of the method is the low impact on the efficiency, whereas a disadvantage is increases stress for other building blocks in the system.

In the event of a failure, maintenance needs to be scheduled contemporary to replace the faulty device. For complex systems, shut down, disassembly, repair and reboot of the system is time consuming and causes high costs. Therefore, the maintenance is most efficient in costs, if several tasks can be solved at a single event. A high number of redundant cells can enlarge the periods between maintenance, but this increases the costs for the system in general.

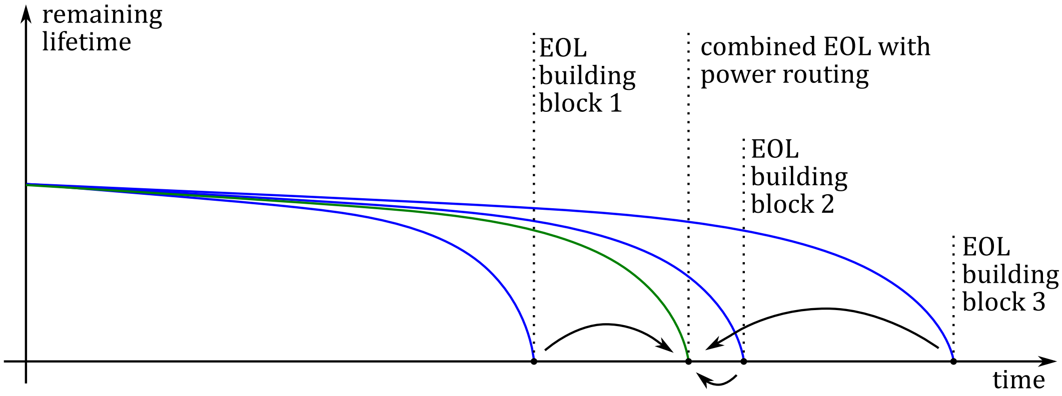

Figure 4.26: Power routing concept for three building blocks with different lifetimes.

The power routing is applied to equalize the useful remaining lifetime in the building blocks. This concept is demonstrated in Figure 4.26 for three building blocks with different lifetimes. The lifetimes may vary due to different times of prior replacement, different building quality or working conditions in duty. The different prognosticated times for end of life (EOL) require three times maintenance. The advantage of the new combined time for EOL is that maintenance is required only once.

4.7 Conclusion of the chapter

Active methods are part of the overall concept to increase the reliability of power electronics systems. Condition monitoring has none or only minor impact on the operation of the system and can provide useful information on the systems fitness in use, which allows to anticipate the time of reliable operation. Active thermal control can be implemented as a pure software approach. This makes it a low-cost solution. It is a technique to reduce the thermal stress of power semiconductors for achieving higher reliability of the system. The active actions can happen at several levels, from the very low level of the gate driver, to the system level, where the presence of multiple power converters is exploited. The possible benefits are avoiding the components de-rating or increasing their lifetime.

A reduction of thermal cycles in power electronic modules could be achieved for different applications using active thermal control. This is also possible by only increasing the switching frequency compared to the not thermal controlled reference. A possibility for online junction temperature estimation without additional sensors has been introduced and applied for active thermal control. This allows a subsequent adoption of active thermal control without changes to the system hardware. Experimental verification provided that the accuracy of the temperature estimation is in good match with the measurement for fundamental frequencies up to 10 Hz. Higher frequencies could not be validated. Experimental comparisons of temperature profiles with and without active thermal control showed a possible reduction of thermal cycles amplitudes that can increase the module's lifetime by a factor of 3 according to the Coffin-Manson model and Miner's accumulated damage rule.

5. FCS-MPC to reduce the thermal stress of power electronic modules

The main disadvantage of active thermal control is the decrease of the overall system efficiency or system performance [141]. In addition to the performance deterioration, additional thermal control loops increase the complexity and the accumulated damage of the semiconductor is not taken into account.

In this chapter a control approach that aims at overcoming these limitations to widen the use of active thermal control in power electronic applications, especially for electric drives. For this purpose finite control-set model predictive control (FCS-MPC) seems the optimal approach, because it allows an optimal control of every switching event and including of non-linear thermal and lifetime related models into the control law. A precise control of the thermal stress in the semiconductors can be achieved as the optimal switching vector is directly applied to the physical system. A model for online junction temperature estimation that is suited for the use of FSC-MPC is designed. The proposed algorithm is a software solution for increasing the reliability and does not utilize special hardware like extra temperature probes nor active gate drivers.

5.1 FCS-MPC temperature estimation

The knowledge of the junction temperatures is necessary to apply active thermal control. As discussed in section 4.2 on the junction temperature detection, measurements that meet the bandwidth demand for the control are challenging. Therefore, several temperature sensitive electrical parameters (TSEP) have been introduced to obtain the chip temperatures [104]. A less invasive method is to use model-based estimations of the junction temperatures. The junction temperature estimation is based on power loss calculations and the thermal properties of the device's cooling path. Both can be described in models for online calculation. This has been presented for PWM based control systems in the section.

The FCS-MPC is a direct control without use of a modulator and with a variable switching frequency. Thus, the existing model given in section 4.2 is not applicable. An adapted junction temperature estimation model shown in Figure 5.1 is designed next using a power loss calculation and a thermal network: The conduction losses are calculated using the v_{CE} characteristic of the semiconductors and the collector current i_c, which is derived from a measurement of the phase current. The switching losses are given with the switching energy characteristics E_{on} and E_{off} of the semiconductors and the sampling time. Switching of the device is determined by the FCS-MPC algorithm and therefore, all switching operations are known to the control. The switching energy loss is only considered if a switching occurs and is set to zero otherwise.

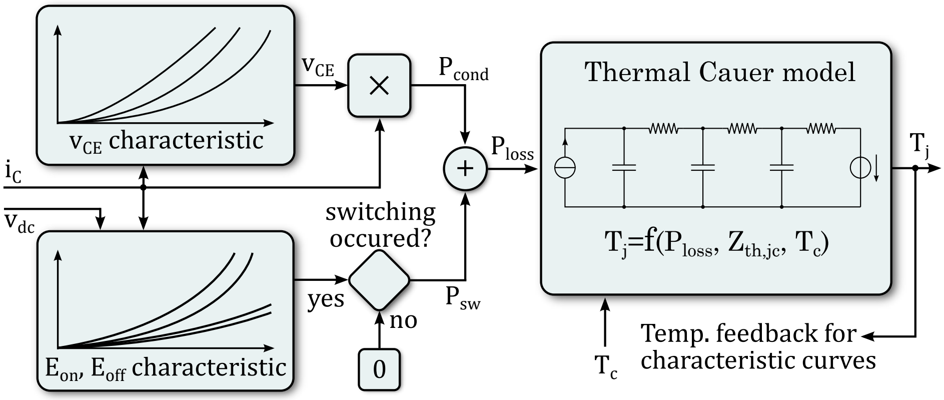

Figure 5.1: Online junction temperature estimation model for FCS-MPC.

A linear Cauer-type thermal network as applied in section 4.2 is used to calculate the temperatures that occur in the module's layers based on the power losses, a low-bandwidth temperature measurement of the modules case T_c that is often included in packages and the thermal impedance between junction and case $Z_{th,jc}$. This enables to estimate the junction temperatures.

5.2 Thermal-based FCS-MPC procedure

Active thermal control can benefit from the non-linear control structure of MPC. Additional, FCS-MPC offers the possibility to apply a particular space vector directly to the inverter system as no modulator is used in this control structure. In this section, the proposed procedure is developed first. Secondly, the effectiveness is demonstrated using simulation. In the end, experimental results are given to validate the behavior using an infrared camera. The procedure of the general FCS-MPC is described in section 2.2.

The purpose of the algorithm is to keep the fatigue of the module low by reducing the thermal stress. In contrast to other active thermal control studies, it also allows to equalize the junction temperatures in the power module. The power losses are changed according to the stress that results from thermal cycles. The gain is adjusted using λ-coefficients that are introduced in this section. This allows tuning to have the maximum allowed power losses in the case of the maximum thermal stress. When the cycle ends, its amplitude vanishes and operation is reset to normal. This behavior actually limits the increase of the additional power losses that may be introduced by other active thermal control studies.

The FCS-MPC allows predicting the current, power losses, junction temperatures and accumulated damage for all possible space vectors at each sampling instant. The principle of the FCS-MPC is to predict these parameters for sample time instants n and space vectors k and score each prediction using a cost function. To choose the most suitable space vector for the next sampling instant the minimal cost function is searched.

As no modulator is used, this space vector is directly applied to the system. Figure 5.2 shows the general scheme of this FCS-MPC. The load current, junction temperature and the resulting thermal stress are predicted for all space vectors of the next sampling instant. These predictions are used to derive the FCS-MPC cost function parameters that include the error from the current reference, the thermal stress on the device, the temperature difference between the chips on a power module and the total power losses from switching and conduction the semiconductors. These parameters are weighted and the space vector with the lowest cost function is directly applied to the power converter.

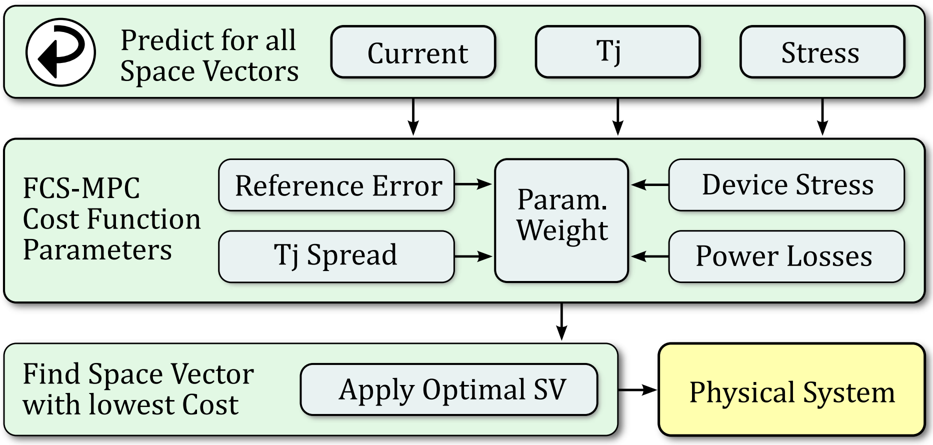

Figure 5.2: Structure of the FCS-MPC adapted for reduction of the thermal stress.

The control system schematic of the thermal-based FCS-MPC is given in Figure 5.3. It is based on the FCS-MPC derived from the field oriented control in section 2.4. In the outer control loop the magnetization and speed of the machine are controlled with PI controllers and the help of a rotor flux estimator. The inner loop is controlled by the FCS-MPC. It uses measurements of the inverter currents for the control of the desired operation point. Additional measurements of the dc link voltage and the module's case temperature are used to estimate the junction temperatures in the model used for the active thermal control.

The flow chart of the FCS-MPC procedure is given in Figure 5.4 for iteration n which corresponds to a one-step prediction horizon. To increase the prediction horizon, the procedure has to be executed again for each resulting space vector. The execution of the procedure can be time consuming, especially if the prediction horizon is increased. For this reason, in iteration n the calculation of the optimal space vector is done for the next iteration $n+1$ and it is applied on the converter at beginning of that iteration.

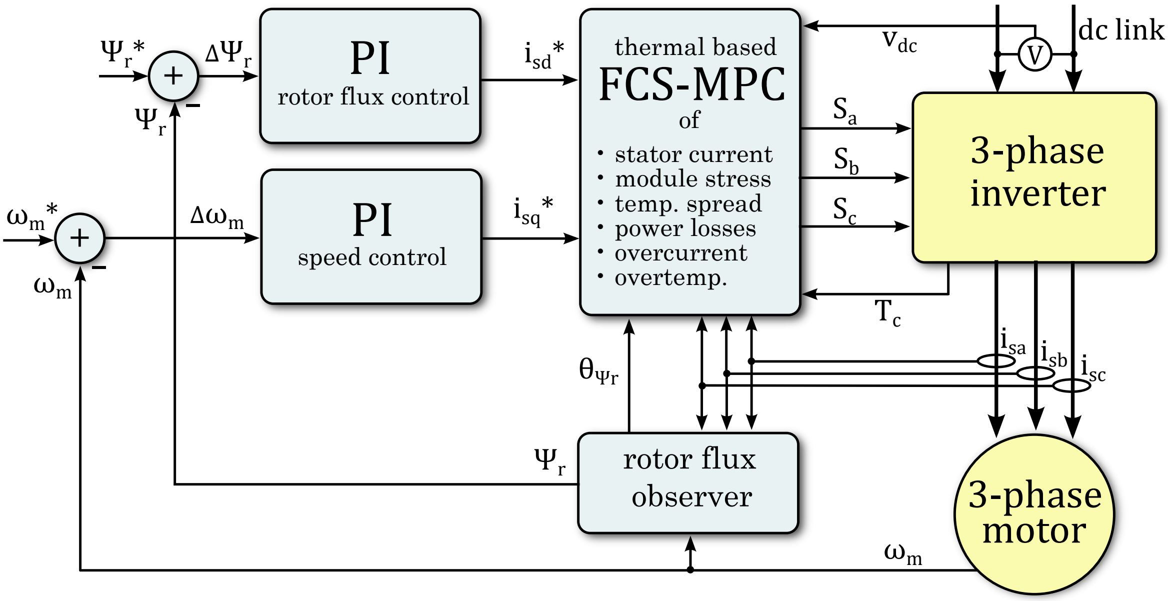

Figure 5.3: Schematic of the proposed thermal-based FCS-MPC control system. The FCS-MPC is used for a multi-parameter optimization.

The cost function that needs to be minimized consists of a compilation of all quantities that are involved in the optimization:

$$\begin{aligned} g(n,k) = g_i(n,k) + g_c(n,k) + g_{sp}(n,k) + g_{loss}(n,k) \\ + g_{imax}(n,k) + g_{Tmax}(n,k) \end{aligned} \tag{5.1}$$

The symbols of the cost function equation are given in Table 5.1. For the proposed thermal-based control it includes elements for the current reference error, the amount of damage that a thermal swing adds to the module, the spread of junctions temperatures from a mean value and the amount of energy that is necessary for the predicted switching operation. The elements of the cost function are weighted by λ-coefficients to make it tunable for the desired application. Additional constraints for the maximum device current and the maximum junction temperature are added. The cost function elements are established in the following for each part in particular.

Cost function element	**Gain**	**Symbol**
Error from current reference	λ_i	$g_i(n,k)$
Additional device damage	$\lambda_{c,l}$	$g_c(n,k,l)$
Device junction temperature spread	λ_{sp}	$g_{sp}(n,k)$
Power losses (switching & conduction)	λ_{loss}	$g_{loss}(n,k)$
Maximum device current constraint	-	$g_{imax}(n,k)$
Maximum device temperature constraint	-	$g_{Tmax}(n,k)$

Table 5.1: Predicted cost function elements

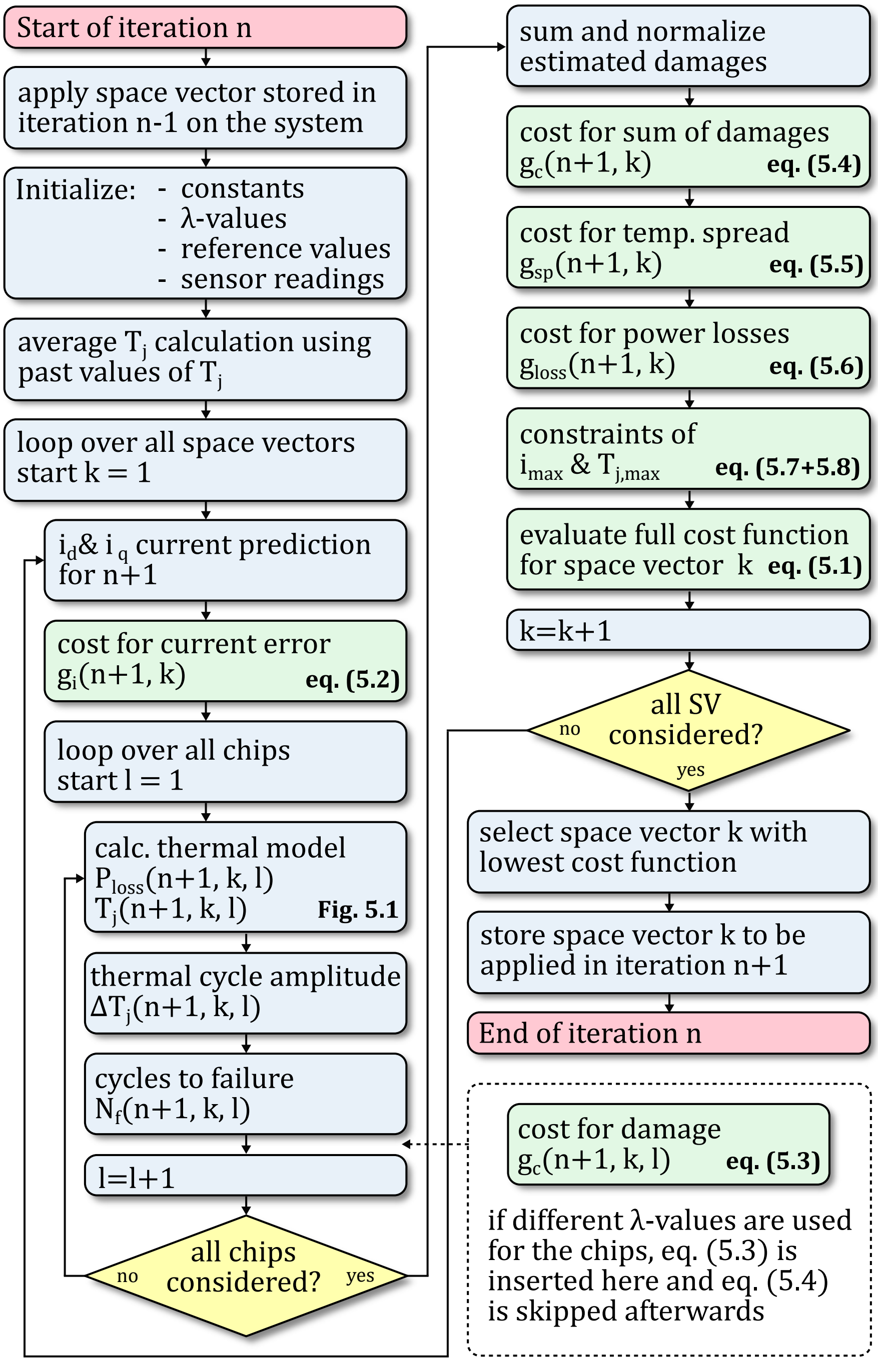

Figure 5.4: Flow chart of the proposed thermal-based FCS-MPC procedure.

First part is the current reference error. Typically the absolute value of current error to its reference value is chosen for both, d and q component of the current [142]. The cost function element for the current error g_i is denoted as:

$$g_i(n,k) = \lambda_i \cdot (|i_d^* - i_{d,k}| + |i_q^* - i_{q,k}|) \tag{5.2}$$

In this equation i_d^* and i_q^* are the current reference values and $i_{d,k}$ and $i_{q,k}$ are the predicted currents for the applied space vector k in the dq-frame. The current reference is assumed to be constant for sampling instant n.

Next, the additional damage for each semiconductor l in the module is computed for each space vector k using the Bayerer lifetime model of equation (4.29). The thermal swing ΔT_j is the main parameter in the model. To detect the current amount of thermal swing, the deviation from the junction temperatures average value $T^l_{j,avg}$ are computed according Figure 4.12 in section 4.5. The base temperature of the thermal swing $T_{j,min}$ is the minimal temperature of a thermal cycle. For the cost function each term is weighted with $\lambda_{c,l}$.

$$g_c(n, k, l) = \lambda_{c,l} \cdot N^{-1}_{f,n,k,l} \tag{5.3}$$

The calculation of g_c relies on a calculation of the number of cycles to failure N_f for the predicted space vector using the predictions of current and temperature as well as the constant values given in table 4.2. The reciprocal of N_f is a snapshot of the damage at the given time instant. As the starting and ending of thermal cycles are not detected in this procedure it is only suitable for computational light online damage estimation. It ensures that thermal cycles are scored by their potential damage to the semiconductors. A more precise but computational more demanding procedure is the online rainflow counting [115]. It is also suitable for accumulating damage calculation to estimate the consumed lifetime.

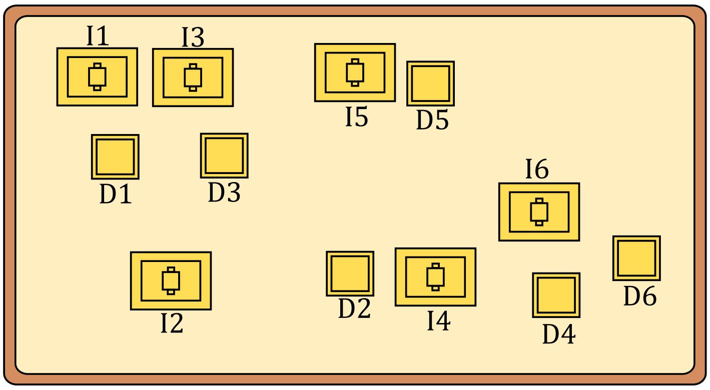

Figure 5.5: Layout of an IGBT module. IGBTs I1 and I2 together with power diodes D1 and D2 form the first phase of the 3-phase module.

Different values for $\lambda_{c,l}$ can be used to quantify the stress that should be relieved from semiconductor l. This enables to equalize the damage in the semiconductors of the module, by relieving the more used ones. In Figure 5.5 the layout of an IGBT module is shown in schematic. Semiconductors that are located next to each other are interacting in temperature. The mutual heating up can be compensated with this coefficient. However, if this is not used, the dependency from l can be removed by using the average of all q chips on the module:

$$g_c(n, k) = \lambda_c \cdot \frac{1}{q} \sum_{l=1}^{q} g_c(n, k, l), \quad \forall \lambda_{c,l} = 1 \tag{5.4}$$

Another element of the cost function allows to reduce or to favor the usage of selected semiconductors of the module. This can be used to relive stress from semiconductors that have been particularly stressed before. It also enables to equalize unequal temperatures in the module. The cost function of space vectors that include the selected semiconductor are evaluated higher or lower according to the control goal:

$$g_{sp}(n,k) = \lambda_{sp} \cdot \mathrm{Var}\left(T_{j,l}(n+1,k)\right) \tag{5.5}$$

The variance of the predicted junction temperatures of all semiconductors l is used to measure how equal the junction temperatures in the module are after applying space vector k. Thus, the cost function element returns low costs for less spread junction temperatures in the module.

The next part of the cost function includes the efficiency, which means reduction of the occurring losses. The dominating losses in the module are the conduction losses and the switching losses [63]. The switching losses can be reduced by choosing space vectors that are neighbored to the previous vector as less semiconductors have to change conductivity [13].

$$g_{loss}(n,k) = \lambda_{loss} \cdot \sum_{l=1}^{q} \left(P_{sw,l}(n,k) + P_{cond,l}(n,k)\right) \tag{5.6}$$

The calculation of the switching losses and conduction losses is given in Figure 5.1.

The last two elements of the cost function are constraints that ensure the safe operation of the inverter. If the condition of a constraint applies, the space vector must not be applied to the system. The cost function's value is set to infinity. For this reason constraints do not have λ-coefficients. If no space vector can be applied the inverter trips.

$$g_{imax}(n,k) = \begin{cases} 0 & |i(n,k)| \leq i_{max} \\ \infty & \text{else} \end{cases} \tag{5.7}$$

$$g_{Tmax}(n,k) = \begin{cases} 0 & T_j(n,k) \leq T_{j,max} \\ \infty & \text{else} \end{cases} \tag{5.8}$$

The cost function is evaluated for all space vectors k. The space vector with the minimal cost is then applied to the system. The λ-coefficients allow to tune the behavior of the control. Decreasing of λ_c and λ_{sp} i.e. will reduce the impact of the thermal control. An example for defining the λ-parameters is given in table 5.2. For instance a current error of 2 A is defined to result in a cost of $g_i = 0.5$ and therefore must be set to $\lambda_i = 0.25$.

Guidelines for selecting of the λ-coefficients are given in section 5.6 in the experimental results.

Cost function element	**Value**	**Cost**	**λ-Parameter**
Current reference error	2 A	$g_i = 0.5$	$\lambda_i = 0.25$
Additional damage	10^{-7}	$g_c = 0.25$	$\lambda_{c,l} = 2.5 \cdot 10^{-6}$
Temperature variance	3 K	$g_{sp} = 0.15$	$\lambda_{sp} = 0.05$
Power losses	200 W	$g_{loss} = 0.1$	$\lambda_{loss} = 5 \cdot 10^{-6}$

Table 5.2: Definition of λ-parameters for simulation

The optimization of the cost function is illustrated in an example in Figure 5.6. To keep it simple, only four of the eight possible space vectors are depicted. If only the cost for current error g_i is minimized, the switching sequence would be 4-1-3-1-2, as space vector 4 has the lowest cost for the current reference error in the first time sample, space vector 1 in the second sample and so on. To find the optimal switching sequence the whole cost function g is minimized. It is the sum of the weighted elements g_i, g_c, g_{sp} and g_{loss}. The resulting switching sequence for the minimal cost function g is 4-1-1-1-2.

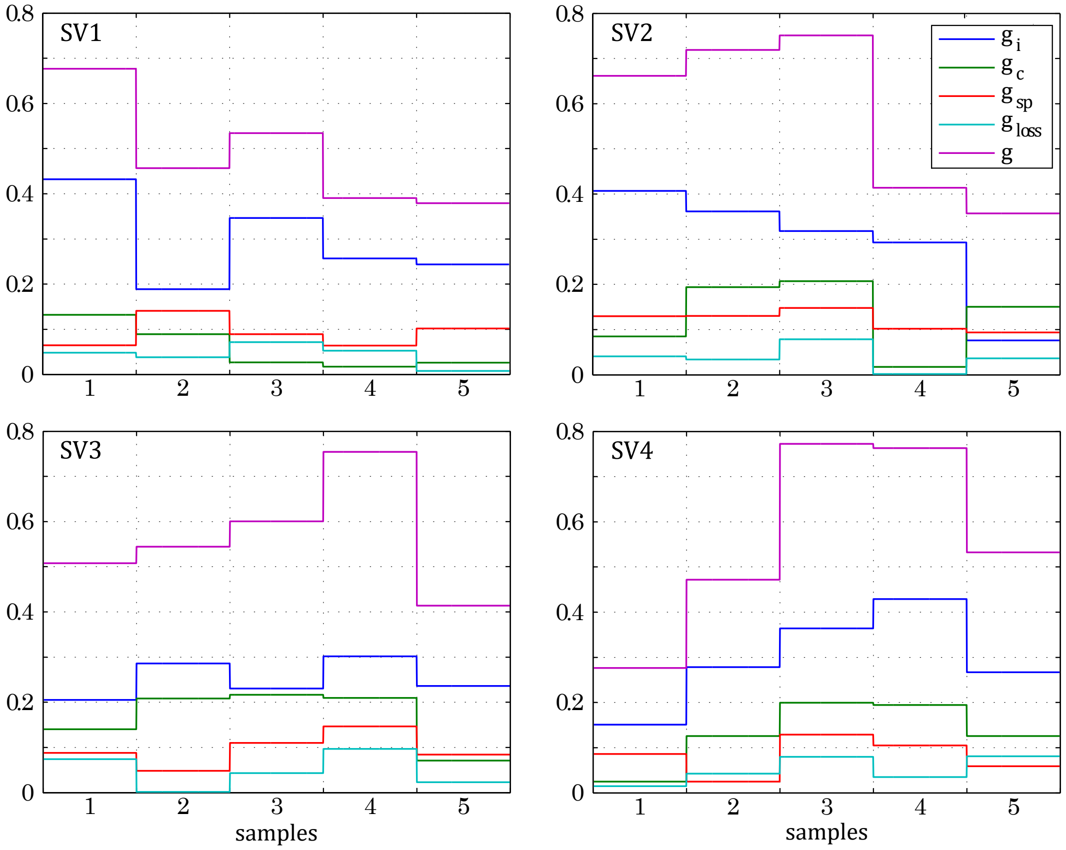

Figure 5.6: Set of cost function elements for four space vectors and five samples.

5.3 Evaluation of the FCS-MPC for thermal control

The FCS-MPC with junction temperature control has been applied in simulation for the control of an induction motor. Rotor flux and machine speed are controlled in a field oriented control scheme using PI controllers. Inverter current and junction temperatures are controlled with the proposed thermal-based MPC. The full scheme of the 3-phase motor control is given in Figure 5.3. It is used to control the motor current and optimize the thermal behavior in a three-phase IGBT module during periodic load changes of the electric drive in a traction application. The mission profile specifies motor turning speed and load torque. The turning speed is kept constant during three trapezoidal load changes per minute. The used parameters for the simulation are given in table 5.3.

Component	**Parameter**	**Symbol**	**Value**	**Unit**
Control system	sampling time	T_s	100	μs
IGBT Module	max. voltage	v_{dc}	1.2	kV
IGBT Module	max. current	I_{max}	50	A
IGBT Module	ambient temp.	T_a	50	°C
Induction Machine	rated power	P_r	11	kW
Induction Machine	rated speed	n_r	1455	rpm
Induction Machine	rated torque	M_r	72.2	Nm

Table 5.3: Simulation parameters

The simulation results are given in Figure 5.7. For comparison, the simulation is run in normal operation and with the proposed active thermal control. In normal operation the λ-coefficients except of λ_i are set to zero and the FCS-MPC is only used to control the load current according to the references of the field oriented control. A thermal cycle amplitude of 30 K arises. In the second run of the simulation the active thermal control algorithm is included to the FCS-MPC cost function optimization. The effect of this active thermal control is a reduction of the thermal cycle amplitude to 20 K at the same boundary conditions.

Using the Bayerer lifetime model introduced in section 4.3 and Miner's cumulative damage rule [111] it is possible to estimate the number of runs of the mission profile to module failure. Assuming this profile is run for 8 hours per day, the lifetime can be given as numbers of years. This is done in table 5.4. As a result, the reduction of the thermal cycle amplitude leads to an increase of the estimated lifetime by the factor of six in this simulation. The drawback is an increased amount of ripple in the stator current during the periods when the control prevents switching operations.

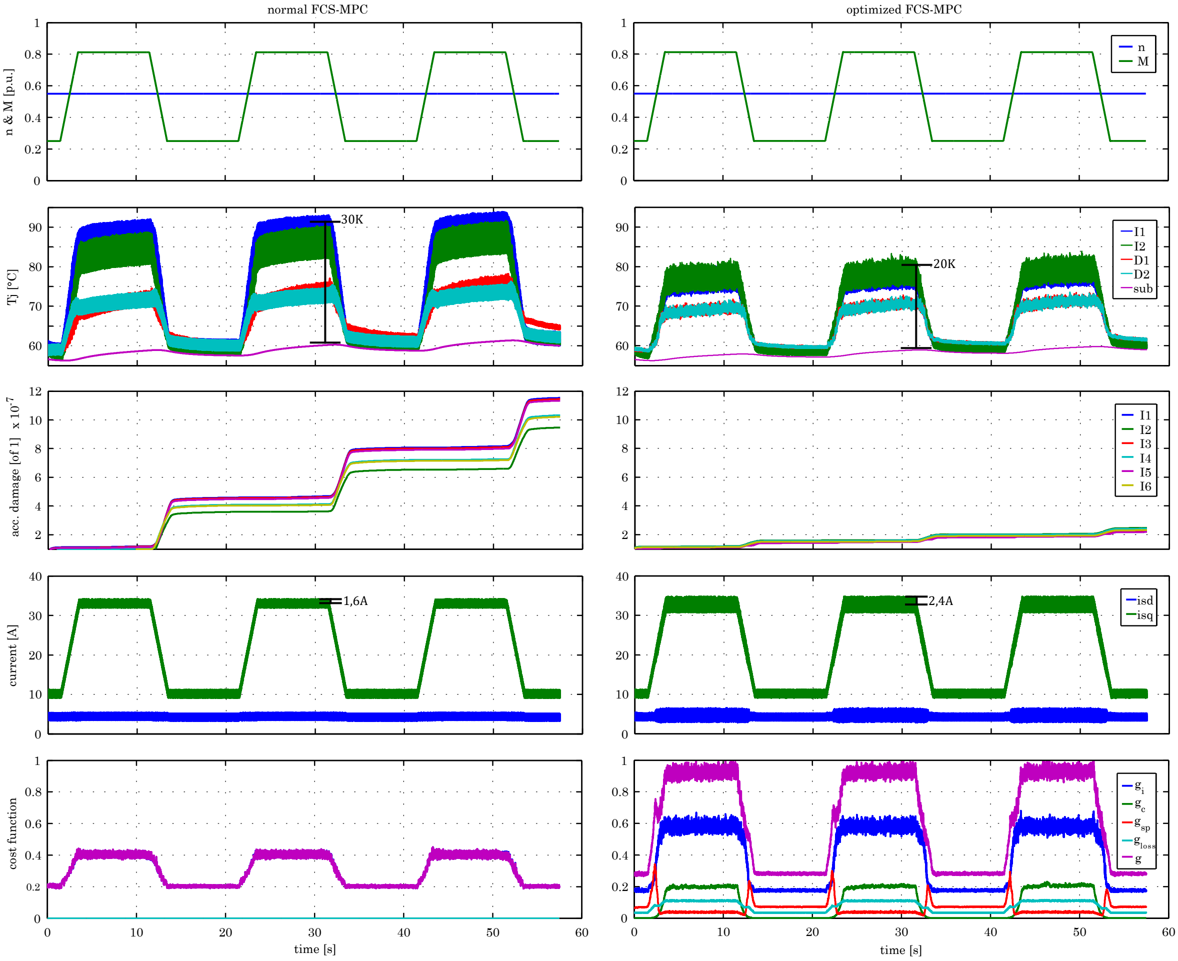

Figure 5.7: Simulation of an IGBT module during a traction application mission profile. The normal FCS-MPC is given in the left column and the thermal optimized behaviour is given in the right column. Turning speed n_r and load torque M_r are given as per unit of the machine's rated operation (see table 5.3). First phase junction temperatures of IGBTs and diodes as well as the module's case temperature are given. The accumulated damage is calculated on basis of equation (4.29). In the bottom plots the values of the minimal cost function are given (lowpass filtered for viability $f_c = 100Hz$). In normal FCS-MPC only the current reference error is minimized. The cost function of the optimized FCS-MPC is weighted using the λ-parameters of table 5.2.

	$T_{j,high}$	$T_{j,low}$	ΔT_j	N_f	est. lifetime
normal	93 °C	63 °C	30 K	$0.26 \cdot 10^7$	4.9 years
optimized	82 °C	62 °C	20 K	$1.54 \cdot 10^7$	29.4 years

Table 5.4: Lifetime estimation for traction mission profile

5.4 Performance and Tuning

The λ-coefficients are used to adjust the control priorities between thermal stress reduction and current ripple. To visualize the effect, a multitude of simulations have been conducted, while varying the ratio of λ_i to λ_c while the other λ-coefficients are set to zero. This varies the gain of current reference error and thermal evoked damage. The effect on on junction temperature swing, lifetime, current ripple and torque ripple are evaluated for each ratio. The temperature cycle amplitude is calculated according to Figure 4.12 in chapter 4.5. The remaining lifetime is calculated using the procedure of the previous paragraph and equation (4.29). As a measure for the current ripple, the root mean square (rms) is applied:

$$i_{s,ripple} = \sqrt{\frac{1}{n} \cdot \sum_{k=1}^{n} (i_s - i_{s,avg})^2} \tag{5.9}$$

In this equation $i_{s,avg}$ is a lowpass filtered signal of the stator current i_s. The torque ripple is calculated using a measure of the electromagnetic torque:

$$T_e = \frac{2}{3} \cdot p \cdot L_m \left(i_{s,q} \cdot i'_{r,d} - i_{s,d} \cdot i'_{r,q} \right) \tag{5.10}$$

As a measure for the torque ripple, the RMS is applied similar to (5.9). The impact on junction temperature swing and current ripple is shown in Figure 5.8. The derived impact on lifetime and torque ripple is shown in Figure 5.9. The tradeoff of these parameters is used to find the optimal gain of the λ-coefficients that fulfills the application dependent demands. The figure shows that always a compromise between reduced stress and additional ripple must be agreed. However, adjusting of the coefficients can be seen as an additional degree of freedom in the system engineering.

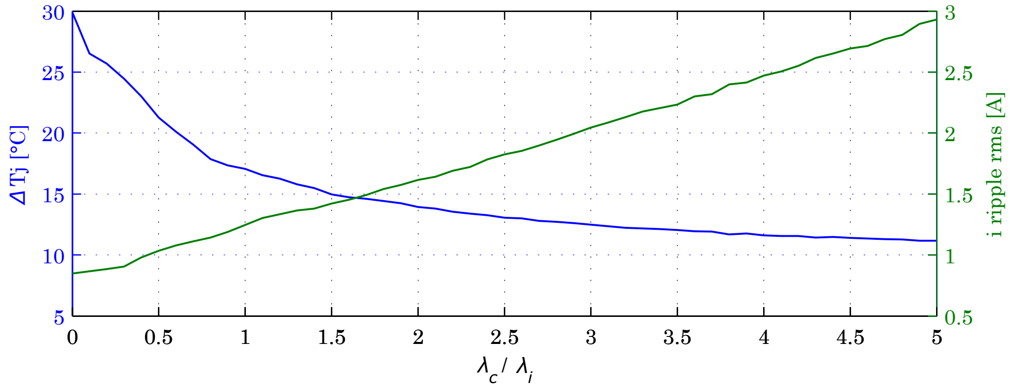

Figure 5.8: Tuning of the thermal-based MPC by varying the normalized ratio λ_c to λ_i. View on temperature cycle amplitude versus RMS of ripple current.

5.5 Equalizing thermal stress in the module

In this simulation, the thermal characteristics of all IGBTs are equal and no aging is assumed. However, in reality the average junction temperatures in an IGBT module may have non-tolerable differences during operation, even the converter is driven with

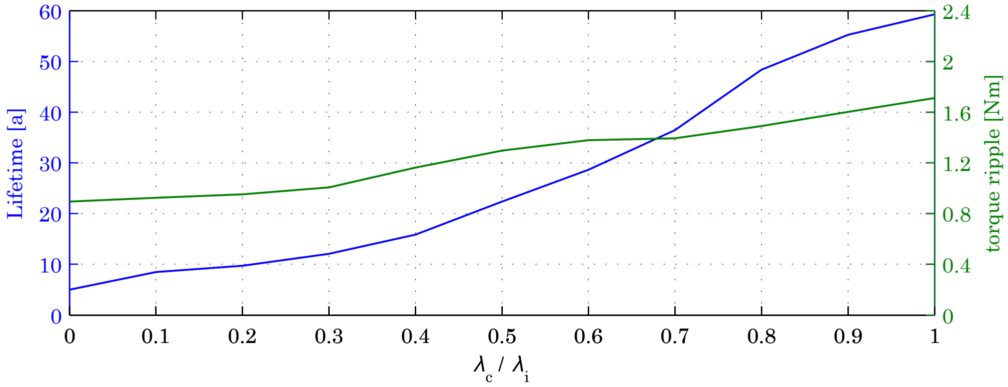

Figure 5.9: Tuning of the thermal-based MPC by varying the normalized ratio λ_c to λ_i. View on lifetime (mission profile of Figure 5.7) versus torque ripple.

a symmetric load. One reason is the non-symmetric design of power modules. Semiconductors that are placed next to others receive additional heat. Thus, semiconductors that are located in the middle of the module receive more heat than those that are located at the edge. Another reason is that aging of the semiconductors does not occur concurrent due to tolerances in the fabrication. Thus, the thermal characteristics and the heat transfer capability change over time.

If the first semiconductors in a module fails due to aging, is has reached end of life and the whole module has to be replaced. Consequently, if the speed of aging could be equalized, the modules lifetime would be maximized. A possibility to influence the aging of a semiconductor is to control its thermal stress.

The proposed control structure offers the possibility to relieve thermal stress from selected IGBTs or diodes. As the FCS-MPC does not use a modulator, it has direct influence on the space vector that is applied on the converter. For each space vector, the involved semiconductors are known. Consequently, the turn-on or the conducting for multiple sampling times of this semiconductor can be included to the MPC cost function as an additional penalty term. In the optimization routine of the MPC, the space vector with the lowest costs is applied to the system. Space vectors that include the selected semiconductor obtain a bias in the optimization, which results in less usage of the semiconductor. This leads to decreased power losses and therefore a lower average temperature. According to the Coffin-Manson-Arrhenius lifetime model, this reduces stress and thus the aging. The possibility to influence single chips on the module is demonstrated in the experimental results.

5.6 Experimental results

The experimental validation is done on a three-phase two-level dc/ac inverter. An open IGBT module without the use of isolating gel filling is used. This allows direct temperature measurements on the chips but decreases the isolation voltage below the rated values. For power input dc power supply is used. The load is an induction machine that is mechanical connected to a torque machine. The control is implemented on a dSPACE DS1006 processor board. The parameters of the experimental setup are given in table 5.5. A photograph of the measurement system is given in Figure 11.3 and a photograph of the machine test bench is given in Figure 11.2 in the appendix.

Component	**Parameter**	**Symbol**	**Value**	**Unit**
Control system	sampling time	T_s	50	μs
IGBT Module	max. voltage	v_{dc}	1.2	kV
IGBT Module	max. current	I_{max}	25	A
Induction Machine	rated power	P_r	5.5	kW
Induction Machine	rated speed	n_r	1455	rpm
Induction Machine	rated torque	M_r	36.1	Nm
Infrared camera	used bandwidth	f_{ir}	200	Hz
Infrared camera	rated accuracy	T_{err}	± 0.02	K

Table 5.5: Experimental setup parameters

For illustration of the junction temperatures in the physical setup, a high speed infrared camera is used. The thermal-based FCS-MPC algorithm has no access to the measured temperatures. It is relying on the model-based junction temperature estimation.

To validate the reduction of the thermal stress by using the proposed FCS-MPC, it has been applied on the experimental setup. In a first experiment, the stress during acceleration of the induction machine and during high torque peaks is relieved. In a second experiment it is demonstrated how the proposed FCS-MPC can be used to equalize unequal stress distributions of the semiconductors in an IGBT module. For both experiments the machine control scheme equals that one used for the simulation given in Figure 5.3.

5.6.1 Experiment to reduce stress

The experimental results are given in Figure 5.10. As a consequence to the high gradient in the junction temperatures, the FCS-MPC is selecting switching patterns that constitute less switching losses. This can be seen in the temporary decrease of the average switching frequency during acceleration. Therefore, the amplitude of the thermal overshoot is reduced by more than 40 %.

5.6.2 Experiment to equalize stress in semiconductors

The possibility to influence single chips on the module is demonstrated. The FCS-MPC is used to equalize the temperatures of all IGBTs in the module. This has the effect that their fatigue is also more equalized.

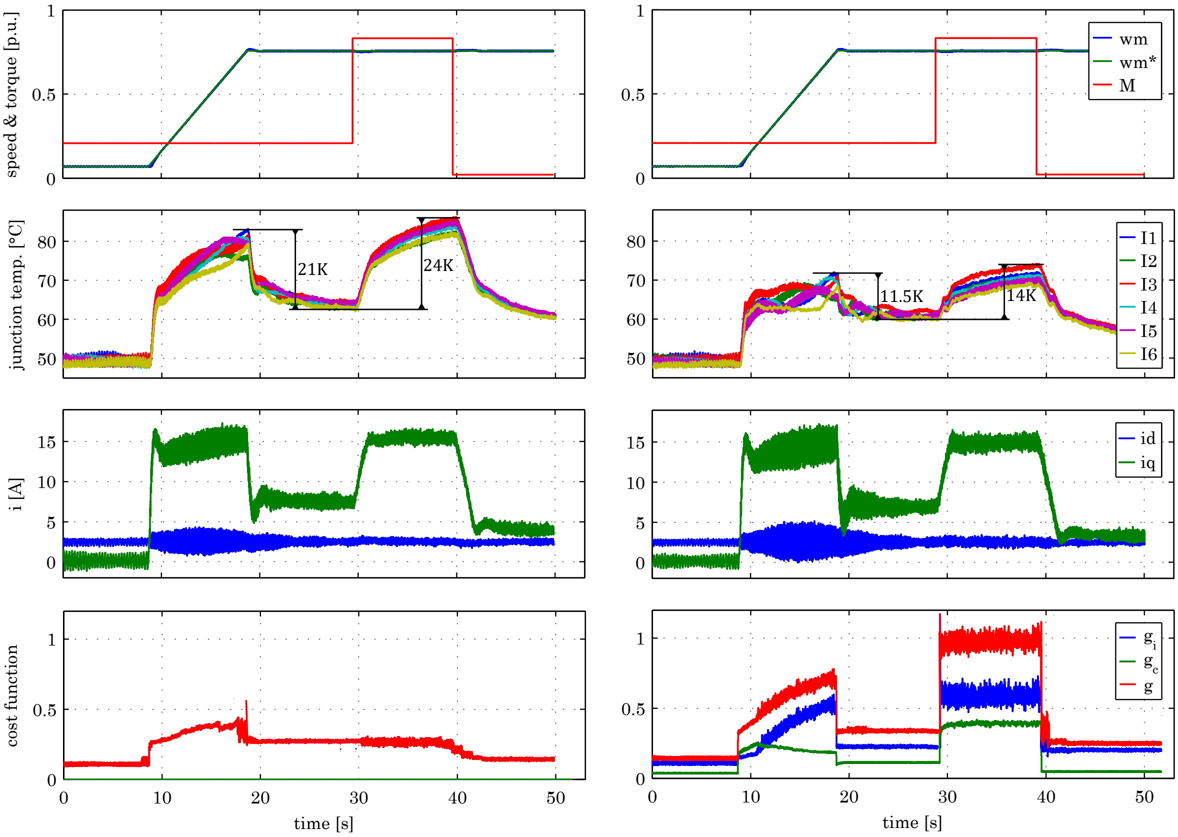

Figure 5.10: Using FCS-MPC to reduce the thermal stress during acceleration and load change of an induction motor. Normal MPC is used on the left, thermal optimized MPC is used on the right. The junction temperature peaks can be reduced while the current ripple increases. In the bottom plots the values of the minimal cost function are given (lowpass filtered for viability $f_c = 100Hz$). In normal FCS-MPC only the current reference error is minimized. The cost function of the proposed FCS-MPC is optimized for minimal current reference error and thermal stress reduction.

The selection of semiconductors that receive a relief of their loading is done online using the temperature equalization element of the FCS-MPC cost function. It is used to divide the thermal stress in order to equal the average temperatures of all semiconductors.

The consequences to the other semiconductors in the module that are not relieved from stress are dependent from the control strategy that is defined by the cost function. In this case, choosing of selected space vectors is penalized. Therefore, these space vectors are avoided which results in a decrease of the average switching frequency. This is analog to well-known switching frequency reduction methods that avoid switching to other space vectors than the adjacent or zero vectors to reduce the number of commutations. If such a method is used, is has to be paused during the stress relieve procedure.

The results for this experiment are given in Figure 5.11. The differences of the IGBT temperatures I1 to I6 are reduced. Due to the changed prioritization of space vectors also the conductivity of the power diodes D1 to D6 is affected which can be seen in the new distribution of the diode temperatures. The drawback of this technique is an increase in the current ripple. As some space vectors are used less frequently, this additional ripple occurs.

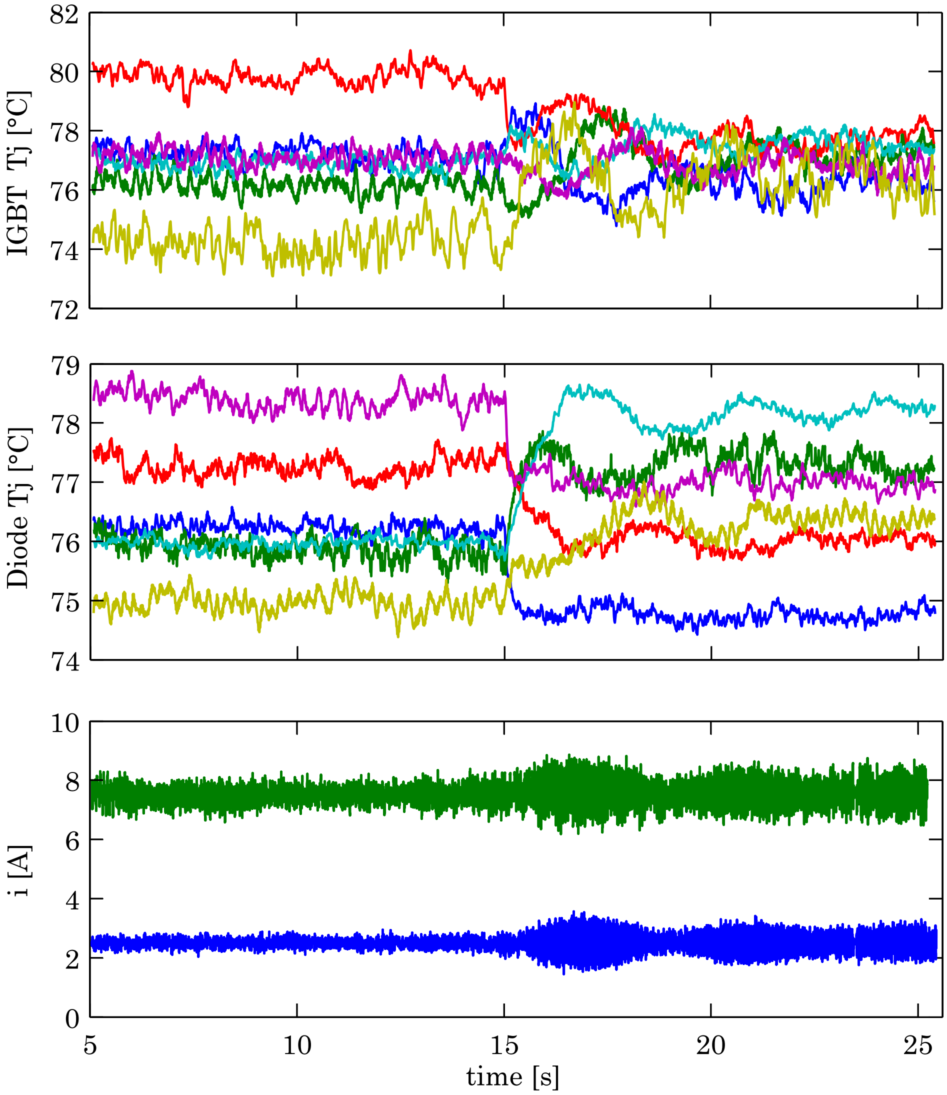

Figure 5.11: Equalization of IGBT junction temperatures in a module. Measured junction temperatures of all six IGBTs and diodes in the module are shown. At $t = 15\,\mathrm{s}$ the control is activated. The λ_{sp}-coefficient can be varied to decide the amount of equalization. Legend is equal to Figure 5.10.

5.7 Conclusion of the chapter

The MPC offers the possibility to include non-linear equations into the control. The FCS-MPC additional offers the possibility to specify the exact switching sequence of the IGBT converter. Both of these properties are well-suited to improve the effectiveness of active thermal control, which is used to reduce the thermal stress in the semiconductor devices. It allows calculating the additional fatigue that an arising thermal cycle adds on each individual chip during inverter operation using a prediction model. This information is considered in the the MPC cost function optimization in order to minimize the thermal stress individually for each chip. Consequently, the FCS-MPC enables to re-distribute the thermal stress in the chips. In the experiment the thermal cycling could be reduced by more than 40 % and the spread between lowest and highest IGBT junction temperature could be reduced from 7 K to 3 K. This is used to equalize the aging of the chips. Considering that the first failed device in a module ends its lifetime, this technique enables to improve the module lifetime. The variation of the cost function element coefficients is an additional degree of freedom in the system design. It allows a trade-off between reducing the thermal stress and additional ripple in current or torque.

The parameter to control the temperatures of the semiconductors in the power module are based on variation of the switching and conduction losses. The thermal stress based FCS-MPC algorithm is able to select the optimal switching sequence that reduces the thermal stress and maintains the desired operation. This requires that the switching sequence with the best possible performance is not necessarily selected. A tolerance band around the performance optimum must be present. Within this tolerance band the optimal switching operation that regards a mixture of performance and thermal stress is selected. However, if only minor tolerance is acceptable only minor influence on the thermal stress occurs.

6. Machine flux variation for ATC

Variation of the machine flux offers a possibility to variate the loading of the converter that is driving the machine without interfering with the mission profile. In this chapter, an active thermal controller is set up that controls the rotor flux of the machine with the aim of smoothing the junction temperatures of the driving inverter. The variation of the flux and its influence on the stator current, input and mechanical power and temperature are analyzed first. A suitable controller is proposed afterwards. Simulation and experimental results are given to demonstrate the concept using the mission profiles of industrial processes and an electric vehicle.

6.1 Rotor flux variation

The usually chosen value of the magnetization flux reference depends on the machine parameters and the desired operation. A high flux level increases the maximum torque of the machine. It is adequate for low-speed high-torque applications. To retain full torque capability over the entire speed range to compensate for load variations the nominal flux level of the machine is selected. For maximum efficient operation the flux reference is varied depending on the load torque. For field-weakening operation the flux reference is usually made proportional to the inverse of the rotor speed [34].

The equations of the rotor flux Ψ_r and the electric torque M_{el} are given in the Laplace domain in equations (6.1) and (6.2) for the general model of the induction machine:

$$\Psi_r(s) = \frac{L_m}{s \cdot \tau_r + 1} \cdot i_{sd}(s) \tag{6.1}$$

$$M_{el}(s) = \frac{m \cdot p \cdot L_m}{2 \cdot L_r} \cdot i_{sq}(s) \tag{6.2}$$

The flux can be controlled with the aim of smoothing the junction temperatures of the driving inverter while maintaining the machine operation. The dependencies between flux, machine current, inverter input power and inverter junction temperatures are shown in Figure 6.1. In this simulation a field oriented control scheme is used. The outer control loop consists of PI controllers for the rotor flux and speed. The inner control loop is done with a FCS MPC for the stator currents. The scheme is given in Figure 2.7 in chapter 2.. The simulated rotational speed and the load torque are kept constant while the flux is stepwise reduced from 1.3 of its nominal value to 0.4 of its nominal value. This is visible in the d-component of the machines stator current. To counteract the reduction of the flux, the necessary torque is increased, therefore, the q-component rises. To counteract a decrease in the d-current a higher increase of the q-current is necessary. The exact ratio depends on the load torque and the gap from the nominal flux. Therefore, the overall current increases, leading to higher losses in the semiconductor devices and increasing junction temperatures. This effect can be used to temporary increase or decrease the junction temperatures by means of active thermal control.

6.2 Active thermal control

In the previous section the effect of varying the rotor flux on the junction temperatures of the driving inverter was shown. In this section the flux of an induction machine is addressed as a parameter for active thermal control. Active thermal control uses temperature related control parameters to influence the junction temperatures of power semiconductor modules online. The goal is to reduce the thermal stress in the module by smoothing the temperature variation. To influence the junction temperatures, the active thermal control increases or decreases the losses in the desired chips temporary. The detailed description of active thermal control is given in section 4.5.

6.2.1 Related work

In [143] a partly similar strategy to reduce the thermal cycling is presented. However, the authors use a permanent magnetized synchronous machine (PMSM) fed by a three level neutral point diode clamped inverter. Their strategy is to preset a reactive current in time intervals of low power in order to reduce the cooling down of the semiconductors in the inverter. The temperature controller estimates a current amplitude that is necessary to compensate the junction temperature drop if there is one in order to increases the conduction losses temporary. The reactive current does not influence the desired mechanical output power of the PMSM. However, it allows to control the temperature of one semiconductor at a time.

The thermal controller is experimentally verified. The results are compared with the conventional maximum torque per ampere (MTPA) and the maximum torque per voltage (MTPV) strategies. In this comparison the semiconductor that takes the highest overall damage was relieved by 30 %. At the same time the power losses in the inverter are increased by 97 % and the power losses in the PMSM are increased by 11 %.

This strategy has in common with the thermal based flux control presented in this chapter that a current is injected to the inverter that does not influence the performance of the driven machine. However, the results are not directly comparable as different machines and inverter topologies are used.

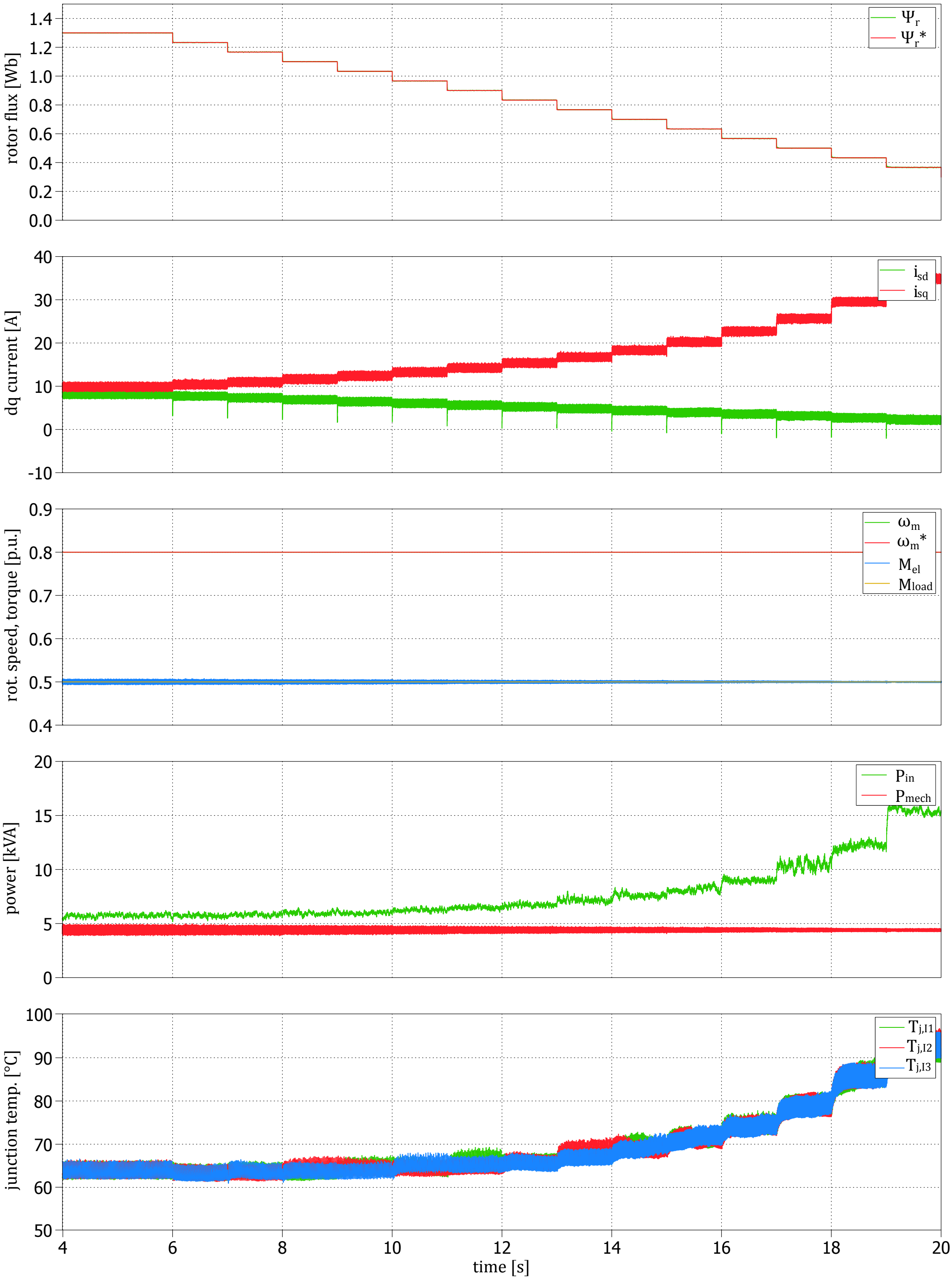

Figure 6.1: Variation of the flux and influence on the stator current, input and mechanical power and temperature of top and bottom IGBTs and power diodes in a 3-phase module from simulation.

6.2.2 Controller Design

In this paragraph a standalone active thermal control that utilizes the rotor flux is build and demonstrated in simulation. It is independent from the thermal based FCS-MPC that was introduced in the previous chapter. This allows to evaluate the pure impact of the variation of the rotor flux on the module's junction temperatures. A combination of both concepts in order to obtain the benefits of both concepts is discussed in the end of this chapter.

To reduce the thermal cycling caused by power variations in the mission profile, a linear open loop controller is built. It applies additional losses in the inverter during low temperature periods of the mission profile to reduce the cooling down of the semiconductors. Its characteristic is given in Figure 6.2. It is designed to decrease the rotor flux when the inverter junction temperatures drop. To the controller this appears as a rising thermal cycling amplitude ΔT_j. To parametrize the characteristic an experiment similar to Figure 6.1 is done. For this simulation the minimum rotor flux is set to $\Psi_{r,min} = 0.5 \cdot \Psi_{r,nom}$ and the maximum rotor flux is set to $\Psi_{r,max} = 1.2 \cdot \Psi_{r,nom}$. $\Psi_{r,nom}$ is the nominal rotor flux. This saturation for the minimum and maximum flux reference ensures to operate the machine only within its specifications. In this range the machine operation is neither too noisy nor close to stalling. The thermal cycling amplitude limits $\Delta T_{j,min}$ and $\Delta T_{j,min}$ are set according to section 4.5.4. The ΔT_j is defined in (4.32). A simple approximation is based on the high dynamic junction temperature estimation T_j and the low dynamic temperature measurement of the module's case T_c as given in (4.33).

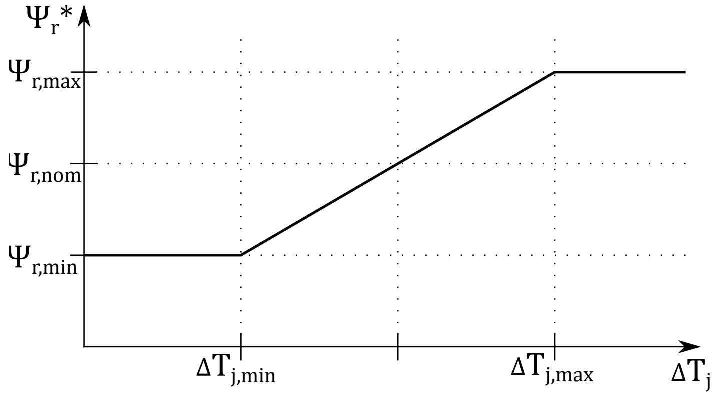

Figure 6.2: Flux junction temperature characteristic. The rotor flux reference Ψ_r^* is a function of the junction temperature amplitude ΔT_j.

The rotor flux reference for the flux controller is taken from the flux temperature characteristic instead of the constant nominal flux. The input to the characteristic is the junction temperature. Therefore, it is estimated using the power loss calculation based junction temperature detection that is given in section 4.2. The machine control scheme of the active thermal control using machine flux variation is given in Figure 6.3.

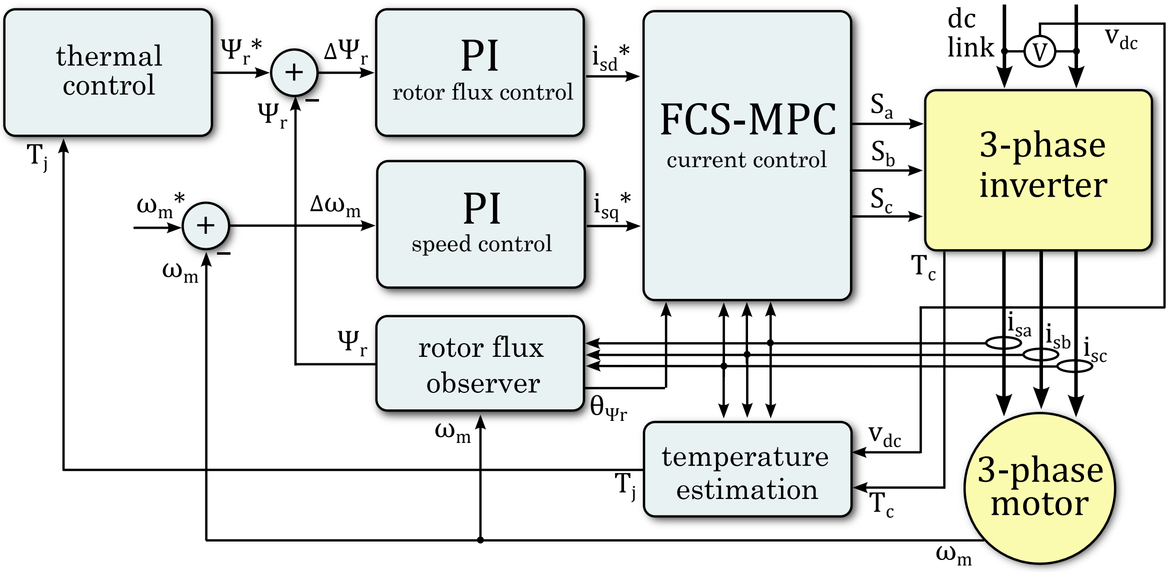

Figure 6.3: Active thermal control using machine flux variation. The outer loop of the machine control is based on the field oriented control.

6.2.3 Simulation Results

To demonstrate the principle of flux variation aiming to smooth the junction temperatures, a simulation is done. The mission profile is a constant speed and a trapezoid load torque, which is plausible for an industrial process. The machine is controlled using the scheme in Figure 2.7. For the simulation, a 5.5 kW squirrel cage induction machine and a 3-phase 1200 V, 25 A power module is considered. The simulation results are given in Figure 6.4. In the conventional controlled simulation, the flux is controlled to hold its nominal value. The input power has the same shape as the torque reference and the junction temperatures follow with a time delay. The thermal cycling amplitude of the topside IGBTs is about 20 K. Using the proposed active thermal control the rotor flux is controlled to reduce the junction temperature swing. This is visible in the stator currents d-component, which is proportional to the rotor flux. When the field is weakened, the speed controller increases the q-current in order to maintain the constant speed reference. This increases the total power during the periods of low power consumption. As a result, the thermal cycling amplitude is reduced to less than 10 K. The drawback is the reduced efficiency as an increased input power is needed to prevent cooling down of the chip temperatures.

Based on the bondwire liftoff and the chip solder degradation failure mechanisms described in section 3.4, the power semiconductors can undergo a specific number of thermal cycles N_f, which is exponentially dependent on the magnitude of the thermal cycles and the base temperature. Lifetime models that can be used to calculate this dependency are described in section 4.3. In this simulation the Bayerer model is applied.

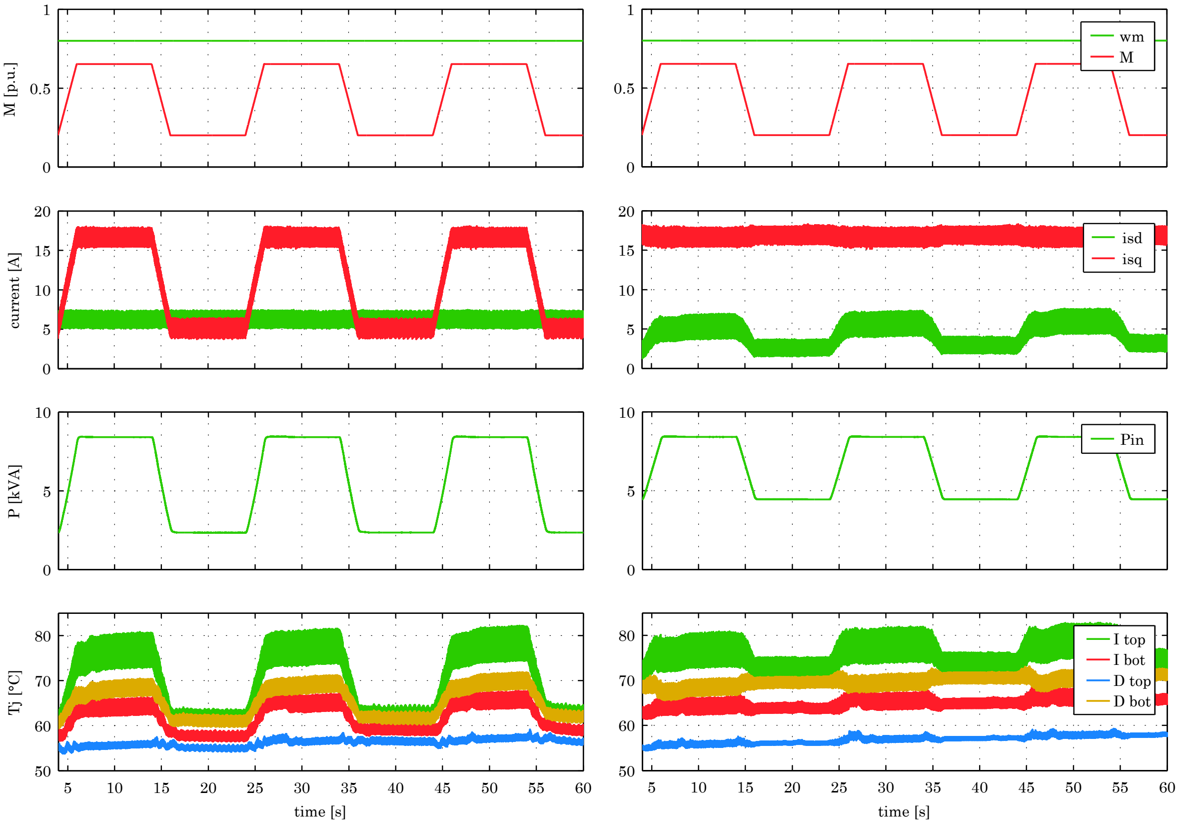

Figure 6.4: Simulation with conventional control (left) and with use of active thermal control flux variation (right).

To trade off the increment in lifetime against the reduction in efficiency, the necessary parameters for both simulations are given in table 6.1. The normalized efficiency is the ratio of the average source power of the conventional controlled run of the mission profile to the average source power of active flux controlled run of the mission profile. The number of cycles to failure is calculated using the Bayerer lifetime model given in section 4.3. It is also normalized to the conventional controlled run of the mission profile.

$$\eta_{conv} = \frac{P_{in,conv}}{P_{in,conv}} = 1 \tag{6.3}$$

$$\eta_{atc} = \frac{P_{in,atc}}{P_{in,conv}} \tag{6.4}$$

$$\tau_{l,conv} = \frac{N_{f,conv}}{N_{f,conv}} = 1 \tag{6.5}$$

$$\tau_{l,atc} = \frac{N_{f,atc}}{N_{f,conv}} \tag{6.6}$$

In these equations η_{conv} is the conventional controlled efficiency and η_{atc} is the efficiency when using the active thermal control. Also, $\tau_{l,conv}$ is the conventional controlled number of cycles to failure and $\tau_{l,atc}$ is the number of cycles to failure when using the active thermal control.

Parameter	**Symbol**	**conventional**	**flux control**
average input power	P_{in}	6.18 kW	7.26 kW
efficiency	η	1 (norm.)	0.851
max. thermal cycling	$\Delta T_{j,max}$	20 K	11 K
cycles to failure	N_f	$5.5 \cdot 10^6$	$7.6 \cdot 10^7$
lifetime improvement	τ_l	1 (norm.)	14

Table 6.1: Simulation evaluation.

The result of this simulation is that an improvement of the lifetime by the factor of 14 costs an efficiency drawback of 0.85. Whether this is meaningful or not depends on the application. However, in this mission profile the time periods for high and low power are balanced. For mission profiles which contain high power operation with only short interrupts, the same lifetime improvement in lifetime can be achieved with less drawback in efficiency.

It is possible to tune the amount of thermal cycling reduction by choosing the minimum flux. At minimum flux the machine is eligible for the desired operation but the losses are increased compared to operation using nominal flux. This effects the ratio of the lifetime improvement versus drawback in efficiency. A series of simulations has been performed using different proportions of the nominal flux for the minimum flux. This is given in Fig. 6.5 for the same mission profile but at a three times higher power level.

In this simulation series the the power level of the mission profile is three times higher. Therefore, the remaining power in the period of reduced power of the mission profile is also higher. The remaining heat loss can be increased to a higher level, when the thermal control multiplies the losses. This results in faster heating of the chips. In addition the minimum flux in this simulation series is $\Psi_{min} = 0.5\,\mathrm{Wb}$.

Using these parameters the maximum lifetime improvement in this simulation series is 27. This maximum value exceeds the typical requirements for higher lifetimes of applications. A realistic choose for the lifetime improvement is a factor between 1.5 and 4. The figure can be used look up the expected efficiency of the system for a given target lifetime improvement. For example if a lifetime improvement of 3 is aimed, the corresponding efficiency is 0.93.

6.2.4 Experimental validation

The experimental validation is done on a three-phase two-level dc/ac inverter. An open module without the use of isolating gel filling is used. This allows direct temperature measurements on the chips but decreases the isolation voltage below the rated values.

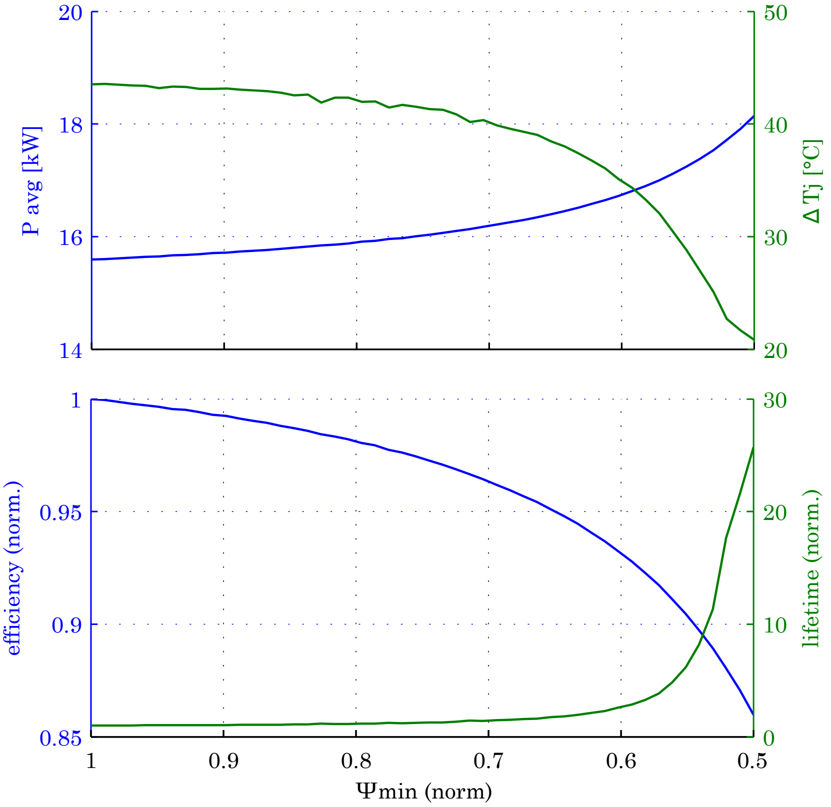

Figure 6.5: Benchmark of the active thermal control. The average input power is drawn against the thermal cycling amplitude occurring in the mission profile. The lifetime improvement versus drawback in efficiency is derived from that.

For junction temperature measurement a high speed infrared camera is used that allows a measurement bandwidth of up to 1 kHz for this purpose. The accuracy is rated 0.02 K. It has been used before to validate an online junction temperature estimation in section 4.2 and will be used to validate the effect of the reduced thermal stress. For power input a 10 kW dc power supply is used. The load is an induction machine connected to a torque machine. The control is implemented on a dSPACE DS1006 processor board. A photograph of the measurement system is given in Figure 11.3 and a photograph of the machine test bench is given in Figure 11.2 in the appendix.

Firstly, an experiment to scale the thermal cycle amplitude during load changes of an induction machine has been done. The infrared camera is used to measure the temperatures of the IGBT chips in the power module. The mission profile consists of rectangular torque changes at fixed rotational speed as it is plausible in industrial processes and conveyors. Two runs of the mission profile are done: One to show the performance and temperatures using conventional control and another to show the same parameters when using the thermal based variation of the rotor flux. The results are given in Figure 6.6. In the conventional control, the flux is controlled to its optimal value. Consequently, the d-component of the current is constant. During the varying of the load torque, the q-component follows the torque, which results in fluctuating power flow through the IGBT module. The junction temperatures of the IGBTs are measured with the infrared camera. For the high-side IGBT of the third phase a maximum thermal cycling amplitude of 25 K is measured. The other IGBT junction temperatures have similar cycling.

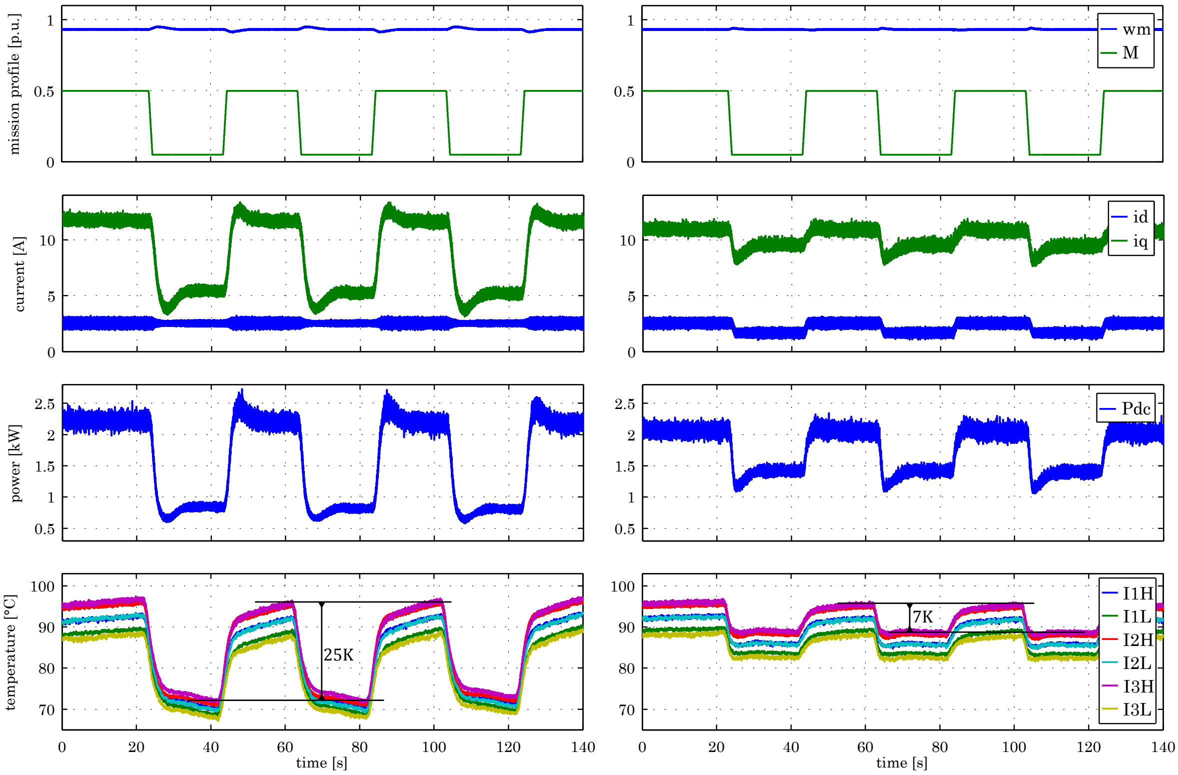

Figure 6.6: Experimental measurement with conventional control (left) and with use of active thermal control flux variation (right). The mission profile of an industrial process is used.

When using the thermal control, the temperature drops are detected using the thermal model. The controller reacts by decreasing the machine rotor flux, which reduces the fluctuation of the q-component of the current. Consequently, the total power fluctuation is reduced, which results in reduces thermal cycling. In fact, the maximum thermal cycling is reduced to 7 K. As additional losses occur, the efficiency of the inverter decreases.

The analysis of the experiment is given in Table 6.2. The experiment is evaluated according to additional lifetime and efficiency reduction. The average power of the whole experiment increases when applying the active thermal control. Consequently, the efficiency decreases. Using the Bayerer lifetime model given in section 4.3 the number of cycles to failure is calculated. The lifetime improvement is derived from N_f and is normalized. The formulas are given in equations (6.3) to (6.6).

The lifetime improvement is higher than in the simulation. This is because of two facts: Firstly, in this experiment the thermal cycling amplitude is reduced to $7[K]$ which is smoother than the simulated value of $11[K]$. Secondly, which is the main fact, the Bayerer lifetime model only considers thermal cycles for the degradation of IGBT

Parameter	**Symbol**	**conventional**	**flux control**
average power	P_{avg}	1.61 kW	1.75 kW
efficiency	η	1 (norm.)	0.917
max. thermal cycling	$\Delta T_{j,max}$	25 K	7 K
cycles to failure	N_f	$1.6 \cdot 10^6$	$3.9 \cdot 10^8$
lifetime improvement	τ_l	1 (norm.)	243.8

Table 6.2: Experimental evaluation (trapezoid profile).

modules. If the model receives a constant junction temperature input, no cycles occur and the number of cycles to failure is infinity. Therefore, for small thermal cycles large numbers of cycles to failure occur.

Another experiment is done using a mission profile of a suburban drive of a medium sized car (TRL WSL Suburban) according to the Warren Spring Laboratory, which are routinely used for emission tests of the Transport Research Laboratory, England. The results are given in Figure 6.7.

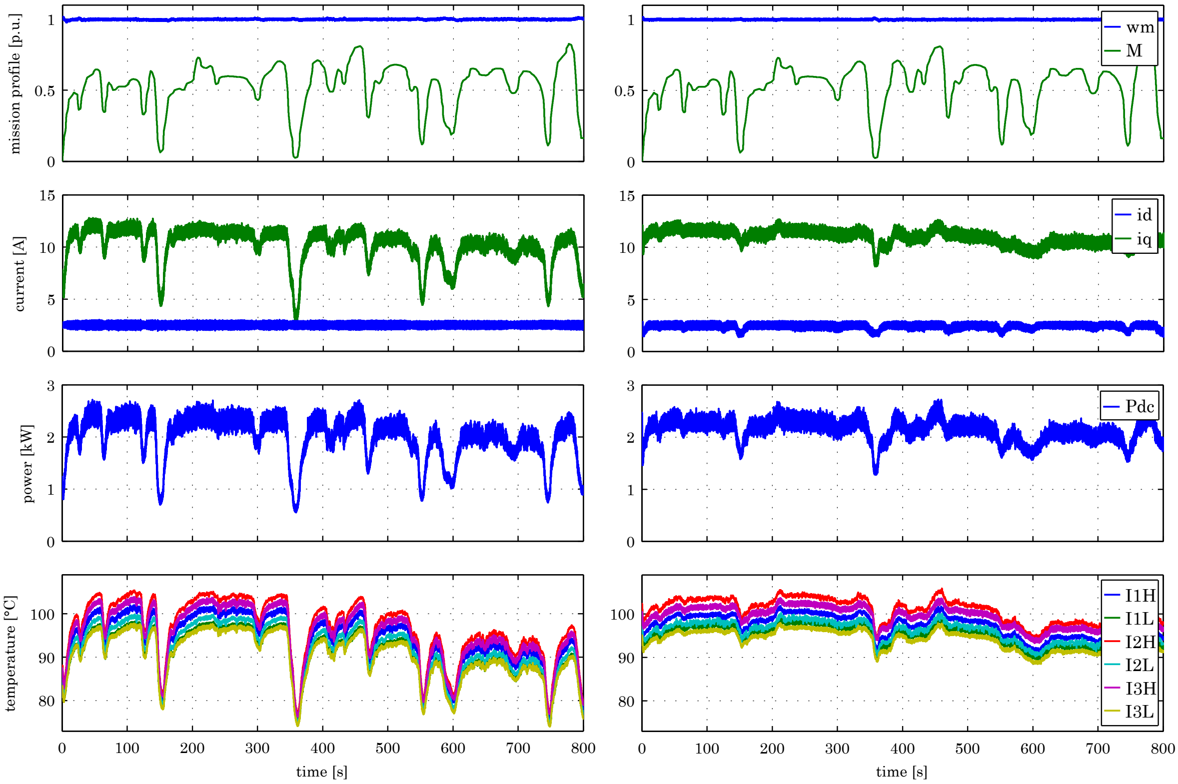

Figure 6.7: Experimental measurement with conventional control (left) and with use of active thermal control flux variation (right). The mission profile of a suburban drive of a car is used.

The motor rotational speed is kept constant, whereas the load torque is varied according to the TRL WSL mission profile. In the conventional controlled run the junction temperatures of all chips in the module fluctuate with the profile. The active thermal control is used to smooth the junction temperatures by variation of the rotor flux. This is visible in the d-component of the load current. To analyze the thermal cycles that occur in the mission profiles, the rainflow counting algorithm is used. This is given in Figure 6.8.

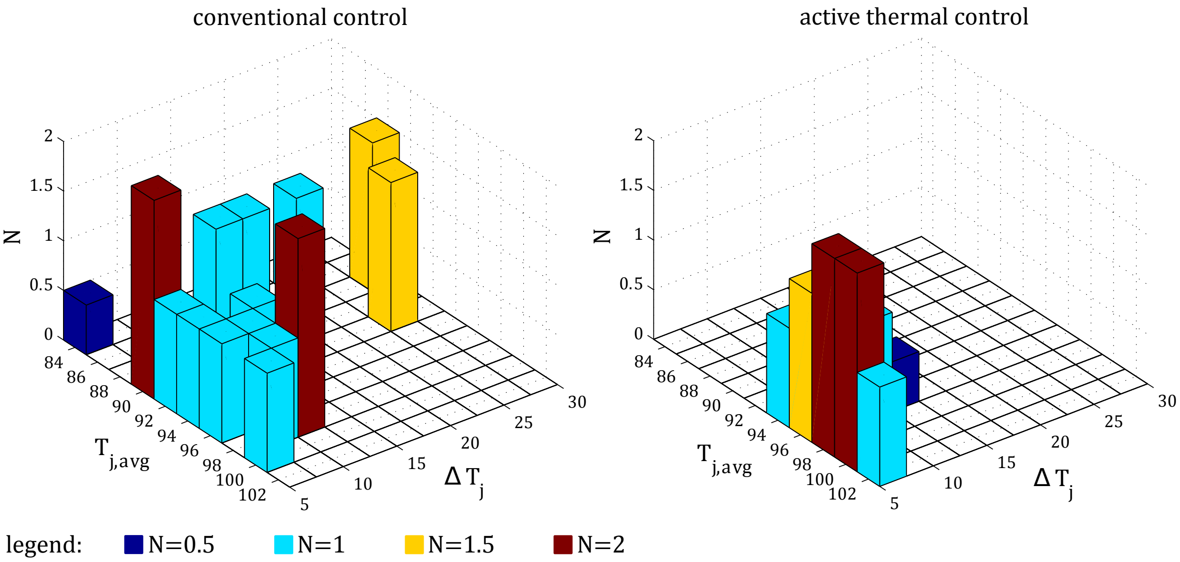

Figure 6.8: Analysis of the thermal cycling occurring in Fig. 6.7 using the rainflow counting algorithm.

When conventional controlled, several thermal cycles with amplitudes up to $\Delta T_j = 30\,\mathrm{K}$ occur. Thermal cycles smaller than $5\,\mathrm{K}$ are neglected in the figure as they have only minor influence on the device's lifetime. The analysis of the active thermal controlled run shows, that larger thermal cycles have been reduces to minor ones. Minor thermal cycles vanish below the $5\,\mathrm{K}$ threshold. The average temperature of the thermal cycles increases slightly.

The experiment is evaluated in Table 6.3 towards efficiency and lifetime. For the cumulative damage analysis, Miner's rule given in equation (4.30) is applied for each thermal cycle in the profile.

Parameter	**Symbol**	**conventional**	**flux control**
average power	P_{avg}	$1.97\,\mathrm{kW}$	$2.12\,\mathrm{kW}$
efficiency	η	1 (norm.)	0.929
cumulative damage	c	$1.8 \cdot 10^{-}6$	$2.4 \cdot 10^{-}8$
lifetime improvement	τ_l	1 (norm.)	75.7

Table 6.3: Experimental evaluation (car profile).

The formulas for η and τ_l are given in equations (6.3) to (6.6).

Another experiment is done with a rolling mill mission profile. A material like steel is rolled several times until the final material thickness is reached. The electric machine torque increases for rolling iterations with increased pressure. Between the rolling iterations the torque decreases close to zero. This evokes thermal cycles in the machine power semiconductor module. In the experiment a recording of the torque of a real rolling mill is taken and given as a reference to the torque machine of the experimental setup. A reference run without active thermal control is shown in Figure 6.9. The experiment that uses active thermal control by flux variation is given in Figure 6.10.

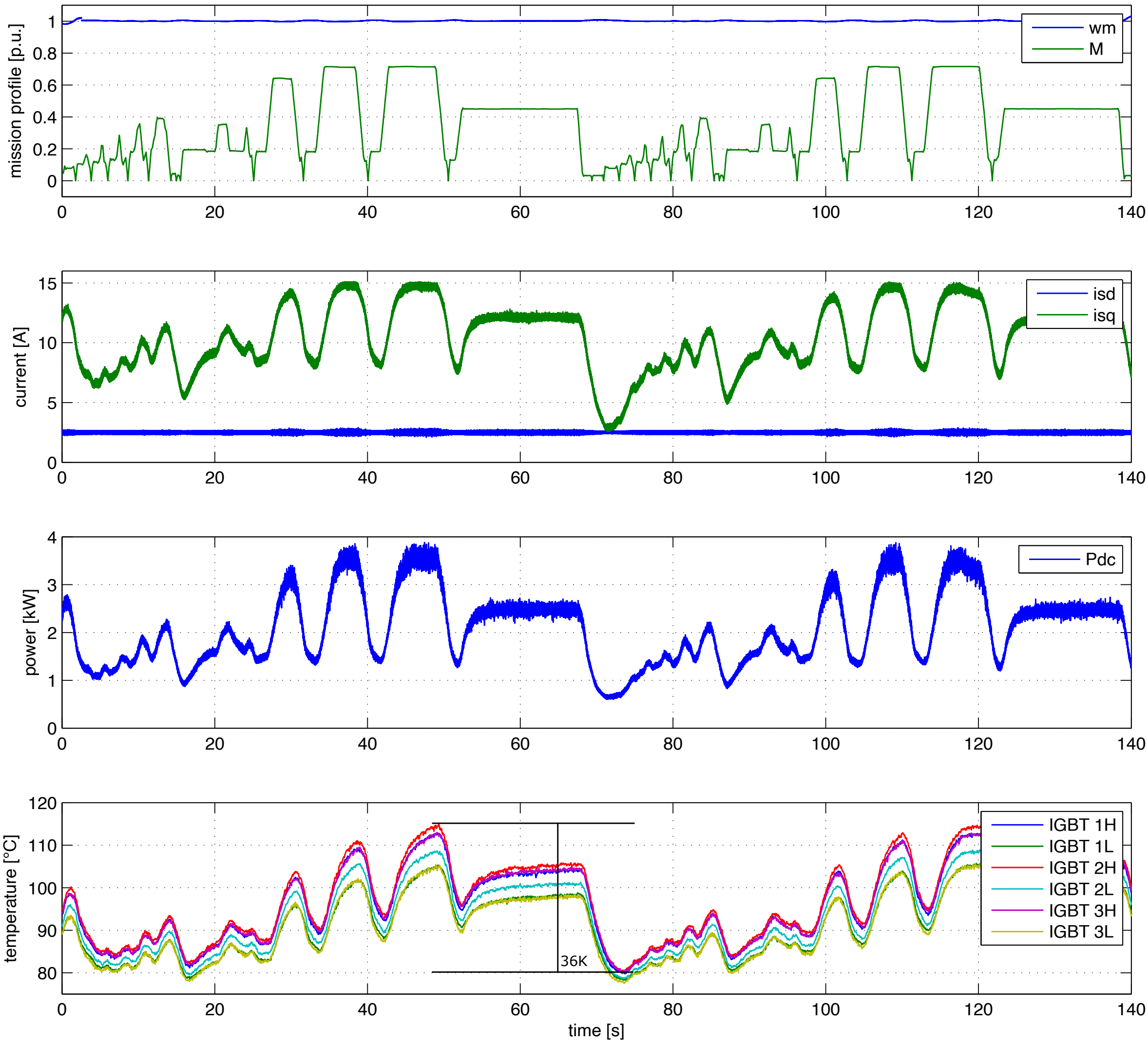

Figure 6.9: Experiment to reduce the stress in the inverter driving an induction machine in a rolling mill mission profile. This is the run without use of the active thermal control for reference.

At the marked position the thermal cycling is reduced from 36 K to 18 K which is a bisection of the thermal cycling amplitude in the mission profile. The spread of the IGBT temperatures, this means the difference between the highest and the lowest IGBT temperature in the module, is not reduced with the active thermal control. This means the fatigue of the IGBTs happens with different ratios. This cannot be prevented with the active thermal control by means of flux variation, as the controller structure only allows to influence the temperatures of all semiconductors in the IGBT module together. A modification that allows also influence on the temperature of individual semiconductors is discussed next.

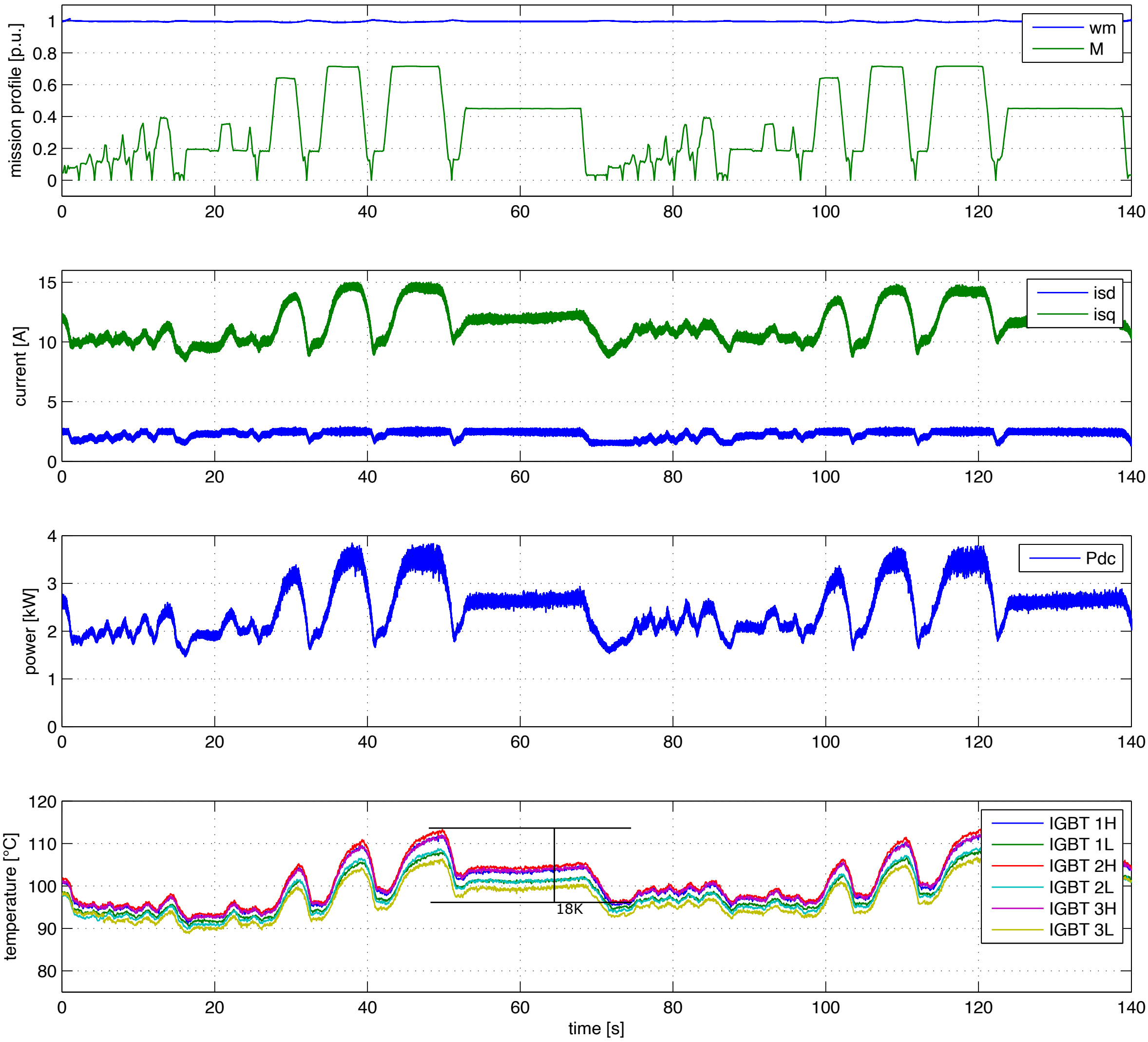

Figure 6.10: Experiment to reduce the stress in the inverter driving an induction machine in a rolling mill mission profile. In this run the active thermal control by means of rotor flux variation is used to reduce the thermal stress.

6.3 Combination with thermal based FCS-MPC

The concept of thermal control by variation of the rotor flux has been demonstrated using the standalone thermal control in this section. In the next step it is included into the thermal based FCS-MPC that was presented in the previous chapter in order to combine its benefits: The thermal-based FCS-MPC allows to control every semiconductor in the module separately and including of non-linear thermal and lifetime related models into the control law. The thermal control by variation of the rotor flux allows to rise the junction temperatures of all semiconductors in the module by more than 15 K in the experimental validations. The aim of the combination of both concepts is to control each semiconductor individual and enlarge the maximum size of thermal cycling amplitude that can be compensated compared to the previously demonstrated thermal-based FCS-MPC in chapter 5.

To reach the goal the strengths of both controllers are combined: The rotor flux variation is used to compensate that part of a thermal cycle amplitude that evokes in all semiconductors in the module. This portion of the thermal cycling amplitude will be called the base thermal cycle amplitude. The thermal-based FCS-MPC algorithm is used to compensate the remaining individual semiconductor thermal cycling amplitude which will be called individual thermal cycling amplitude. This is demonstrated in Figure 6.11.

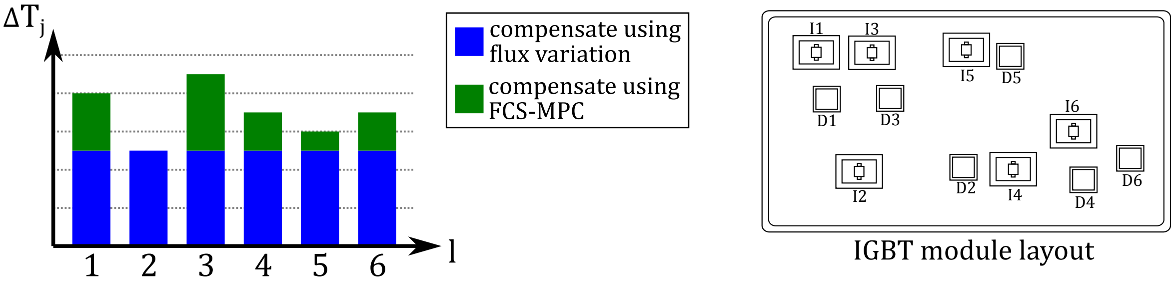

Figure 6.11: This Figure shows the partition in the base thermal cycling amplitude that applies for all semiconductors and the individual thermal cycling amplitude which is the difference of an individual semiconductor thermal cycling amplitude to the base thermal cycling amplitude. On the right is a possible layout of an IGBT module.

Within an IGBT module the thermal cycling amplitudes of the semiconductors spread. A reason is unequal dissipation of the heat that arises in the chips. A possible layout of the IGBTs and power diodes in an power electronics module is given in the right part of Figure 6.11. In this example the IGBTs I1 and I3 are located close to each other in the upper left corner of the module. The power density in this part of the module substrate is higher than for example the power density in the lower left corner where only IGBT I2 are located. Consequently, I1 and I3 have a higher average temperature compared to I2 at the condition that all IGBTs have equal degradation and the cooling of the substrate is homogenous. This is visibe in the left part of the figure for IGBTs $l = /1, 2, 3/$ which correspond I1, I2 and I3.

The base thermal cycling amplitude $\Delta T_{j,base}$ and the individual thermal cycling amplitude $\Delta T_{j,ind}$ are defined in the following two equations:

$$\Delta T_{j,base} = \min\left(\Delta T_{j,l}\right) \cdot r_t \tag{6.7}$$

$$\Delta T_{j,ind}(l) = \Delta T_{j,l} - \Delta T_{j,base} \tag{6.8}$$

The parameter r_t is a tuning parameter that selects which amount of the base thermal cycling amplitude is compensated by the rotor flux variation. Values can be chosen $0 \leq r_t \leq 1$. Zero means no part of the thermal cycling amplitude is compensated by the rotor flux variation. In this configuration the controller works exactly like demonstrated in chapter 5.. One means the complete mutual amount the thermal cycling amplitudes of the semiconductors in the module is compensated by the rotor flux variation. Interim values help if the aim of the active thermal control is only a reduction of the thermal cycling and not a maximum compensation.

6.3.1 Controller Design

The scheme of the controller is based on the thermal based FCS-MPC that is described in Figure 5.4 of chapter 5.. However, it is extended by the calculation of the base thermal cycling amplitude and the individual thermal cycling amplitude according to equations (6.7) and (6.8). $T_{j,base}$ used to compute the flux reference of the machine according to the flux characteristic that is given in Figure 6.2. $T_{j,ind}$ is used to run through the thermal-based FCS-MPC algorithm given in Figure 5.4. This method is shown in Figure 6.12.

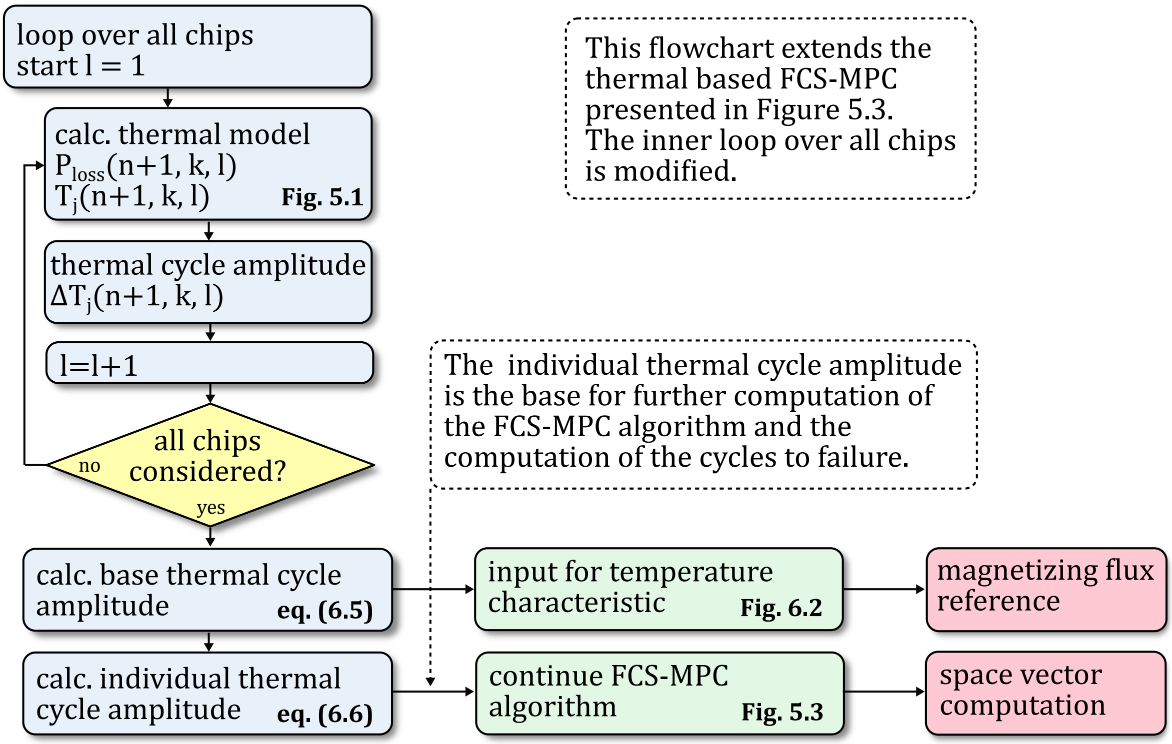

Figure 6.12: To include the flux variation in the thermal based FCS-MPC, the calculation of the base thermal cycling amplitude and the individual thermal cycling amplitude is included in the algorithm.

The base thermal cycling amplitude is compensated by the flux control. Thus, only the individual thermal cycling amplitude needs to be compensated by the thermal based FCS-MPC. To prevent both thermal controllers from working against each other it is necessary that the flux controller is slower than the thermal-based FCS-MPC. This is ensured with a change rate limitation of the rotor flux reference.

6.4 Conclusion of the chapter

The influence of rotor flux variation on the stator current, input power and temperature of semiconductors in a three-phase module is demonstrated. On this basis an active thermal controller was designed to reduce the thermal cycling in the power module of the inverter.

Simulation and experiment at different power levels and mission profiles have been carried out. In the experiment the thermal cycling amplitude of an industrial process mission profile could be reduced from 25 K to 7 K. This results in a lifetime increment of more than 200. Another experiment for an electric vehicle has been carried out resulting in a lifetime increment of more than 75. The main drawback of this technique is the increased losses. However, the amount of lifetime increment versus drawback in efficiency can be selected freely as a tuning parameter of the active thermal control.

The combination of the rotor flux variation and the thermal based FCS-MPC is a possibility to control each semiconductor individual and enlarge the maximum size of thermal cycling amplitude that can be compensated.

7. Summary, Conclusion and Future Research

The purpose of this chapter is to summarize the results, which have been achieved throughout this thesis. Finally, topics for the future work are also discussed.

7.1 Summary and conclusion

Thermal cycling is one of the main sources of aging and failure in power electronics. A possibility to reduce the thermal stress of semiconductors is to control the distribution of losses occurring in the semiconductor devices and reduce the thermal cycles in the most stressed. This approach is known as active thermal control.

The hardest limit of known active thermal control approaches is that they cannot set the optimal switching operation that fulfils the applications demand, reduces the thermal stress in a specific semiconductor and limit the additional occurring losses. A second limitation is found in inaccuracies of the high-bandwidth junction temperature measurement that is needed for proper control. Also aging and lifetime consumption of the module is not yet taken into account in a systematic way. More open topics in research are found in giving design guidelines for temperature control and providing a universal approach that is not restricted to a specific technology.

This research aimed to overcome these limitations and prepare to widen the use of thermal control in power electronic applications. The goal was to achieve the minimum thermal stress for the best possible overall efficiency. For this purpose finite control-set model predictive control (FCS-MPC) seemed the optimal approach because it allows including of non-linear thermal and lifetime related models into the control law. A precise control of the thermal stress in the semiconductors was achieved as the optimal switching vector is directly applied to the physical system.

In chapter 2 the finite control-set model predictive control is introduced. It starts with the general principle of model predictive control. For power electronics the variant of the FCS-MPC is introduced in detail. State of the art and theoretical background of the control structure are given for the application of control of electric drives. This includes a view on direct torque control which is related to the FCS-MPC.

In chapter 3 starts with the results of comprehensive industry-wide survey that was conducted with collaboration of the international organization European Center for Power Electronics (ECPE). The survey was circulated to the selected reliability experts from ECPE member companies. Typical target lifetimes of 5 to 20 years were identified for the application field of electric drives. The investigation on stressors that limit these requirements showed that all thermal stressors were considered particularly critical with power cycling identified as the most critical stressor. Along the same lines, semiconductor devices were identified the most critical components. Potential is seen in active methods that help to increase the reliability during operation. On the basis of this survey and literature research the current state of reliability in power electronics is described.

Chapter 4 deals with methods to improve the reliability in power electronic modules. This includes auxiliary methods that are necessary to obtain the the junction temperatures of a power electronic module. A junction temperature estimator was designed that fulfills the demand in accuracy, computation time and bandwidth. It is tested by parallel use of a high-bandwidth infrared camera on an opened IGBT module during operation. Methods for condition monitoring are reviewed. The thermal cycling of the semiconductors can be smoothed during operation using active thermal control. The overall goal is reducing the thermal stress to increase lifetime of the semiconductors. In experiments with realistic mission profiles a reduction of the thermal cycling amplitude could be achieved. This shows that active thermal control for power modules can potentially extend the lifetime of the converter.

In chapter 5 the FCS-MPC is applied to reduce the thermal stress of power electronic modules. An online lifetime model based on known cycles to failure models is designed to regard the impact of aging of the module. It is used to provide information on the damage of the module during operation and to predict the damage that future switching operations will create. This information was included into the active thermal control law and used to update the parameters of the power electronic system that are affected by the aging. The purpose of the algorithm is to keep the fatigue of the module low by reducing the thermal stress. In contrast to other active thermal control studies, it also allows to equalize the junction temperatures in the power module. The power losses are changed according to the stress that results from thermal cycles.

In chapter 6 the rotor flux of an induction machine is used as a parameter for active thermal control of power modules in drives applications. The method is described in theory and proven in simulation and experiment. For realistic mission profiles a reduction of the thermal cycling amplitude could be achieved. In the next step the flux variation is integrated into the thermal-based FCS-MPC of the previous chapter. As a result the maximum amplitude of thermal cycles that can be compensated is increased. This allows to reduce the thermal stress in application with severe thermal cycles.

7.2 Future research

This thesis has introduced control algorithms for controlling the thermal stress in power semiconductor modules. Chapter 3 pointed out that there are other components in the converter which are prone to failures. These components include capacitors, semiconductor drivers, control system hardware, sensors and axillary power supply systems. To increase the lifetime of the whole system, it needs to be ensured that not only the power semiconductor modules are kept operational, but also the other components and subsystems. This can be addressed with the development of proper lifetime models for all components, which need to be included in a comprehensive approach.

For manufacturers and operators of power electronic modules it is of interest to estimate the impact of certain usage on the lifetime of modules. The lifetime of a system is an important parameter, as cost calculations for purchase, maintenance and replacement depend on it. The aim of lifetime prediction is to assess over which time interval a module can be used without failures for a particular application.

The estimation of the remaining lifetime that is used in the thermal-based FCS-MPC is based on the LESIT model. Other lifetime models from literature have been reviewed that are also based on the LESIT model. When a reduction of the thermal cycling is achieved, this model is referred to tell that the lifetime of the IGBT module has increased.

However, a direct experiment to increase the lifetime of a power semiconductor module using the active thermal control has not been performed. A possibility is to perform accelerated lifetime testing of IGBT modules based on thermal cycling and comparison with still used LESIT model. A longtime test with setups that use active thermal control and conventional setups for reference can prove the effectiveness of active thermal control and excludes possible not seen negative effects of active thermal control.

Furthermore, future work is required to collect data in combination with accelerated aging tests under different load operating conditions to improve the robustness of the available lifetime models. A lifetime model can provide information on the consumed lifetime of a module during operation. The lifetime model can be used to update the thermal impedances of the thermal network according to the aging. This improves the junction temperature estimation in aged modules.

8. Bibliography

[1] H. Wang, M. Liserre, and F. Blaabjerg, "Toward reliable power electronics: Challenges, design tools, and opportunities," *IEEE Industrial Electronics Magazine*, vol. 7, no. 2, pp. 17–26, June 2013.

[2] D. Murdock, J. Torres, J. Connors, and R. Lorenz, "Active thermal control of power electronic modules," *IEEE Transactions on Industry Applications*, vol. 42, no. 2, pp. 552–558, March 2006.

[3] M. Andresen, K. Ma, G. Buticchi, J. Falck, F. Blaabjerg, and M. Liserre, "Junction temperature control for more reliable power electronics," *IEEE Transactions on Power Electronics*, vol. 33, no. 1, pp. 765–776, Jan 2018.

[4] S. Kouro, M. Perez, J. Rodriguez, A. Llor, and H. Young, "Model predictive control: Mpc's role in the evolution of power electronics," *IEEE Industrial Electronics Magazine*, vol. 9, no. 4, pp. 8–21, Dec 2015.

[5] J. C. R. Martinez, R. M. Kennel, and T. Geyer, "Model predictive direct current control," in *2010 IEEE International Conference on Industrial Technology*, March 2010, pp. 1808–1813.

[6] W. S. Levine, *The control handbook.* CRC press, 1996.

[7] R. M. Kennel, M. Kazmierkowski, J. Rodriguez, and P. Cortes, "Predictive control in power electronics and drives," in *2008 IEEE International Symposium on Industrial Electronics*, June 2008, pp. 1–90.

[8] S. Saeidi and R. Kennel, "Continuous set nonlinear model predictive control for an induction motor," in *2013 15th European Conference on Power Electronics and Applications (EPE)*, Sept 2013, pp. 1–10.

[9] J. Holtz and S. Stadtfeld, "A predictive controller for the stator current vector of ac machines fed from a switched voltage source," in *Proc. of JIEE IPEC-Tokyo Conference*, 1983, pp. 1665–1675.

[10] J. Holtz, "Pulsewidth modulation for electronic power conversion," *Proceedings of the IEEE*, vol. 82, no. 8, pp. 1194–1214, Aug 1994.

[11] J. Rodriguez and P. Cortes, *Predictive control of power converters and electrical drives.* John Wiley & Sons, 2012, vol. 40.

[12] J. Rodriguez, M. Kazmierkowski, J. Espinoza, P. Zanchetta, H. Abu-Rub, H. Young, and C. Rojas, "State of the art of finite control set model predictive control in power electronics," *IEEE Transactions on Industrial Informatics*, vol. 9, no. 2, pp. 1003–1016, May 2013.

[13] M. Preindl, E. Schaltz, and P. Thogersen, “Switching frequency reduction using model predictive direct current control for high-power voltage source inverters,” *IEEE Transactions on Industrial Electronics*, vol. 58, no. 7, pp. 2826–2835, July 2011.

[14] E. F. Camacho and C. B. Alba, *Model predictive control.* Springer Science Business Media, 2013.

[15] L. Wang, *Model predictive control system design and implementation using MATLAB.* Springer Science & Business Media, 2009.

[16] P. Cortes, M. P. Kazmierkowski, R. M. Kennel, D. E. Quevedo, and J. Rodriguez, “Predictive control in power electronics and drives,” *IEEE Transactions on Industrial Electronics*, vol. 55, no. 12, pp. 4312–4324, Dec 2008.

[17] R. Vargas, P. Cortes, U. Ammann, J. Rodriguez, and J. Pontt, “Predictive control of a three-phase neutral-point-clamped inverter,” *IEEE Transactions on Industrial Electronics*, vol. 54, no. 5, pp. 2697–2705, Oct 2007.

[18] H. Abu-Rub, J. Guzinski, Z. Krzeminski, and H. A. Toliyat, “Predictive current control of voltage-source inverters,” *IEEE Transactions on Industrial Electronics*, vol. 51, no. 3, pp. 585–593, June 2004.

[19] A. V. Aho and J. D. Ullman, *Data structures and algorithms.* Pearson, 1983.

[20] J. Scoltock, T. Geyer, and U. K. Madawala, “A model predictive direct current control strategy with predictive references for mv grid-connected converters with *lcl*-filters,” *IEEE Transactions on Power Electronics*, vol. 30, no. 10, pp. 5926–5937, Oct 2015.

[21] P. Karamanakos, K. Pavlou, and S. Manias, “An enumeration-based model predictive control strategy for the cascaded h-bridge multilevel rectifier,” *IEEE Transactions on Industrial Electronics*, vol. 61, no. 7, pp. 3480–3489, July 2014.

[22] J. Scoltock, T. Geyer, and U. K. Madawala, “A comparison of model predictive control schemes for mv induction motor drives,” *IEEE Transactions on Industrial Informatics*, vol. 9, no. 2, pp. 909–919, May 2013.

[23] K. H. Ahmed, A. M. Massoud, S. J. Finney, and B. W. Williams, “A modified stationary reference frame-based predictive current control with zero steady-state error for lcl coupled inverter-based distributed generation systems,” *IEEE Transactions on Industrial Electronics*, vol. 58, no. 4, pp. 1359–1370, April 2011.

[24] S. Kwak and J. C. Park, “Switching strategy based on model predictive control of vsi to obtain high efficiency and balanced loss distribution,” *IEEE Transactions on Power Electronics*, vol. 29, no. 9, pp. 4551–4567, Sept 2014.

[25] J. Holtz and N. Oikonomou, “Fast dynamic control of medium voltage drives operating at very low switching frequency - an overview,” *IEEE Transactions on Industrial Electronics*, vol. 55, no. 3, pp. 1005–1013, Mar. 2008.

[26] M. Kazmierkowski and L. Malesani, “Current control techniques for three-phase voltage-source pwm converters: A survey,” *IEEE Transactions on Industrial Electronics*, vol. 45, no. 5, 1998.

[27] M. Liserre, F. Blaabjerg, and S. Hansen, “Design and control of an lcl-filter-based three-phase active rectifier,” *IEEE Transactions on Industry Applications*, vol. 41, no. 5, pp. 1281–1291, Sep. 2005.

[28] J. Dannehl, C. Wessels, and F. Fuchs, “Limitations of voltage-oriented pi current control of grid-connected pwm rectifiers with lcl filters,” *IEEE Transactions on Industrial Electronics*, vol. 56, no. 2, pp. 380–388, Feb. 2009.

[29] S. Bowes and D. Holliday, “Optimal regular-sampled pwm inverter control techniques,” *IEEE Transactions on Industrial Electronics*, vol. 54, no. 3, pp. 1547–1559, Jun. 2007.

[30] G. S. Buja, “Optimum output waveforms in pwm inverters,” *IEEE Transactions on Industry Applications*, vol. 16, no. 6, pp. 830–836, Nov. 1980.

[31] T. Geyer, “A comparison of control and modulation schemes for medium-voltage drives: Emerging predictive control concepts versus field oriented control,” in *IEEE Energy Conversion Congress and Exposition (ECCE)*, Sep. 2010, pp. 2836–2843.

[32] M. P. Kazmierkowski, R. Krishnan, and F. Blaabjerg, *Control in power electronics: selected problems.* Academic press, 2002.

[33] W. Leonhard, *Control of electrical drives.* Springer Science & Business Media, 2012.

[34] X. Xu and D. W. Novotny, “Selection of the flux reference for induction machine drives in the field weakening region,” *IEEE Transactions on Industry Applications*, vol. 28, no. 6, pp. 1353–1358, Nov 1992.

[35] R. Kennel and A. Linder, “Predictive control of inverter supplied electrical drives,” in *Proc. of 2000 31st Annual IEEE Power Electronics Specialists Conference*, vol. 2, 2000, pp. 761–766 vol.2.

[36] A. Linder and R. Kennel, “Model predictive control for electrical drives,” in *2005 IEEE 36th Power Electronics Specialists Conference*, June 2005, pp. 1793–1799.

[37] S. S. Yeoh, T. Yang, L. Tarisciotti, C. I. Hill, S. Bozhko, and P. Zanchetta, “Permanent-magnet machine-based starter–generator system with modulated model predictive control,” *IEEE Transactions on Transportation Electrification*, vol. 3, no. 4, pp. 878–890, Dec 2017.

[38] Y. Liu, S. Cheng, B. Ning, and Y. Li, “Robust model predictive control with simplified repetitive control for electrical machine drives,” *IEEE Transactions on Power Electronics*, vol. 34, no. 5, pp. 4524–4535, May 2019.

[39] A. A. Ahmed, B. K. Koh, and Y. I. Lee, “A comparison of finite control set and continuous control set model predictive control schemes for speed control of induction motors,” *IEEE Transactions on Industrial Informatics*, vol. 14, no. 4, pp. 1334–1346, April 2018.

[40] I. Takahashi and T. Noguchi, “A new quick-response and high-efficiency control strategy of an induction motor,” *IEEE Transactions on Industry Applications*, vol. IA-22, no. 5, pp. 820–827, Sept 1986.

[41] G. Buja, D. Casadei, and G. Serra, “Dtc-based strategies for induction motor drives,” in *Industrial Electronics, Control and Instrumentation, 1997. IECON 97. 23rd International Conference on*, vol. 4, Nov 1997, pp. 1506–1516 vol.4.

[42] I. Boldea and S. A. Nasar, *Vector control of AC drives.* CRC press, 1992.

[43] Y. Zhang and J. Zhu, “Direct torque control of permanent magnet synchronous motor with reduced torque ripple and commutation frequency,” *IEEE Transactions on Power Electronics*, vol. 26, no. 1, pp. 235–248, Jan 2011.

[44] Y. Zhang and H. Yang, “Generalized two-vector-based model-predictive torque control of induction motor drives,” *IEEE Transactions on Power Electronics*, vol. 30, no. 7, pp. 3818–3829, July 2015.

[45] W. Xie, X. Wang, F. Wang, W. Xu, R. M. Kennel, D. Gerling, and R. D. Lorenz, “Finite-control-set model predictive torque control with a deadbeat solution for pmsm drives,” *IEEE Transactions on Industrial Electronics*, vol. 62, no. 9, pp. 5402–5410, Sep. 2015.

[46] J. Liu, C. Gong, Z. Han, and H. Yu, “Ipmsm model predictive control in flux-weakening operation using an improved algorithm,” *IEEE Transactions on Industrial Electronics*, vol. 65, no. 12, pp. 9378–9387, Dec 2018.

[47] G. Papafotiou, J. Kley, K. G. Papadopoulos, P. Bohren, and M. Morari, “Model predictive direct torque control part ii: Implementation and experimental evaluation,” *IEEE Transactions on Industrial Electronics*, vol. 56, no. 6, pp. 1906–1915, June 2009.

[48] P. D. O'Connor, P. O'Connor, and A. Kleyner, *Practical reliability engineering.* John Wiley & Sons, 2012.

[49] F. Blaabjerg and K. Ma, "Future on power electronics for wind turbine systems," *IEEE Journal of Emerging and Selected Topics in Power Electronics*, vol. 1, no. 3, pp. 139–152, Sept 2013.

[50] J. G. Kassakian and T. M. Jahns, "Evolving and emerging applications of power electronics in systems," *IEEE Journal of Emerging and Selected Topics in Power Electronics*, vol. 1, no. 2, pp. 47–58, June 2013.

[51] N. Baker, M. Liserre, L. Dupont, and Y. Avenas, "Improved reliability of power modules: A review of online junction temperature measurement methods," *IEEE Industrial Electronics Magazine*, vol. 8, no. 3, pp. 17–27, Sept 2014.

[52] A. Graves, K. Harman, M. Wilkinson, and R. Walker, "Understanding availability trends of operating wind farms," in *AWEA Wind Power Conference, AWEA*, 2008.

[53] P. Tavner, F. Spinato, G. Van Bussel, and E. Koutoulakos, "Reliability of different wind turbine concepts with relevance to offshore application," in *Proceedings of European Wind Energy Conference, Brussels, Belgium, March*, 2008.

[54] J. Ribrant and L. Bertling, "Survey of failures in wind power systems with focus on swedish wind power plants during 1997-2005," in *Power Engineering Society General Meeting, 2007. IEEE.* IEEE, 2007, pp. 1–8.

[55] F. Spinato, P. J. Tavner, G. J. Van Bussel, and E. Koutoulakos, "Reliability of wind turbine subassemblies," *IET Renewable Power Generation*, vol. 3, no. 4, pp. 387–401, 2009.

[56] M. Wilkinson, K. Harman, B. Hendriks, F. Spinato, T. van Delft, G. Garrad, and U. Thomas, "Measuring wind turbine reliability-results of the reliawind project," in *EWEA Conference*, 2011, pp. 1–8.

[57] K. Fischer and J. Wenske, "Towards reliable power converters for wind turbines: Field-data based identification of weak points and cost drivers," *in Scientific Proceedings of EWEA*, 2015.

[58] S. Yang, A. Bryant, P. Mawby, D. Xiang, L. Ran, and P. Tavner, "An industry-based survey of reliability in power electronic converters," *IEEE Transactions on Industry Applications*, vol. 47, no. 3, pp. 1441–1451, May 2011.

[59] H. Wang, M. Liserre, F. Blaabjerg, P. de Place Rimmen, J. Jacobsen, T. Kvisgaard, and J. Landkildehus, "Transitioning to physics-of-failure as a reliability driver in power electronics," *IEEE Journal of Emerging and Selected Topics in Power Electronics*, vol. 2, no. 1, pp. 97–114, March 2014.

[60] J. Lutz, H. Schlangenotto, U. Scheuermann, and R. Doncker, "Semiconductor properties," *Semiconductor Power Devices*, pp. 17–75, 2011.

[61] M. Ciappa, "Selected failure mechanisms of modern power modules," *Microelectronics reliability*, vol. 42, no. 4, pp. 653–667, 2002.

[62] H. Oh, B. Han, P. McCluskey, C. Han, and B. D. Youn, "Physics-of-failure, condition monitoring, and prognostics of insulated gate bipolar transistor modules: A review," *IEEE Transactions on Power Electronics*, vol. 30, no. 5, pp. 2413–2426, May 2015.

[63] A. Wintrich, U. Nicolai, W. Tursky, and T. Reimann, *Application Manual Power Semiconductors*, 2nd ed., ISLE, Ed. Semikron, 2015.

[64] C. Bailey, H. Lu, and T. Tilford, "Predicting the reliability of power electronic modules," in *2007 8th International Conference on Electronic Packaging Technology*, Aug 2007, pp. 1–5.

[65] M. Schulz, "Thermal management details and their influence on the aging of power semiconductors," in *Proc. of 2014 16th European Conference on Power Electronics and Applications (EPE'14-ECCE Europe).* IEEE, 2014, pp. 1–6.

[66] H. Huang and P. A. Mawby, "A lifetime estimation technique for voltage source inverters," *IEEE Transactions on Power Electronics*, vol. 28, no. 8, pp. 4113–4119, Aug 2013.

[67] V. Smet, F. Forest, J.-J. Huselstein, F. Richardeau, Z. Khatir, S. Lefebvre, and M. Berkani, "Ageing and failure modes of igbt modules in high-temperature power cycling," *IEEE Transactions on Industrial Electronics*, vol. 58, no. 10, pp. 4931–4941, Oct 2011.

[68] R. Wu, F. Blaabjerg, H. Wang, M. Liserre, and F. Iannuzzo, "Catastrophic failure and fault-tolerant design of igbt power electronic converters-an overview," in *Industrial Electronics Society, IECON 2013-39th Annual Conference of the IEEE.* IEEE, 2013, pp. 507–513.

[69] C. Felgemacher, S. V. Araujo, C. Noeding, and P. Zacharias, "Benefits of increased cosmic radiation robustness of sic semiconductors in large power-converters," in *PCIM Europe 2016; International Exhibition and Conference for Power Electronics, Intelligent Motion, Renewable Energy and Energy Management*, May 2016, pp. 1–8.

[70] B. Gadalla, E. Schaltz, and F. Blaabjerg, "A survey on the reliability of power electronics in electro-mobility applications," in *Intl Symposium on Advanced Electromechanical Motion Systems (ELECTROMOTION)*, Sept 2015, pp. 304–310.

[71] H. Wang and F. Blaabjerg, "Reliability of capacitors for dc-link applications in power electronic converters - an overview," *IEEE Transactions on Industry Applications*, vol. 50, no. 5, pp. 3569–3578, 2014.

[72] Y. Ko, H. Jedtberg, G. Buticchi, and M. Liserre, "Analysis of dc-link current influence on temperature variation of capacitor in a wind turbine application," *IEEE Transactions on Power Electronics*, vol. PP, no. 99, pp. 1–1, 2017.

[73] P. Matkowski and I. Brabandt, "Modal analysis of board vibration during mechanical reliability tests of lead-free solder joints," in *2012 4th Electronic System-Integration Technology Conference*, Sept 2012, pp. 1–7.

[74] P. Matkowski, R. Zawierta, and J. Felba, "Vibration response of printed circuit board in wide range of temperature. characterization of pcb materials," in *32nd International Spring Seminar on Electronics Technology*, May 2009, pp. 1–6.

[75] J. S. Karppinen, J. Li, and M. Paulasto-Krockel, "The effects of concurrent power and vibration loads on the reliability of board-level interconnections in power electronic assemblies," *IEEE Transactions on Device and Materials Reliability*, vol. 13, no. 1, pp. 167–176, March 2013.

[76] S. Joshy, V. Verdingovas, M. Jellesen, and R. Ambat, "Simulation of electronic circuit sensitivity towards humidity using electrochemical data on water layer," in *2015 IEEE 17th Electronics Packaging and Technology Conference (EPTC)*, Dec 2015, pp. 1–5.

[77] C. Andersson, J. Ingman, E. Varescon, and M. Kiviniemi, "Detection of cracks in multilayer ceramic capacitors by x-ray imaging," *Microelectronics Reliability*, vol. 64, pp. 352 – 356, 2016, proceedings of the 27th European Symposium on Reliability of Electron Devices, Failure Physics and Analysis.

[78] P. Ghimire, S. Beczkowski, S. Munk-Nielsen, B. Rannestad, and P. B. Thogersen, "A review on real time physical measurement techniques and their attempt to predict wear-out status of igbt," in *Proc. of 2013 15th European Conference on Power Electronics and Applications (EPE)*, Sept 2013, pp. 1–10.

[79] H. Jedtberg, M. Langwasser, R. Zhu, G. Buticchi, and M. Liserre, "Impacts of rotor current control targets during unbalanced grid faults on dc-link capacitor lifetime in dfig wind turbine systems," in *Proc. of 2017 IEEE Energy Conversion Congress and Exposition (ECCE)*, 2017.

[80] T. Herrmann, M. Feller, J. Lutz, R. Bayerer, and T. Licht, "Power cycling induced failure mechanisms in solder layers," in *Proc. of 2007 European Conference on Power Electronics and Applications*, Sept 2007, pp. 1–7.

[81] H. Conseil-Gudla, Z. Staliulionis, M. S. Jellesen, M. Jabbari, J. H. Hattel, and R. Ambat, "Humidity buildup in electronic enclosures exposed to constant conditions," *IEEE Transactions on Components, Packaging and Manufacturing Technology*, vol. 7, no. 3, pp. 412–423, March 2017.

[82] H. Conseil, V. C. Gudla, M. S. Jellesen, and R. Ambat, "Humidity build-up in a typical electronic enclosure exposed to cycling conditions and effect on corrosion reliability," *IEEE Transactions on Components, Packaging and Manufacturing Technology*, vol. 6, no. 9, pp. 1379–1388, Sept 2016.

[83] S. J. Watson, B. J. Xiang, W. Yang, P. J. Tavner, and C. J. Crabtree, "Condition monitoring of the power output of wind turbine generators using wavelets," *IEEE Transactions on Energy Conversion*, vol. 25, no. 3, pp. 715–721, Sept 2010.

[84] G. L. Skibinski, R. J. Kerkman, and D. Schlegel, "Emi emissions of modern pwm ac drives," *IEEE Industry Applications Magazine*, vol. 5, no. 6, pp. 47–80, Nov 1999.

[85] H. Kabza, H. J. Schulze, Y. Gerstenmaier, P. Voss, J. W. W. Schmid, F. Pfirsch, and K. Platzoder, "Cosmic radiation as a cause for power device failure and possible countermeasures," in *Proceedings of the 6th International Symposium on Power Semiconductor Devices and Ics*, May 1994, pp. 9–12.

[86] C. Felgemacher, S. V. Araújo, P. Zacharias, K. Nesemann, and A. Gruber, "Cosmic radiation ruggedness of si and sic power semiconductors," in *2016 28th International Symposium on Power Semiconductor Devices and ICs (ISPSD)*, June 2016, pp. 51–54.

[87] J. M. Thebaud, E. Woirgard, C. Zardini, S. Azzopardi, O. Briat, and J. M. Vinassa, "Strategy for designing accelerated aging tests to evaluate igbt power modules lifetime in real operation mode," *IEEE Transactions on Components and Packaging Technologies*, vol. 26, no. 2, pp. 429–438, June 2003.

[88] K. Ma, N. He, M. Liserre, and F. Blaabjerg, "Frequency-domain thermal modeling and characterization of power semiconductor devices," *IEEE Transactions on Power Electronics*, vol. 31, no. 10, pp. 7183–7193, Oct 2016.

[89] Y. Song and B. Wang, "Survey on reliability of power electronic systems," *IEEE Transactions on Power Electronics*, vol. 28, no. 1, pp. 591–604, Jan 2013.

[90] K. Ma, H. Wang, and F. Blaabjerg, "New approaches to reliability assessment: Using physics-of-failure for prediction and design in power electronics systems," *IEEE Power Electronics Magazine*, vol. 3, no. 4, pp. 28–41, Dec 2016.

[91] H. Lu, C. Bailey, and C. Yin, "Design for reliability of power electronics modules," *Microelectronics reliability*, vol. 49, no. 9, pp. 1250–1255, 2009.

[92] M. Musallam, C. Yin, C. Bailey, and M. Johnson, "Mission profile-based reliability design and real-time life consumption estimation in power electronics," *IEEE Transactions on Power Electronics*, vol. 30, no. 5, pp. 2601–2613, May 2015.

[93] K. Ma, M. Liserre, F. Blaabjerg, and T. Kerekes, "Thermal loading and lifetime estimation for power device considering mission profiles in wind power converter," *IEEE Transactions on Power Electronics*, vol. 30, no. 2, pp. 590–602, Feb 2015.

[94] B. Ji, X. Song, E. Sciberras, W. Cao, Y. Hu, and V. Pickert, "Multiobjective design optimization of igbt power modules considering power cycling and thermal cycling," *IEEE Transactions on Power Electronics*, vol. 30, no. 5, pp. 2493–2504, May 2015.

[95] S. Yang, D. Xiang, A. Bryant, P. Mawby, L. Ran, and P. Tavner, "Condition monitoring for device reliability in power electronic converters: A review," *IEEE Transactions on Power Electronics*, vol. 25, no. 11, pp. 2734–2752, Nov 2010.

[96] A. Volke and M. Hornkamp, *IGBT modules: technologies, driver and application*, 2nd ed. Infineon Technologies AG, 2012.

[97] J. Lutz, "Packaging and reliability of power modules," in *CIPS 2014; 8th International Conference on Integrated Power Electronics Systems*, Feb 2014, pp. 1–8.

[98] S. Haumann, M. Becker, J. Rudzki, R. Eisele, and F. Osterwald, "Novel bonding and joining technology for power electronics - enabler for improved lifetime, reliability, cost and power density," in *Applied Power Electronics Conference and Exposition (APEC), 2013 Twenty-Eighth Annual IEEE*, March 2013, pp. 622–626.

[99] W. Zhang, D. Xu, P. N. Enjeti, H. Li, J. T. Hawke, and H. S. Krishnamoorthy, "Survey on fault-tolerant techniques for power electronic converters," *IEEE Transactions on Power Electronics*, vol. 29, no. 12, pp. 6319–6331, Dec 2014.

[100] M. H. Rashid, *Power electronics handbook.* Butterworth-Heinemann, 2017.

[101] H. Wang, A. M. Khambadkone, and X. Yu, "Control of parallel connected power converters for low voltage microgrid part ii: Dynamic electrothermal modeling," *IEEE Transactions on Power Electronics*, vol. 25, no. 12, pp. 2971–2980, Dec 2010.

[102] Z. Wang, W. Qiao, B. Tian, and L. Qu, "An effective heat propagation path-based online adaptive thermal model for igbt modules," in *Proc. of 2014 IEEE Applied Power Electronics Conference and Exposition - APEC 2014*, March 2014, pp. 513–518.

[103] A. Castellazzi, E. Batista, M. Ciappa, J.-M. Dienot, M. Mermet-Guyennet, and W. Fichtner, “Full electro-thermal model of a 6.5kv field-stop igbt module,” in *Power Electronics Specialists Conference, 2008. PESC 2008. IEEE*, June 2008, pp. 392–397.

[104] N. Baker, M. Liserre, L. Dupont, and Y. Avenas, “Junction temperature measurements via thermo-sensitive electrical parameters and their application to condition monitoring and active thermal control of power converters,” in *Proc. of 39th Annual Conference of the IEEE Industrial Electronics Society, IECON 2013*, Nov 2013, pp. 942–948.

[105] J. Lehmann, M. Netzel, R. Herzer, and S. Pawel, “Method for electrical detection of bond wire lift-off for power semiconductors,” in *Power Semiconductor Devices and ICs, 2003. Proceedings. ISPSD ’03. 2003 IEEE 15th International Symposium on*, April 2003, pp. 333–336.

[106] A. J. Forsyth, S. y. Yang, P. A. Mawby, and P. Igic, “Measurement and modelling of power electronic devices at cryogenic temperatures,” *IEE Proceedings - Circuits, Devices and Systems*, vol. 153, no. 5, pp. 407–415, October 2006.

[107] D. Barlini, M. Ciappa, M. Mermet-Guyennet, and W. Fichtner, “Measurement of the transient junction temperature in mosfet devices under operating conditions,” *Microelectronics Reliability*, vol. 47, no. 9, pp. 1707 – 1712, 2007, 18th European Symposium on Reliability of Electron Devices, Failure Physics and Analysis.

[108] J. Lemmens, P. Vanassche, and J. Driesen, “Optimal control of traction motor drives under electrothermal constraints,” *IEEE Journal of Emerging and Selected Topics in Power Electronics*, vol. 2, no. 2, pp. 249–263, June 2014.

[109] L. Coffin Jr, “A study of the effects of cyclic thermal stresses on a ductile metal,” *Trans. ASME*, vol. 76, pp. 931–950, 1954.

[110] H. Cui, “Accelerated temperature cycle test and coffin-manson model for electronic packaging,” in *Annual Reliability and Maintainability Symposium, 2005. Proceedings.*, Jan 2005, pp. 556–560.

[111] I. Kovacevic, U. Drofenik, and J. Kolar, “New physical model for lifetime estimation of power modules,” in *Proc. of 2010 International Power Electronics Conference (IPEC)*, June 2010, pp. 2106–2114.

[112] F. Blaabjerg, K. Ma, and D. Zhou, “Power electronics and reliability in renewable energy systems,” in *Proc. of IEEE International Symposium on Industrial Electronics (ISIE)*. IEEE, 2012, pp. 19–30.

[113] R. Bayerer, T. Herrmann, T. Licht, J. Lutz, and M. Feller, “Model for power cycling lifetime of igbt modules - various factors influencing lifetime,” in *Proc. of*

5th International Conference on Integrated Power Systems (CIPS). VDE, 2008, pp. 1–6.

[114] H. Lu, T. Tilford, and D. Newcombe, "Lifetime prediction for power electronics module substrate mount-down solder interconnect," in *Proc. of International Symposium on High Density packaging and Microsystem Integration, HDP'07.* IEEE, 2007, pp. 1–10.

[115] M. Musallam and C. M. Johnson, "An efficient implementation of the rainflow counting algorithm for life consumption estimation," *IEEE Transactions on Reliability*, vol. 61, no. 4, pp. 978–986, 2012.

[116] B. Ji, V. Pickert, W. Cao, and B. Zahawi, "In situ diagnostics and prognostics of wire bonding faults in igbt modules for electric vehicle drives," *IEEE Transactions on Power Electronics*, vol. 28, no. 12, pp. 5568–5577, Dec 2013.

[117] S. M. Avery and R. D. Lorenz, "In situ measurement of wire-bond strain in electrically active power semiconductors," *IEEE Transactions on Industry Applications*, vol. 49, no. 2, pp. 973–981, March 2013.

[118] P. Sun, C. Gong, X. Du, Y. Peng, B. Wang, and L. Zhou, "Condition monitoring igbt module bond wires fatigue using short-circuit current identification," *IEEE Transactions on Power Electronics*, vol. 32, no. 5, pp. 3777–3786, May 2017.

[119] D. Hirschmann, D. Tissen, S. Schroder, and R. De Doncker, "Reliability prediction for inverters in hybrid electrical vehicles," *Power Electronics, IEEE Transactions on*, vol. 22, no. 6, pp. 2511–2517, Nov 2007.

[120] J. Zhang, Y. Li, H. Wang, X. Cai, S. Igarashi, and Z. Wang, "Thermal smooth control based on orthogonal circulating current for multi-mw parallel wind power converter," in *2014 International Power Electronics and Application Conference and Exposition*, Nov 2014, pp. 146–151.

[121] K. Ma, M. Liserre, and F. Blaabjerg, "Reactive power influence on the thermal cycling of multi-mw wind power inverter," *IEEE Transactions on Industry Applications*, vol. 49, no. 2, pp. 922–930, March 2013.

[122] J. Lemmens, J. Driesen, and P. Vanassche, "Dynamic dc-link voltage adaptation for thermal management of traction drives," in *Proc. of 2013 IEEE Energy Conversion Congress and Exposition (ECCE)*, Sept 2013, pp. 180–187.

[123] M. Weckert and J. Roth-Stielow, "Lifetime as a control variable in power electronic systems," in *Proc. of 2010 Emobility - Electrical Power Train*, Nov 2010, pp. 1–6.

[124] P. K. Prasobhu, G. Buticchi, S. Brueske, and M. Liserre, “Gate driver for the active thermal control of a dc/dc gan-based converter,” in *2016 IEEE Energy Conversion Congress and Exposition (ECCE)*, Sept 2016, pp. 1–8.

[125] C. Sintamarean, H. Wang, F. Blaabjerg, and F. Iannuzzo, “The impact of gate-driver parameters variation and device degradation in the pv-inverter lifetime,” in *Proc. of 2014 IEEE Energy Conversion Congress and Exposition (ECCE)*, Sept 2014, pp. 2257–2264.

[126] F. Hahn, G. Buticchi, and M. Liserre, “Active thermal balancing for modular multilevel converters in hvdc applications,” in *2016 18th European Conference on Power Electronics and Applications (EPE’16 ECCE Europe)*, Sept 2016, pp. 1–10.

[127] M. Andresen, G. Buticchi, and M. Liserre, “Thermal stress analysis and mppt optimization of photovoltaic systems,” *IEEE Transactions on Industrial Electronics*, vol. 63, no. 8, pp. 4889–4898, Aug 2016.

[128] M. Andresen and M. Liserre, “Impact of active thermal management on power electronics design,” *Microelectronics Reliability*, vol. 54, no. 9, pp. 1935–1939, 2014.

[129] A. Isidori, F. M. Rossi, F. Blaabjerg, and K. Ma, “Thermal loading and reliability of 10-mw multilevel wind power converter at different wind roughness classes,” *IEEE Transactions on Industry Applications*, vol. 50, no. 1, pp. 484–494, Jan 2014.

[130] K. Ma and F. Blaabjerg, “Modulation methods for neutral-point-clamped wind power converter achieving loss and thermal redistribution under low-voltage ride-through,” *IEEE Transactions on Industrial Electronics*, vol. 61, no. 2, pp. 835–845, Feb 2014.

[131] L. Wu and A. Castellazzi, “Temperature adaptive driving of power semiconductor devices,” in *Proc. of 2010 IEEE International Symposium on Industrial Electronics*, July 2010, pp. 1110–1114.

[132] X. Wang, Z. Zhao, and L. Yuan, “Current sharing of igbt modules in parallel with thermal imbalance,” in *Proc. of 2010 IEEE Energy Conversion Congress and Exposition*, Sept 2010, pp. 2101–2108.

[133] L. Mackay, R. Guarnotta, A. Dimou, G. Morales-España, L. Ramirez-Elizondo, and P. Bauer, “Optimal power flow for unbalanced bipolar dc distribution grids,” *IEEE Access*, vol. 6, pp. 5199–5207, 2018.

[134] M. Liserre, M. Andresen, L. Costa, and G. Buticchi, “Power routing in modular smart transformers: Active thermal control through uneven loading of cells,” *IEEE Industrial Electronics Magazine*, vol. 10, no. 3, pp. 43–53, Sept 2016.

[135] M. M. Esfahani, H. F. Habib, and O. A. Mohammed, "A hierarchical power routing scheme for interlinking converters in unbalanced hybrid ac-dc microgrids," in *IECON 2018 - 44th Annual Conference of the IEEE Industrial Electronics Society*, Oct 2018, pp. 53–58.

[136] M. A. Allam, A. A. Hamad, M. Kazerani, and E. F. El-Saadany, "A novel dynamic power routing scheme to maximize loadability of islanded hybrid ac/dc microgrids under unbalanced ac loading," *IEEE Transactions on Smart Grid*, vol. 9, no. 6, pp. 5798–5809, Nov 2018.

[137] A. Marquez, J. I. Leon, S. Vazquez, L. G. Franquelo, G. Buticchi, and M. Liserre, "Power device lifetime extension of dc-dc interleaved converters via power routing," in *IECON 2018 - 44th Annual Conference of the IEEE Industrial Electronics Society*, Oct 2018, pp. 5332–5337.

[138] Y. Ko, M. Andresen, G. Buticchi, M. Liserre, and L. Concari, "Multi-frequency power routing for cascaded h-bridge inverters in smart transformer application," in *2016 IEEE Energy Conversion Congress and Exposition (ECCE)*, Sept 2016, pp. 1–7.

[139] M. Andresen, V. Raveendran, G. Buticchi, and M. Liserre, "Lifetime-based power routing in parallel converters for smart transformer application," *IEEE Transactions on Industrial Electronics*, vol. PP, no. 99, pp. 1–1, 2017.

[140] G. Buticchi, M. Andresen, M. Wutti, and M. Liserre, "Lifetime-based power routing of a quadruple active bridge dc/dc converter," *IEEE Transactions on Power Electronics*, vol. 32, no. 11, pp. 8892–8903, Nov 2017.

[141] M. Andresen, G. Buticchi, J. Falck, M. Liserre, and O. Muehlfeld, "Active thermal management for a single-phase h-bridge inverter employing switching frequency control," in *Proc. of PCIM Europe 2015; International Exhibition and Conference for Power Electronics, Intelligent Motion, Renewable Energy and Energy Management*, May 2015, pp. 1–8.

[142] S. Kouro, P. Cortes, R. Vargas, U. Ammann, and J. Rodriguez, "Model predictive control: A simple and powerful method to control power converters," *IEEE Transactions on Industrial Electronics*, vol. 56, no. 6, pp. 1826–1838, June 2009.

[143] J. Wölfle, T. Röser, M. Nitzsche, N. Tröster, M. Stempfle, J. Ruthardt, and J. Roth-Stielow, "Model based temperature control system to increase the expected lifetime of igbt power modules executed on a neutral point diode clamped three level inverter," in *Proc. of 2017 19th European Conference on Power Electronics and Applications (EPE'17 ECCE Europe)*, 2017, pp. 1–9.

9. List of figures

10. List of tables

11. Appendix

11.1 Technical data of the experimental setup

Component	**Parameter**	**Symbol**	**Value**	**Unit**
Control system	sampling time	T_s	50	μs
IGBT Module	max. voltage	v_{dc}	1.2	kV
IGBT Module	max. current	I_{max}	25	A
Induction Machine	rated power	P_r	5.5	kW
Induction Machine	rated speed	n_r	1455	rpm
Induction Machine	rated torque	M_r	36.1	Nm
Infrared camera	used bandwidth	f_{ir}	200	Hz
Infrared camera	rated accuracy	T_{err}	±0.02	K

Table 11.1: Experimental setup parameters

In experiments with opened IGBT modules without insulating gel the max. voltage is decreased to 500 V to reduce the risk of short circuits through dust and debris that might have settled on the modules substrate.

11.2 Photos of the experimental setup

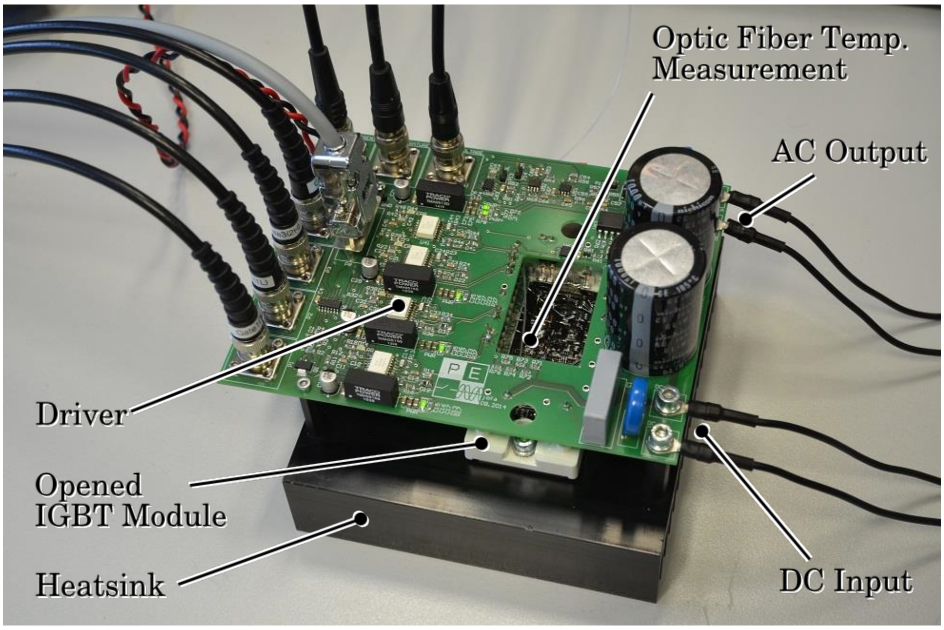

Figure 11.1: Inverter experimental setup. An opened IGBT module is installed to allow measurement the semiconductor temperatures during operation via an infrared camera.

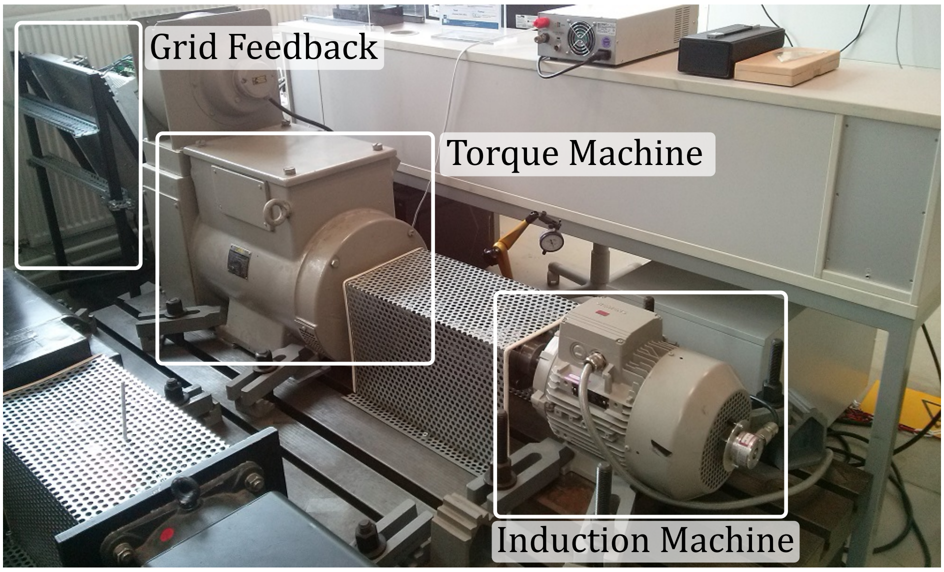

Figure 11.2: The machine test bench used for experimental validation of the thermal-based FCS-MPC.

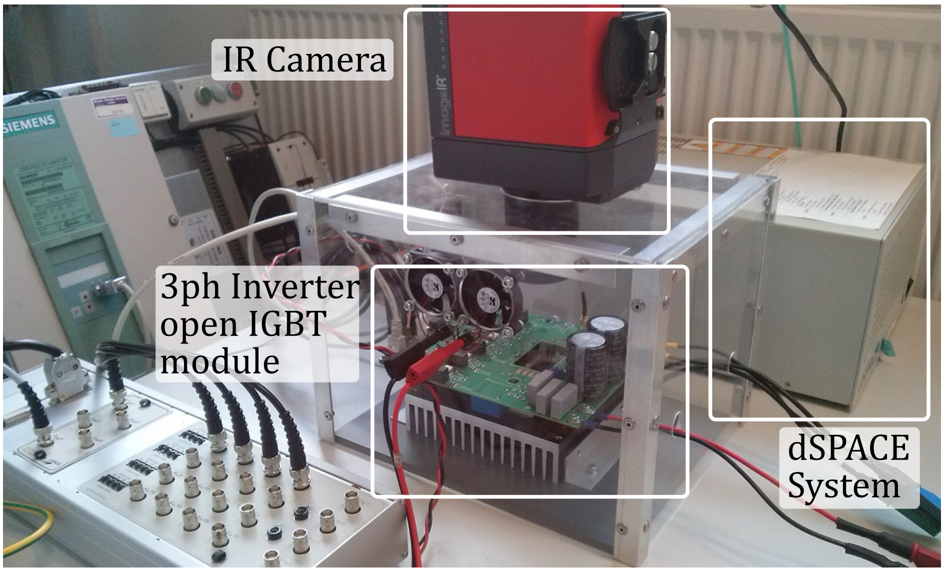

Figure 11.3: The three-phase inverter experimental setup. The infrared camera is used to measure the semiconductor temperature profile of an opened IGBT module during operation.

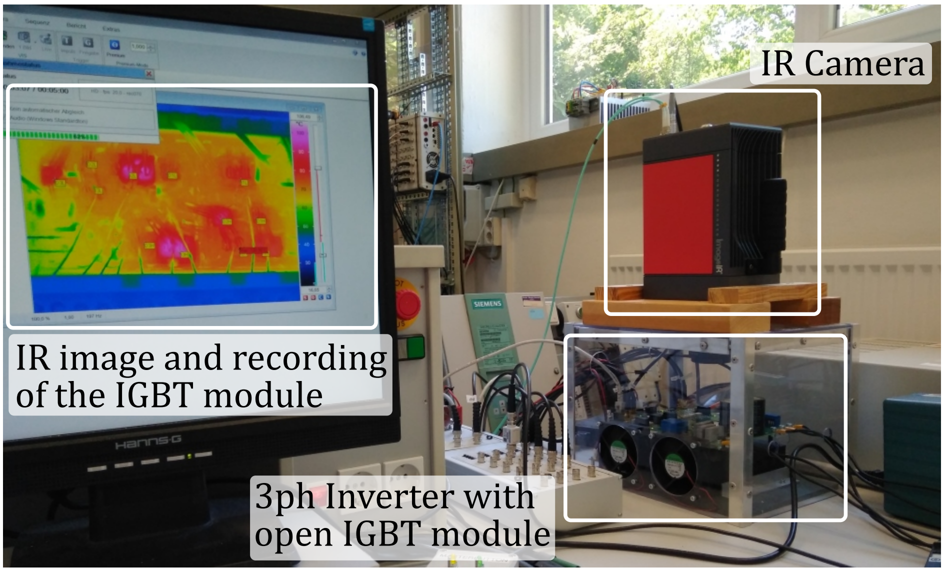

Figure 11.4: The infrared measurement of the infrared camera displays and records the whole IGBT module during operation. The chip temperature detection is based on the known positions of the semiconductors on the substrate of the IGBT module.